2019

Innovations in material characterization and structural configuration of link slabs

Rizwan Karim
Iowa State University

Innovations in material characterization and structural configuration of link slabs

by

Rizwan Karim

A thesis submitted to the graduate faculty

in partial fulfillment of the requirements for the degree of

MASTER OF SCIENCE

Major: Civil, Construction, and Environmental Engineering (Structural Engineering)

Program of Study Committee:
Behrouz Shafei, Major Professor
Brent Phares
Jennifer Shane

The student author, whose presentation of the scholarship herein was approved by the program of study committee, is solely responsible for the content of this thesis. The Graduate College will ensure this thesis is globally accessible and will not permit alterations after a degree is conferred.

Iowa State University

Ames, Iowa

2019

DEDICATION

To my parents,

Sher Faraz Khan and Daftar Bibi,

For their support, love and encouragement

TABLE OF CONTENTS

Page

LIST OF FIGURES

Page

LIST OF TABLES

Page

ACKNOWLEDGMENTS

This thesis would not have been possible without the guidance, and support of my major supervisor Dr. Behrouz Shafei. I would like to thank my committee members, Dr. Brent Phares and Dr. Jennifer Shane for their guidance and time throughout the course of this research.

I would like to extend my gratitude to Dr. Meysam Najimi and Dr. Shahin Hajilar for their help in conducting this research.

In addition, I would also like to thank my friends, colleagues, the department faculty and staff for making my time at Iowa State University a wonderful experience. I want to also offer my appreciation to all the staff members and student helpers in Structures laboratory and PCC laboratory at Iowa State University.

I would also like to extend acknowledgement to the Fulbright Program, Iowa Department of Transportation, and Accelerated Bridge Construction University Transportation Center for their financial support.

ABSTRACT

Expansion joints included in bridges to accommodate thermal expansion and contraction provide an easy route for water to pass through to the underlying substructure, thus, causing corrosion of the substructure. These expansion joints accumulate debris and require frequent repair and maintenance. Link slabs provide a potential solution to eliminating these expansion joints. The research presented in this thesis explores the structural behavior of link slabs through experimental tests and finite element simulations. The study presents a novel non-proprietary ultra-high performance concrete, which can also be a potential replacement for materials used in the link slabs.

The first part of this thesis consists of testing two full scale link slab specimens in the laboratory. The link slabs were made of fiber-reinforced concrete (FRC) with steel and GFRP rebars. The link slabs were carefully designed so that the stresses from the concrete deck are effectively transferred to the link slab. The designed link slabs were tested to evaluate the detailing of the transition zone and to understand the overall performance of the structural setup. A comparison was then made between the results obtained from the two link slabs. A set of finite element models were developed for the link slabs tested and the parameters, such as rebar spacing in debonded length, rebar spacing in bonded length and depth of link slab, were evaluated.

In the second part, an experimental setup was tested to find out the effect of support condition on the stresses in the link slab. The effect of support condition was further evaluated by developing a set of finite element models for a case study bridge to explore the possibility of installing a link slab on existing bridge structures. The finite element study not only evaluated the response of link slabs, but also determined its effect on the

substructure of the existing bridges. In the final part, a nonproprietary UHPC was developed with the properties that are important for link slabs. The non-proprietary UHPC was tested for transport properties, volume stability, and frost resistance. The non-proprietary UHPC mixes tested showed characteristics comparable to the proprietary UHPC mixes, thus, making it a competitive alternative to be used in link slabs.

CHAPTER 1. INTRODUCTION

1.1 Overview

Bridges are often supported by steel or concrete girders that sit on piers. There are expansion joints provided in the continuous decks to allow for thermal stress release. The expansion joints, however, permit water and aggressive agents, such as chlorides and carbonates, to directly reach the girder under the bridge deck, leading to deterioration induced by corrosion. Additionally, debris can be accumulated in the expansion joints, resulting in the generation of additional stresses in the bridge superstructure. According to a survey conducted by Fincher (1983), about 60% of expansion joints start leaking after 5 years and other 40% experience some extent of damage that decreases their expected service life. This has caused significant direct and indirect costs to maintain and repair the expansion joints (Wolde-Tinsae and Klinger, 1987, Lepech et al., 2005).

There are two methods to eliminate the expansion joints: first, by providing an integral bridge deck construction on a continuous girder, and second, by having a jointless deck on simply supported girders. The integral bridge deck on the continuous girder system relies on the flexibility of the piers to accommodate the thermal stresses, but this can result in the formation of cracks in piers and additional safety concerns. The jointless deck systems, however, can be equipped with a link slab, which connects the two bridge decks from the slab supported on simply supported girders.

1.2 Research Needs and Gaps

The literature review presented below indicates three important aspects to be explored:

1. Details of the transition zone
2. Materials appropriate for link slabs

3. Support conditions provided under link slabs

1.2.1 Design of Transition Zone

The initial design of the link slab had debonding length starting directly from the concrete deck. The design of the transition zone was ignored in the initial work of Caner and Zia (1998), where the debonding region begins just at the face of connection of concrete deck and link slab. There was no special design provided in the transition zone between the main slab and link slab, resulting in high stress concentration at the interface. The Michigan Department of Transportation (Gilani and Juntunen, 2001, and Gilani and Janson, 2004) reported problems with the connection of engineered cementitious composites (ECC) link slab and deck. The transition zone underwent macrocracking, which could be because the ECC link slab and the concrete were not placed at the same time. Qian et al. (2011) worked on the design of the transition zone. The study tested three full scale link slabs. The shear studs in the transition zone (bonded zone) were placed at as close as 4 inches, which was even lower than the AASHTO minimum limit of 4.5 in. The reinforcement was extended into the transition zone up to 6 inches only, which is the development length of #3 rebars in ECC. The specimens were tested for cyclic loading. The transition zone showed no macrocrack as was the case in previous studies. The study recommended the provision of shear studs in the transition zone along with extension of top rebars into the transition zone. Reyes and Robertson (2011), introduced the concept of partial depth link slab. This concept although very unique required a significant care in detailing the bonded zone. Reyes and Robertson (2011) designed the transition zone of the link slab by the provision of the dowel bars in the bonded zone. The dowels bar were extending from the FRC link slab to the deck concrete deck underneath. The arrangement was effective for cast in place link slab but for a precast link slab there were

macrocracking in the transition zone. Larusson (2013) provides an innovative way of detailing for partial depth link slab by including a supplementary set of reinforcement. The supplementary reinforcement extends into the transition zone of link slab and the approach slab deck. This detailing can be used both in cast in place and precast link slabs. Larusson (2013) tested the link slabs by axially loading them, but did not provide any information on their behavior under flexural loading.

The current literature is limited in terms of detailing of the transition zone, which holds a significant importance in the design of the bonded zone in half depth and partial depth link slabs, especially when the link slab is intended to be installed in a rehabilitation project. The innovative idea of providing supplementary reinforcement seems a viable solution, but it needs to be explored under both axial force and bending moment.

1.2.2 Link Slab Materials

The link slab is designed to behave as a pinned connection and let the underlying girders to behave as a simply supported setup, with no cracking in the link slab. These two goals compete with each other, as a pin behavior requires less reinforcement, while controlling the crack width dictates a dense reinforcement in the link slab. This motivated the studies to look into materials that have inherent behavior of controlling crack width, thus requiring less reinforcement to control the crack width. There have been a number of studies on Engineered Cementitious Composites (ECC), Fiber reinforced concrete (ECC) and Ultra high-performance concrete (UHPC) in combination with either steel or glass fiber reinforced polymer (GFRP) rebars.

The early work on use of ECC in the link slab is by Lepech and Li (2005). The study used ECC in the link slab following the design procedure of Caner and Zia (1998). It was found

that the ECC link slab showed a more ductile behavior and the crack width for the ECC link slab was 10 times smaller than the crack width developed in the concrete link slab for the same number of cyclic loadings. The ECC link slabs tested in the laboratory were then implemented in the field. The link slabs in the field were instrumented to monitor the long term behavior of the link slab (Lepech and Li, 2009). A full scale test was also conducted in the field to evaluate the condition of the ECC link slab.

Hossain and Anwar (2014) evaluated the ECC link slab through experimental tests. The samples made were for 1/4th scale link slab models using ECC. One normal concrete link slab and four ECC link slabs were built. The link slabs were tested under monotonic loading. The normal concrete link slab showed a crack in the initial phase of loading and this crack kept widening as the load was increased, while the ECC had thin cracks confined in the debonded zone. The ECC link slabs performed better as compared to the normal concrete link slab in terms of ductility, energy absorption and limiting crack width. The results showed that the ECC link slab was still behaving as intended in "pure bending, uncoupled from girders". Reyes and Robertson (2011) and Larusson (2013) studied FRC with GFRP rebars. Reyes and Robertson (2011) studied the behavior of FRC with GFRP rebars under flexural loading, while Larusson (2013) explored the behavior of the FRC with GFRP under axial loading. These studies emphasized on the strain hardening properties of FRC and the lower modulus of elasticity of the GFRP rebars, the combination of which results in a flexible link slab with tighter crack widths. Despite few studies that have been done on ECC and other cementitious materials, there is a need for further improvement of link slab materials with FRC and UHPC. This requires additional investigations regarding the type of materials to be used and their behavior in combination with steel or GFRP reinforcement.

1.2.3 Effect of Support Conditions

The earliest work on link slab has been done by Caner and Zia (1998). The experimental work provided design recommendations for the link slabs. The study tested two link slabs on two different types of girder, i.e., steel girders and concrete girders. The link slab was debonded by placing two layers of plastic sheet, which was meant to reduce release the moments, so that the total stresses can be minimized. The length of the debonded zone on each side was set to 5% of the span length. The superstructures were then tested for four different support conditions. The superstructures were initially loaded up to about 40% of their ultimate capacity and the variation in the behavior of the link slabs were monitored. It was found that the slope of load vs. deflection curve was practically the same for all different support conditions considered. Since the deflections measured experimentally were in close agreement with those obtained theoretically, it was concluded that the link slabs behaved as a pin and the girders behaved as in a simply supported setup. Moreover, from the distribution of cracks which were mainly found on the top surface of the link slabs, it was inferred that flexural bending governed the structural behavior of link slabs (rather than axial force).

The link slab designed by Caner and Zia (1998) was implemented in the field by North Carolina Department of Transportation. The link slab was monitored by instrumenting the structure. The results from the instrumented structure was published by Wing and Kowalawsky (2005). To find the effect of live loads, the bridge was tested under full-scale live load test and data was acquired to monitor the effect of changing weather conditions on the rotation induced at the end of the bridge. It was observed that the end rotations in the link slab were significantly lower than the design rotation of 0.002 rad, even when an overloaded condition was applied. It was concluded that the thermal rotations were greater than those induced by the live loads.

The use of limit state design approach and crack control criteria were recommended in this study.

The finite element studies by Okeil and Elsafty (2005), Mothe (2006), and Ulku et al. (2009) explored different design aspects of the link slab. Okeil and Elsafty (2005) studied the effect of different support conditions on the link slab. The initial understanding from Caner and Zia (1998) showed that change in support conditions had no effects in the load deflection variation from different support conditions. The study by Okeil and Elsafty (1998) showed that the support conditions has significant effect on the stresses developed in the link slab and the types of stresses developed in the link slab. Mothe (2006) explored the effect of introduction of link slab in the structure, debonded length, and changes in the supported conditions. The study confirmed the findings of Okeil and Elsafty (2005) and stated that the roller support conditions under link slab provided lower bound for stresses while the hinge supports under the link slab provided the upper bound of stresses. The study by Ulku et al. (2009) showed the effect of the changes in the link slab and provided a modified formula from Caner and Zia (1998) to design the link slabs. Hong et al. (2014) developed finite element method models for a full scale bridge to explore the effect of support conditions and reached conclusions similar to the previous studies. The current literature, however, lacks full-scale experiments to evaluate the effect of different support conditions on link slab. This is anticipated to address the discrepancies that have been reported for the expected response of link slabs in real applications.

1.3 Research Objectives and Outline

The goal of this research is to further the understanding of the structural behavior of link slabs by exploring the effect of support conditions and come up with innovative materials

and structural details that can provide a durable link slab for cast in place and rehabilitation bridge projects.

Chapter 2 of this thesis provides the details of the full-scale experimental tests completed as part of this research. This chapter provides a summary of the results from two full-scale experimental test setups and compares the performance of FRC link slabs with steel and GFRP rebars. This chapter also includes a set of finite element simulations performed using Abaqus software package. The validated model is then used for parametric studies on link slab specimens tested in laboratory. The effect of rebar spacing in debonded and bonded region of link slab and the depth of link slab was explored through finite element simulations.

Chapter 3 of this thesis has two sections. The first section includes the experimental work performed in laboratory to explore the effect of support conditions on stresses developed in the link slab. A set of finite element models are then developed for the experimental setup. The effect of support condition is further explored for thermal and gravity loading and the debonded length of the link slab is further investigated. The second section details the finite element simulation results for a case study bridge. This section explores the effect of introducing link slab on a bridge's overall response and the effect of stresses in the super and substructure. The effect of different support conditions is also explored by converting the bearing pads (defined as springs) to hinges and rollers. The effect of change in debonded length of the link slab is also explored. This chapter answers the question of effect of support condition on the stresses developed in the link slab and then in the sub and superstructure of an existing bridge after the addition of link slab.

Chapter 4 details the process of development of a non-proprietary UHPC for link slab construction purposes. As the proprietary UHPC is not always available or is very expensive

($1000-2000/yd^3), an alternative material that can provide characteristics close enough to proprietary UHPC (with reduced cost) would be of interest, especially for large-scale projects. The developed non-proprietary UHPC is expected to provide comparable strength and durability properties to the proprietary UHPC.

Chapter 5 provides the conclusions from the experimental work conducted in the laboratory, finite element simulations, and material testing and evaluation. This chapter summarizes the most significant findings from the entire study. Possible future work and topics worth further exploring for link slabs are outlined as well.

CHAPTER 2. PERFORMANCE EVALUATION OF LINK SLABS BY EXPERIMENTAL TESTS

Expansion joints in bridge structures are expensive to maintain and leads to problem like water leakage and debris accumulation (Caner and Zia, 1998). The link slabs can provide a potential solution for replacing the expansion joints and there are significant efforts made by transportation agencies to minimize the number of expansion joints using link slabs (Caner and Zia, 1998, Li et al., 2005, Reyes and Robertson, 2011, Larusson, 2013). These studies have contributed significantly to the body of knowledge on link slabs, but there is still need for an in-depth research to fully understand structural behavior of the link slabs and the materials to be used for them. This chapter presents innovative link slab design for bridges using a combination of fiber reinforced concrete (FRC) with steel and glass fiber reinforced polymer (GFRP) rebars.

The first section of this chapter includes a thorough literature review of studies done on structural testing of link slabs in the laboratory. The research gaps and needs were identified based on the literature review. The second section details the experimental setup including the bridge deck design, details of the two link slab designed, instrumentation details and testing procedure in the laboratory. The chapter then presents the results, including a comparison of the results from the two link slabs tested. A set of FE simulations are then performed on the validated models of the experimental test setup to explore the contribution of design parameters, such as rebar spacing in debonding zone, rebar spacing in bonded zone and depth of link slab.

The main objectives pursued in this chapter of the thesis are to investigate the effectiveness of rebars in transferring the stresses from concrete deck to the bonded and

debonded region of link slab, and to evaluate the behavior of FRC link slab reinforced with steel and GFRP rebars.

2.1 Literature Review

Expansion joints are provided in the bridge superstructures to accommodate the stresses generated by the temperature gradient. Although expansion joints are widely used in bridges, they require constant maintenance over the lifetime of bridge structures. The expansion joints allow water and aggressive agents such as chlorides and carbonates to directly reach the girder under the bridge deck, leading to deterioration induced by corrosion of steel. Additionally, debris accumulates in the expansion joints, resulting in the generation of additional stresses in the bridge superstructure. Noting the issues associated with expansion joints, development of jointless bridge structures are becoming the standard practice for transportation infrastructures. For this purpose, the application of link slabs in bridge superstructures has received great attention in the practice. This is due to the fact that link slabs can deliver a jointless bridge by replacing the expansion joints. A few research investigations using experimental tests, finite element simulations, and field observations have been conducted in the literature to evaluate the structural performance of bridge structures designed or retrofitted using link slabs.

The earliest experimental investigation on link slabs was conducted by Caner and Zia, (1998). Two superstructures of the same length were designed with a deck size of 2 ft wide and 4 in thick. Two different girder types, i.e., concrete and steel girders, were considered. Since the deflections measured experimentally were in close agreement with those obtained theoretically, it was shown that the link slabs behaved as a pin and the girders behaved as simply supported. Moreover, from the distribution of cracks which were mainly found on the top surface of the link slabs, it was concluded that flexural bending governed in the structural

behavior of link slabs rather than axial forces formed. The crack width control criteria were recommended for design of link slab based on this study. Wing and Kowalsky (2005) monitored the link slab designed by Caner and Zia (1998) implemented in the field. The results from this instrumentation and monitoring led to the conclusion that a material with tightly spaced crack width is desirable to be used in link slabs.

The knowledge from initial field observations indicates that a material with small crack widths and more ductile behavior will be ideal for link slab. This led researchers to consider advanced construction materials such as engineered cementitious composites (ECC), fiber Reinforced Concrete (FRC) and ultra-high performance concrete (UHPC) to be used in link slabs. Lepech and Li (2005) introduced the use of engineered cementitious materials (ECC) in link slab. It was observed that the ECC link slab showed a more ductile behavior and had tighter crack widths than concrete. Later researchers Qian et al. (2011) and Hossain and Anwar, (2014) observed similar behavior in the link slab.

Since the ECC performed well for link slabs, investigators started exploring materials that have similar behavior, like FRC, which has a strain hardening properties and results in smaller crack width because of the fibers. Reyes and Robertson (2011) explored the use of FRC. They tested partial depth link slab made with high-performance FRC in combination with glass fiber reinforced polymer (GFRP) rebars. The GFRP rebars have a lower modulus of elasticity and are good against corrosion. The study had a cast in place and a precast 3 in thick link slab in a 9 in thick concrete deck. The specimens were tested by fixing one end using anchorage and loading on the other end, which is cantilevered. The link slab is at a reasonable distance above the center of rotation that the forces in link slabs were assumed to be axial. The precast sample showed a localized crack at the connection of unbonded and bonded region, but

most of the cracks were limited to the unbonded region in both the samples. The cracking in the debonded zone involved very fine cracks. Lárusson et al., 2013, studied the design of link slabs using FRC and GFRP rebars. The experimental setup consisted of four samples with different rebars detailing for the bonded zone and varying percentage of reinforcement in all the samples. The samples had a 3 in link slab build in an 8 in deep concrete deck. The designed link slab was then tested by applying only axial loads. To simulate the effect of deflections on the link slab, the link slab was subjected to cyclic axial loading. The cracks in the debonded zone were very fine and the link slab observed a total strain of 1%, indicating that it was highly ductile. The study showed that the FRC in combination with GFRP can be a good material to be used in the link slab.

The link slab designed initially started directly from the face of the two bridge deck slabs. These link slabs had debonded length only, with no consideration for design of bonded and transition zone (Caner and Zia, 1998). As the design of link slabs gained interest the problem at the face of the connections were observed by researchers (Gilani and Juntunen, 2001, and Gilani and Janson, 2004). Macrocracks were observed at the face of the connection of link slab and the concrete deck. To tackle this problem of macrocracking at the face of connection, Qian et al., 2011, proposed designing the transition zone with denser shear studs, and extending the top rebars into the transition zone of the link slab. The transition zone showed no macrocracking but the spacing of shear studs provided was closer (at 4 in) than the AASHTO recommended limit of 4.5 in. The design of transition zone has become immensely critical with the introduction of the half depth link slabs. Reyes and Robertson (2011) used dowel bars extending into FRC link slab from the concrete deck underneath. No macrocracks were observed for the cast in place link slab, but macrocracking was observed for the precast

link slabs in the transition zone. Larusson (2013) studied the behavior of half depth FRC link slabs. The cracking in the transition zone was controlled by providing dense reinforcement in the transition zone. Four different sets of detailing were tested. The details differed in the length of rebars in the transition zone and the density of rebars in the transition zone. All the link slab with additional rebars in transition zone resulted in no macrocracking. The link slabs were tested by loading the specimens axially but no information could be obtained about the behavior of link slabs detailing under flexural loading.

Based on the literature review, there are two research needs which require further investigation: (1) Exploration of FRC to be used in link slabs in combination with steel and GFRP rebars, and (2) The detailing of transition zone especially for half depth link slabs. The current studies about the transition zone design are limited in general and scarce for the link slab with partial or half depth. This study aims to provide an insight into the possible material replacement for future link slabs and the design of transition zone in link slabs. Two different types of detailing for the transition zones are also provided. The details are carefully selected so that they can be applicable both in the cast in place and precast applications.

2.2 Experimental Setup

Two full-scale tests are conducted in the laboratory. Each specimen consists of two 21 ft, W21×55 A 36 steel girders. The steel girders support a concrete deck with a thickness of 20.3 cm (8 in). The concrete has a strength of 41.4 MPa (6 ksi) on the day of testing at 21 days. A 5 cm (2 in) gap is provided between the steel girders that represents the expansion joint. Two half-depth link slabs are constructed using fiber reinforced concrete (FRC). The half-depth link slabs are easy to be implemented in the field, especially for rehabilitation projects. The FRC is chosen because of its' high ductility and tension stiffening abilities in

tension, and having reduced crack width, and very low splitting crack. The FRC material used has a strength of 8 ksi on the day of testing at 21 days. Both link slabs have a depth of 27.6 cm (4 in), width 160 cm (63 in), and a total length of 170.2 cm (67 in). The link slabs are designed using the procedure provided by Caner and Zia (1998) and improved by Ulku et. al. (2009).

The test setup includes strain gages, embedded concrete strain gauges, surface strain gauges, DCDTs and LVDTs. A schematic view of the entire test setup is provided in Figure 2.1. Figure 2.2 shows the reinforcement mat and bridge specimen constructed in the laboratory. The details of the design of the bridge deck, design of link slabs, and instrumentations are provided in the following sections.

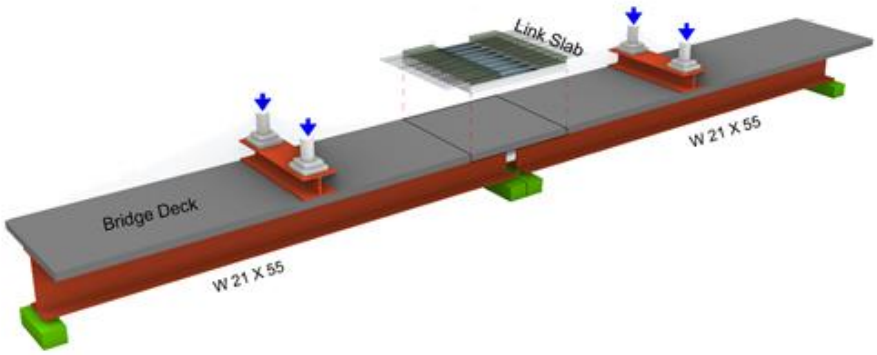

Figure 2.1 *A schematic view of the entire test setup*

Figure 2.2 *Slab reinforcement Mat*

2.2.1 Bridge Deck Design

A typical bridge designing method in accordance with the AASHTO-LRFD method is used for the concrete deck other than link slab. The deck is made of ordinary concrete with a compressive strength of 41.4 MPa (6 ksi). The depth of the concrete slab is chosen to be 20.3 cm (8 in). The depth is chosen based on section S2.5.2.6.3 of AASHTO LRFD. A width of a 160 cm (63 in) is chosen for the deck based on the AASHTO effective flange criteria to ensure a T-beam behavior.

Table 2.1 shows the reinforcement detailing for the bridge deck. The top rebars are cut off at the face of the connection between fiber reinforced concrete link slab and concrete deck. The concrete cover to the centroid of reinforcement rebar and bottom clear cover of the section is kept as 5 cm (2 in) and 2.5 cm (1 in), respectively. The top cover is chosen to have the top

reinforcement in the middle of the 10.2 cm (4 in) link slab. The bottom clear cover criterion is selected based on section S5.12.3 of AASHTO LRFD.

Table 2.1 *Reinforcement details for the deck slab*

	Top	**Bottom**
Longitudinal Rebars	#4@ 12 in c/c	#6@ 10 in c/c
Transverse Rebars	#6@ 10 in c/c	#6@ 10 in c/c

The bridge deck is connected to the steel girder using shear studs. The shear studs in the entire girder are of 2.22 ×17.8 cm (7/8×7 in), except for the link slab portion where the steel shear studs are of 2.22 × 10.2 cm (7/8×4 in) size. This is to ensure that the shear studs do not affect the debonded length in the link slab. The shear studs are designed following the AASHTO LRFD design procedure for the design of shear studs.

2.2.2 Link Slab Design

The link slab is designed using the procedure provided by Caner & Zia, 1998 and modified by Ulku et al. (2009) that includes considering the spans individually as simply supported beam and finding the end rotations for a design live load of AASHTO HS-93L truck. The design end rotation is calculated considering the girders to be simply supported. The design moment (M_{LL}) induced in the link slab is then calculated using equation (2.1).

$$M_{LL} = \frac{2E_c I_{ls} \Theta_{LL}}{L_{ls}} \tag{2.1}$$

where Θ_{LL} is the end rotation due to the live loading, L_{ls} is the length of the link slab, E_c is modulus of elasticity of concrete, and I_{ls} is the moment of inertia of the link slab.

The moment obtained is then converted to unit strip by dividing it by the width of the slab (i.e., 160 cm (63 in)). The reinforcement ratio is then calculated for the unit strip moment considering a conservative working stress (e.g., 40% of yield strength of steel) as per AASHTO standard specifications section 8.15.2 and also suggested in the design procedure from Caner & Zia (1998).

The stress in the steel reinforcement (f_{steel}) is determined by the equation originally provided by Caner & Zia (1998) and later modified by Ulku et al. (2009).

$$f_{steel} = \frac{M_{LL}}{A_{steel} \times d \times (1 - \frac{k}{3})} \tag{2.2}$$

where k is the factor for getting neutral axis distance kd , and can be calculated by,

$$k = -n\rho + \sqrt{(n\rho)^2} + 2(n\rho) \tag{2.3}$$

where ρ is the reinforcement ratio, n is modular ratio, and d is the distance of reinforcement from the bottom surface of the slab.

The allowable stress in steel ($f_{a\ steel}$) is then calculated using the crack width parameter Z = 130 kip/in often considered for severe exposure condition.

$$f_{a\ steel} = \frac{Z}{(d_c A)^{1/3}} \leq 0.6\, fy \tag{2.4}$$

where d_c is the concrete cover measured from the extreme tension fiber to the center of nearest rebar level, and A is the area of concrete having the same centroid as the principal tensile

reinforcement and bounded by the surfaces of the cross-section and a straight line parallel to the neutral axis, divided by the number of bars (in^2). It should be noted that for the crack width to remain less than 0.33 mm (0.013 in), the allowable stress in the steel obtained from the Equation (4) must be less than 60 % of the steel's yield strength (0.6 f_y).

From the previous field investigations on the constructed link slabs (Wing et al., 2005, Au et al., 2013), it has been shown that link slabs' ends never reach the design rotation under live loadings, but rather they can go beyond design rotation under thermal loadings. In contrast, Hulsey, 1992, found that thermal stress does not induce maximum rotation in the length between the expansion joints. The design strain because of thermal variation can be calculated by the procedure provided of AASHTO LRFD S3.12.2.2. The linear strain induced in the link slab due to the variation of temperature can then be estimated by:

$$\Delta\varepsilon_T = \frac{\alpha_T.\Delta T.L_{sp}}{L_{ls}} \qquad (2.5)$$

where α_T is the coefficient of thermal expansion, ΔT is the annual temperature variance, L_{sp} is the length of the debonded region of link slab (i.e., 5% of the span length), and L_{ls} is the total length of the debonded region of link slab.

It is highly desirable to design the link slab with low stiffness, as it is supposed to act as a pin connection linking the two spans. The low stiffness can be also achieved by providing a debonding length using plastic sheeting or roofing paper in the debonded zone.Plastic Sheeting is usually used when the two surfaces to be debonded are concrete, and roofing paper is used for debonding concrete and steel surfaces. Plastic sheeting is used in this project because the two surfaces to be debonded are concrete. As mentioned earlier, shorter shear studs

are provided to make the debonding possible. Two link slabs are constructed with different types of rebar, namely steel, and GFRP rebars, hereafter referred to as LS-1 and LS-2, respectively.

2.2.2.1 Design Details of Link Slab 1 (LS-1)

The LS-1 is designed based on the procedure discussed above and it mainly consists of two parts: bonded and debonded zone. The region just before the debonded region from both sides is called the bonded region which is densely reinforced as compared to the debonded region which allows transferring the stresses from the deck to the debonded region of the link slab. Alternating reinforcement of length 91 cm (36 in) is added to both sides of the debonded region to provide more stiffness so that the forces can be transferred to the debonded region. The detailing selected for this specimen is mainly based on the recommendations made by Lárusson et al. (2013). The debonded length is taken as 5 % of the span length as recommended by the previous investigations (Au & Tharmabala, 2013, Caner & Zia, 1998, Okeil & Elsafty, 2005, Ulku et al., 2009). Figure 2.3 shows the detailing of the link slab, as well as the bonded and debonded regions. The reinforcement detail included in the link slab consists of #6 longitudinal rebars with 17.8 cm (7.0 in) center-to-center spacing in the unbonded region. This spacing is reduced to half, i.e., 8.9 cm (3.5 in) in the bonded region.

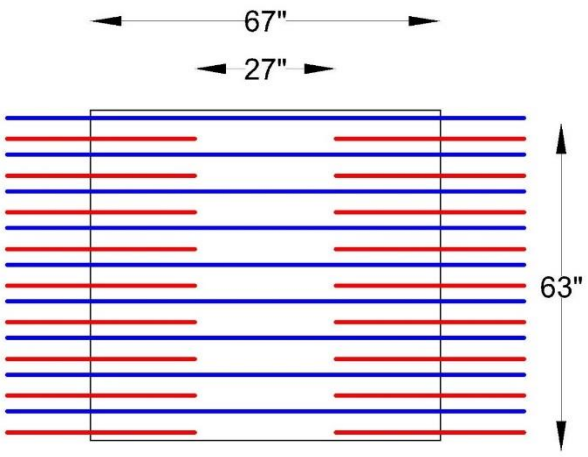

Figure 2.3 *Link slab 1 details*

Figure 2.4 *View of link slab 1 constructed in the laboratory*

2.2.2.2 Design Details of Link Slab 2 (LS-2)

The LS-2 is designed with GFRP rebars. GFRP rebars are corrosion resistant and have a lower modulus of elasticity than steel rebars, which makes them a viable material to be used

in link slabs. The GFRP rebars from the debonded region are extended into the bonded region. The top longitudinal rebars from the bridge deck are extended into the bonded region. The region just before the debonded region from both sides is called the bonded region which is densely reinforced with aa combination of GFRP rebar from link slab and extended top steel rebars, as compared to the debonded region to transfer the stresses from the deck to the debonded region of the link slab. Figure 2.5 shows the reinforcement detailing in LS-2. The blue rebars show the longitudinal #6 GFRP rebar provided at 20.3 cm (8in) center to center in the link slab and the red lines show the top longitudinal steel rebars (#4 @ 30 cm (12 in) c/c) from concrete deck extending into the link slab. Figure 2.6 shows the LS-2 reinforcement mat constructed in the laboratory.

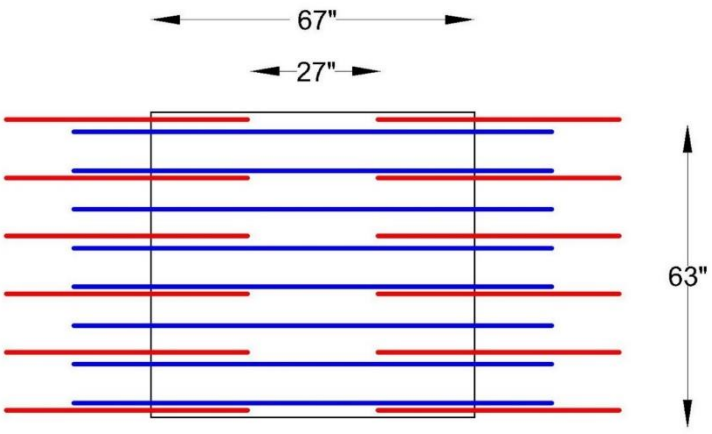

Figure 2.5 *Reinforcement detailing in Link Slab 2*

Figure 2.6 *Link slab 2 as constructed in the laboratory*

2.2.3.1 Instrumentation for LS-1

The bridge superstructure made is instrumented with strain gauges mounted on rebars in critical locations identified by preliminary finite element analysis to monitor the evolution of strains induced in the reinforcement during the loading. The strain gauges are installed on the top layer of reinforcement over the support in the deck approaching link slab, on the rebars inside the bonded zone, and on the reinforcements in the debonded zone. This is to monitor the difference in strains between the deck and the bonded zone, as well as between the bonded and debonded zone. The difference of strain between bonded and debonded zone will provide invaluable insight into the effectiveness of the bonded zone in transferring forces to the debonded zone. The difference of strain between the bonded and debonded zones will also show the effectiveness of debonding in releasing moments in the link slab.

A separate set of strain gauges are placed inside the concrete to measure the strain variations in the concrete during the loading. The strain gauges are placed at 10.2 cm (4 in) and 15.2 cm (6 in) from the bottom surface in the bonded region, and in the debonded region, at 15.2 cm (6 in) from the bottom of the slab. This is to monitor the strain variation along the depth of the link slab in both the bonded and debonded regions. Moreover, two surface strain gauges are placed at the top of the debonded surface spaced at 30 cm (12 in) from the centerline of the link slab, under the plastic sheeting. Additionally, surface strain gauges are also installed on the surface of the link slab and that of the finished deck. Six linear differential variable transformers (LVDTs) are installed on the steel girder, three on each girder to monitor the curvature of the girder under different support conditions. The instrumentation and debonding of link slab are shown in Figure 2.7. Three direct current displacement transducers (DCDTs) are also installed to measure crack width across the centerline of link slab, and at the line where bonded and debonded regions meet. The LVDT's and surface strain gauges can be seen in Figure 2.8.Figure 2.9 shows the surface strain gauges. Figure 2.10 shows the strain gauges at the level of debonded layer at 10.2 cm (4 in) from the bottom surface. The blue rectangles represent the embedded strain gauges. Figure 2.10 shows the strain gauges at the rebar level.

Figure 2.7 *Instrumentation and debonding of the link slab portion*

Figure 2.8 *DCDT's and surface strain strain gauges on link slab 1*

Figure 2.9 shows the surface strain gauges. Figure 2.10 shows the strain gauges at the level of debonded layer at 4 in from the bottom surface. The blue rectangles represent the embedded strain gauges. Figure 2.11 shows the strain gauges at the rebar level

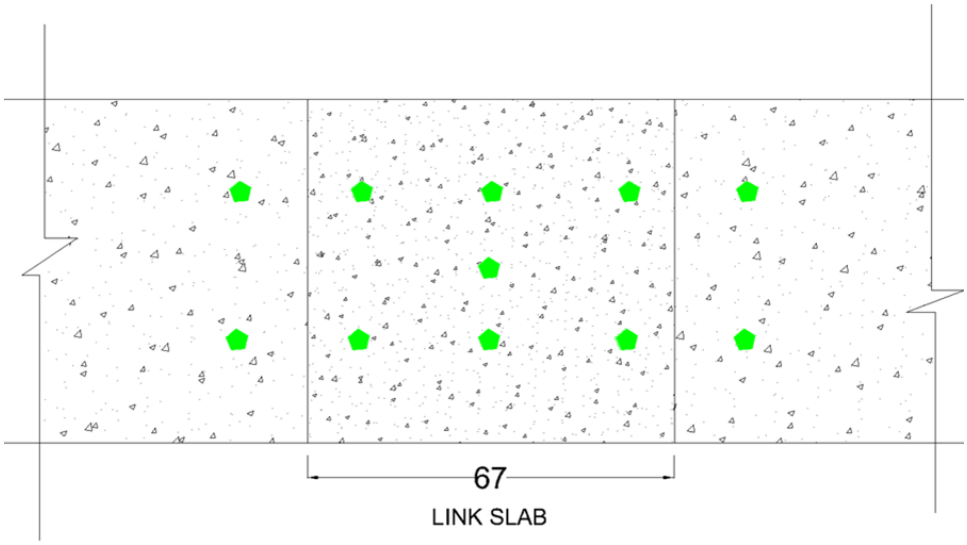

Figure 2.9 *Surface strain gauges in LS-1*

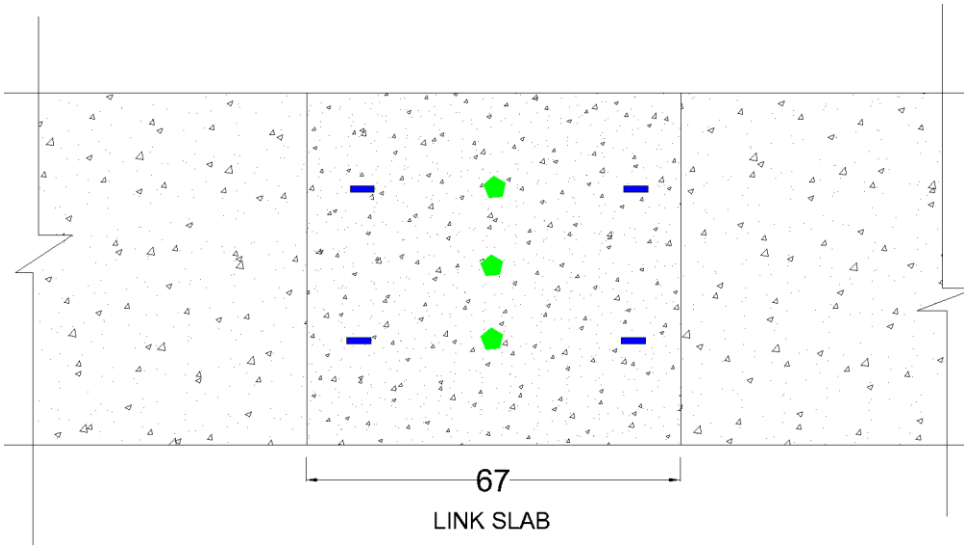

Figure 2.10 *Strain distribution at 4 in from bottom in the LS-1*

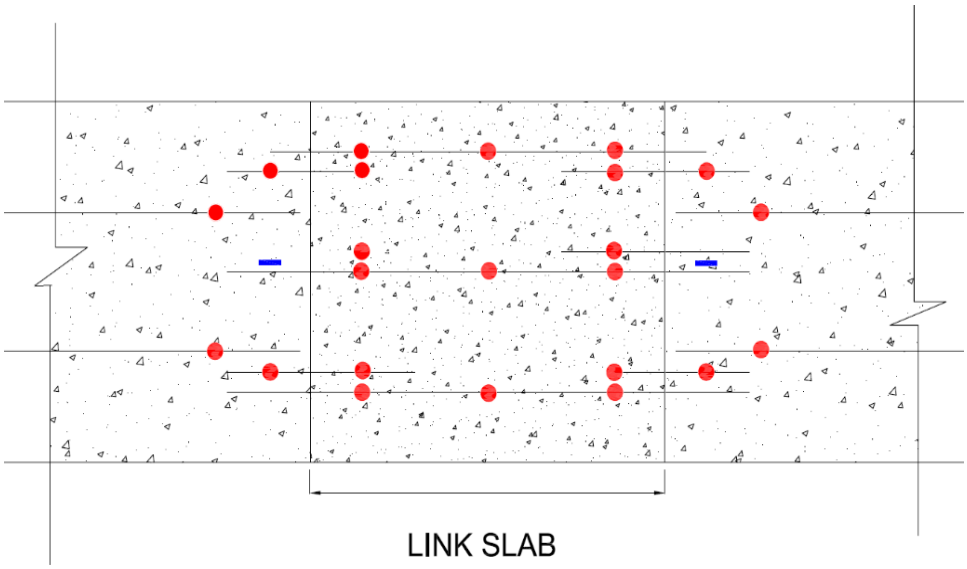

Figure 2.11 *Strain gauges on the rebars in LS-1*

2.2.3.2 Instrumentation for LS-2

The instrumentation on link slab consisted of surface strain gauges, strain gauges on rebars, embedded strain gauges, LVDTs and DCDTs. Two strain gauges are installed on the GFRP rebars in the debonded region and two in the bonded region. Two strain gauges are also installed on the longitudinal steel rebars in the bonded region. The strain gauges are also mounted on the bottom rebars in the link slab and under the loading points. Concrete embedded strain gauges are also installed in the bonded region one on each side. Concrete surface strain gauges are placed on the top of the concrete deck in the debonded region and on top of the FRC link slab in the bonded and debonded regions as well as on the bridge deck. The strain gauges installed on the link slab's surface are shown in Figure 2.12 and are represented by a green polygon. Two surface gauges are also installed on top of the debonded surface at 4 in from the bottom of the slab as shown in Figure 2.13.

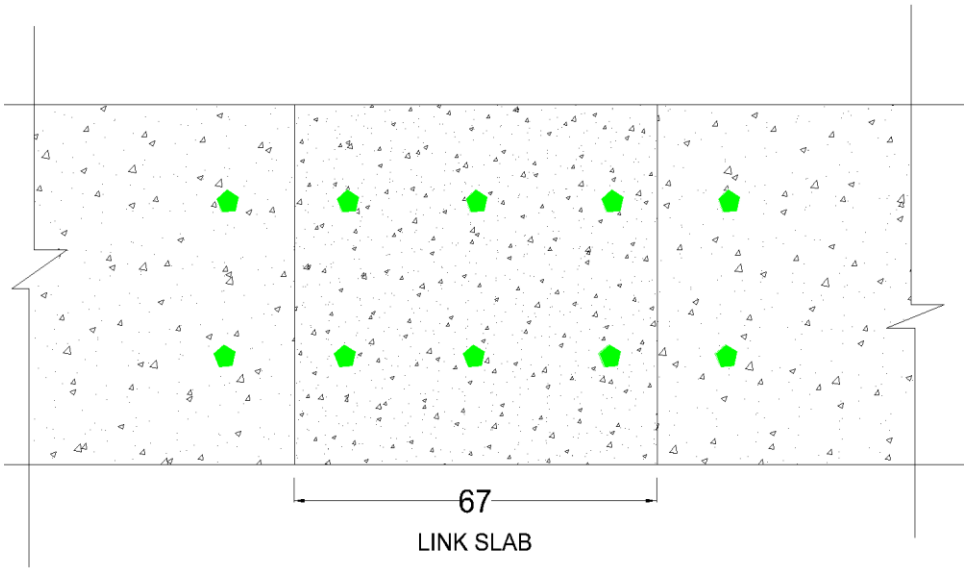

Figure 2.12 *Surface strain gauges in LS-2*

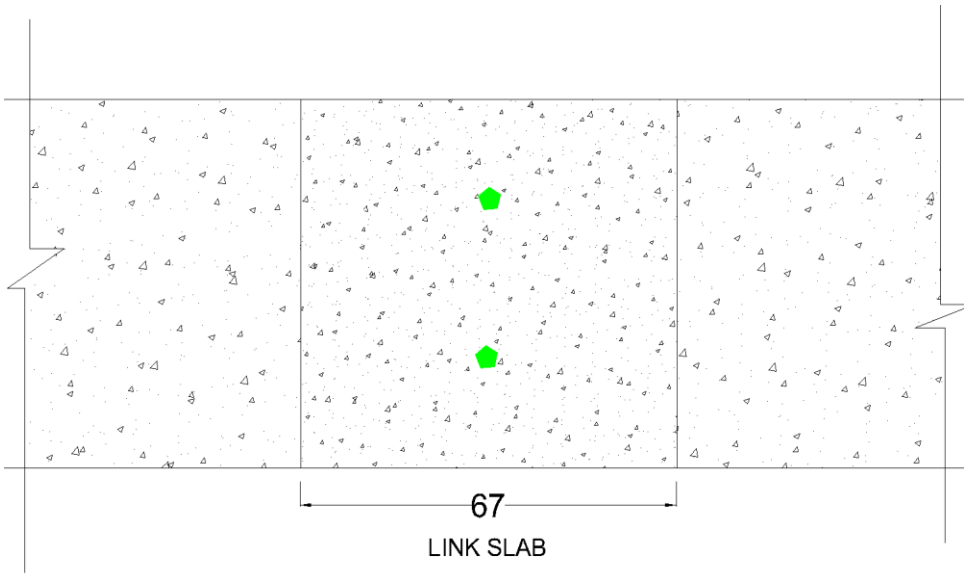

Figure 2.13 *Strain gauges at 4 in from bottom*

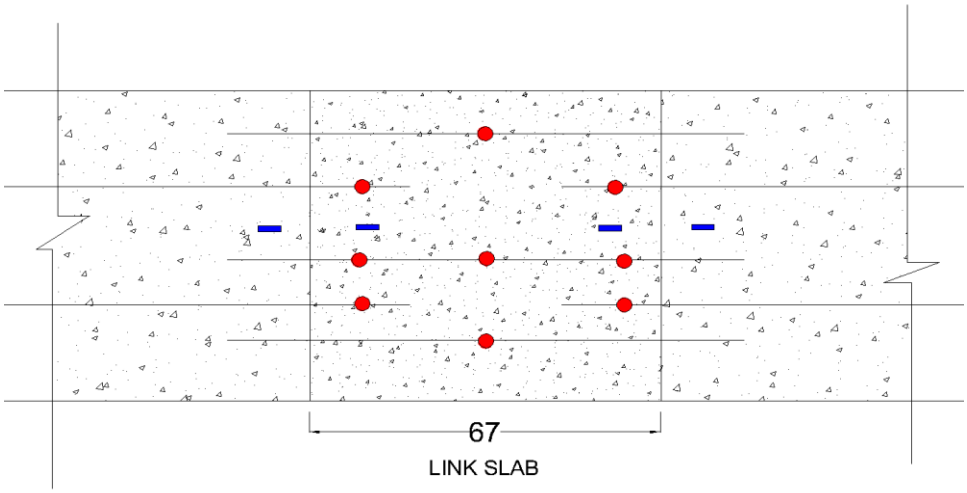

Figure 2.14 *Strain gauge distribution at rebar level in LS-2*

2.3 Testing Procedure

The two specimens were tested by loading them at the center of both spans by an actuator with a loading capacity of 1068 kN (240 kip). The Structure is loaded until failure. The laboratory test setup and arrangement can be seen in Figure 2.15.

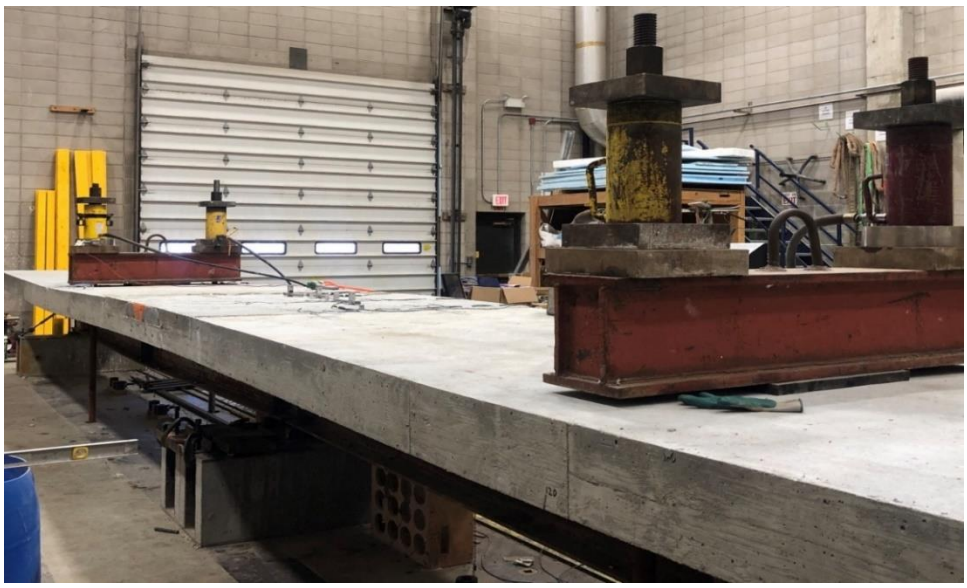

Figure 2.15 *Laboratory Test Setup Showing Actuators on Loading Points*

2.3.2 Testing procedure of LS-2

From the experimental results of LS-1, the most critical support condition (RPPR) is identified. The LS-2 specimen is tested only for RPPR support condition by loading the structure at the middle of both girders. The structure is then loaded till failure.

2.4 Results for LS-1

The test results for link slab include the load-deflection curves, the load-crack width curves and the crack distributions.

2.4.1 Load Deflection Curve

The structure is loaded until failure for RPPR support condition, where R refers to roller and P refers to pin support condition. The ultimate load observed is 979 kN (220 kip). It can be seen that the structure behaves elastically till 444.8 kN (100 kip) of loading, after which a plastic response is witnessed (Figure 2.16).

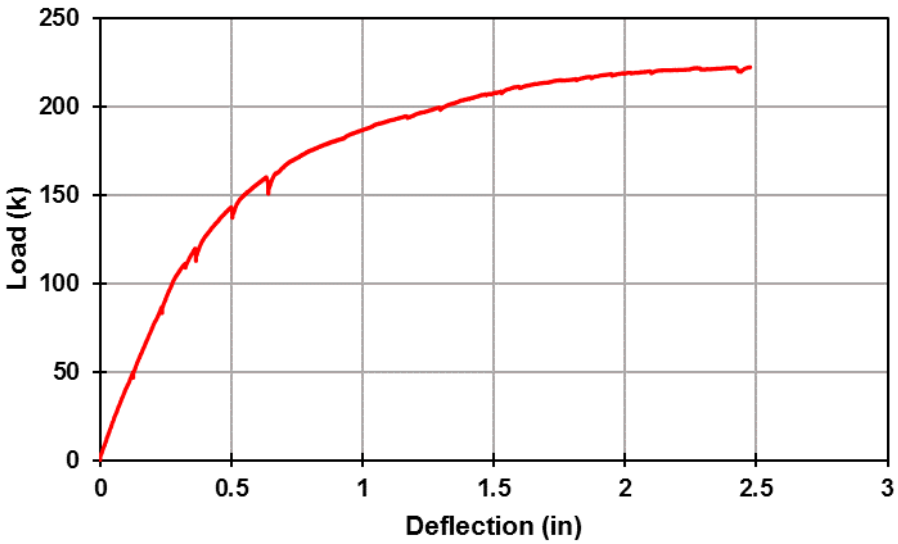

Figure 2.16 *Load-Deflection curve for LS-1*

2.4.2 Crack Width and Crack Propagation

The crack widths are monitored by Direct Control Displacement Transducers (DCDT). The first crack initiates through the middle of the debonded region recorded by DCDT-2. The crack width against load is shown in the Figure 2.17. This crack width reaches the AASHTO standard crack limit of 0.33 mm (0.0013 in), when the load reaches 120 kips.

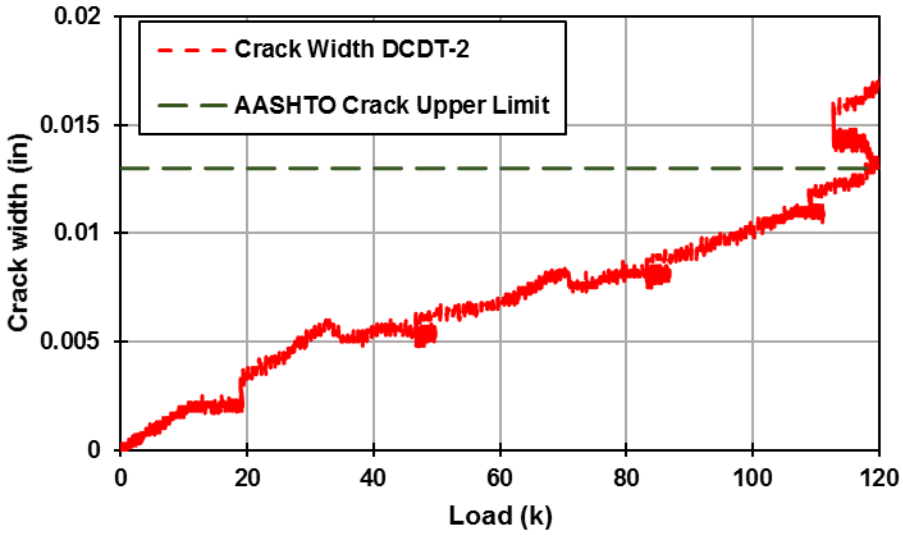

Figure 2.17 *Crack width on top of Link Slab versus Load*

Two additional cracks follow the first crack across the link slab and recorded by DCDT-1 and DCDT-3, at the spots where bonded region ends and debonded region starts. The DCDT-1 and DCDT-3 are presented in Figure 2.18. It can be seen that the cracks reach standard AASHTO limits at 533.8 kN (120 kip) and 622.8 kN (140 kip) for DCDT-1 and DCDT-3 respectively. The cracks can be seen in Figure 2.19. These cracks also extend down to the surface of concrete deck when the load reaches 383 kN (86 kip) (Figure 2.20).

Majority of the cracks are located in the debonded region. At ultimate there are a few cracks in the bonded region, which shows that the debonding and the dense provision of

reinforcement in the bonded region performed as intended. Since all the cracks run straight across the link slab, it can be concluded that the cracks are formed because of flexural loading.

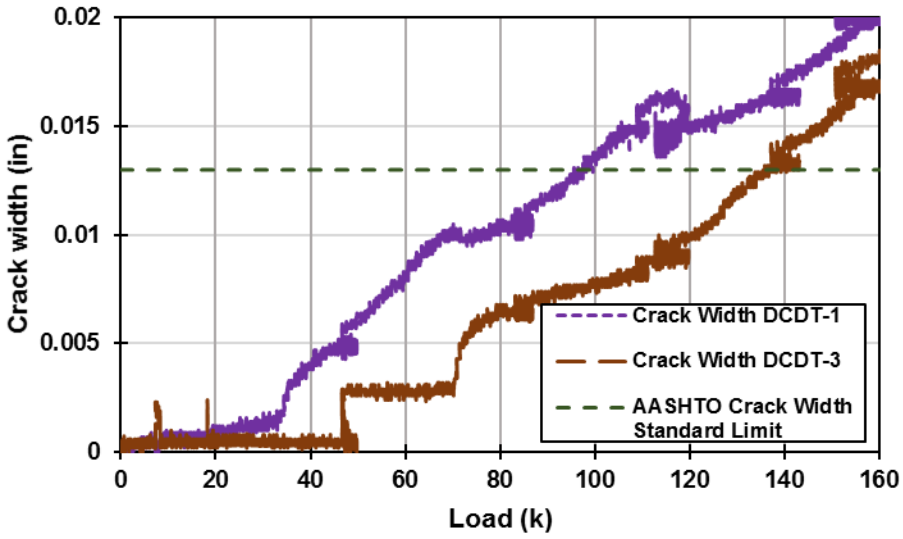

Figure 2.18 *The crack width from DCDT-1 and DCDT-3*

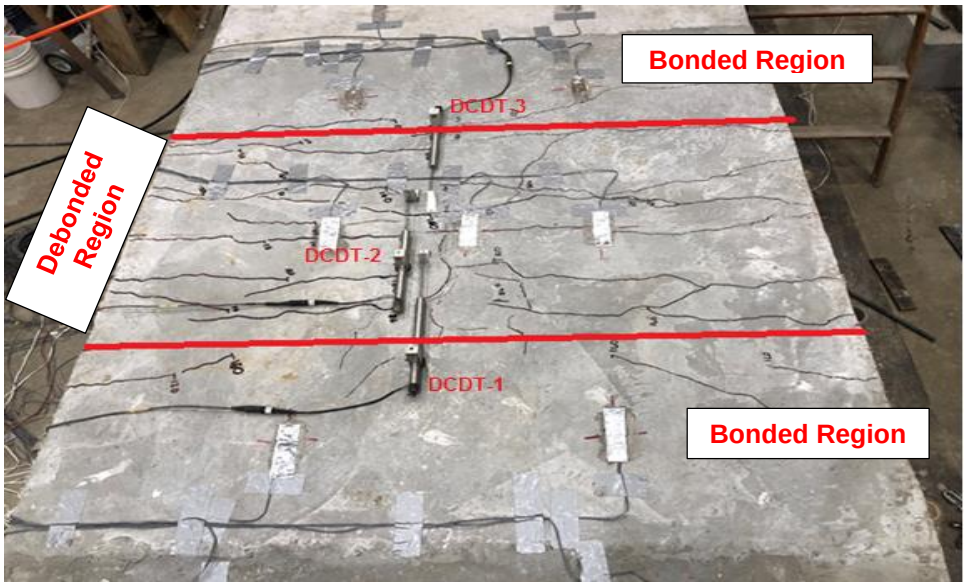

Figure 2.19 *Crack Pattern in the LS-1 at ultimate Loading*

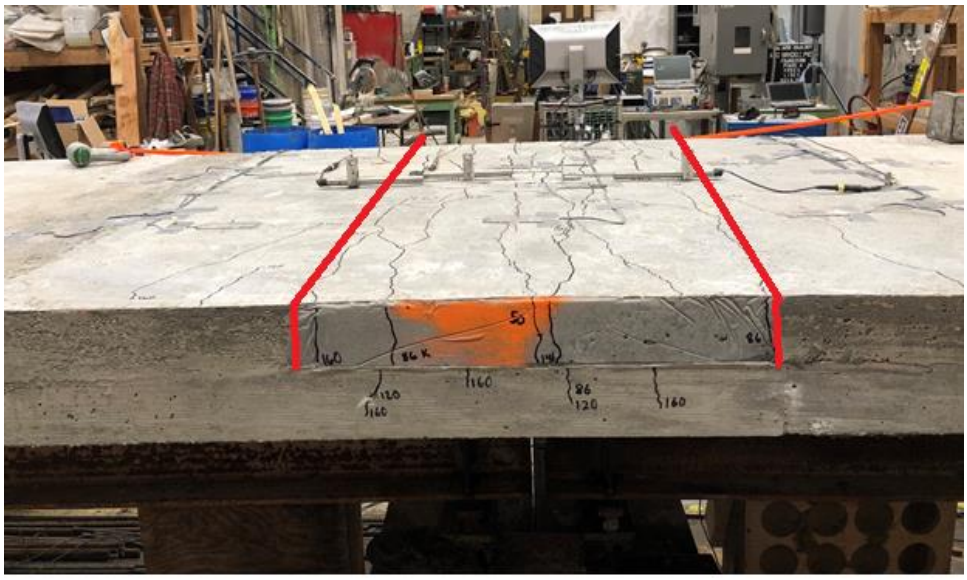

Figure 2.20 *Crack Pattern in the LS-1 at maximum loading (Side View)*

2.5 Results for LS-2

2.5.1 Load Deflection Curve

The link slab 2 (LS-2) is tested by loading the structure at midspan of the two spans using two actuators on each sides. The support conditions for LS-2 are RPPR, as it is the most critical support condition for stresses developed in the link slab. Figure 2.21 shows the load deflection curve for the link slab. The load-deflection curve shows that the structure behaved linear elastically till 489 kN (110 kips) after that the structure enters in plastic load deflection response. The load strain curve for the strain in the rebar at the middle of the slab is shown in the Figure 2.22. The load strain curve is linear till 444.82 kN (100 kip) and the rebar exhibits plastic deformation after 444.82 kN (100 kip). This plastic behavior can be attributed to the combined action of GFRP and FRC, as the FRC has some tensile capacity because of the fibers.

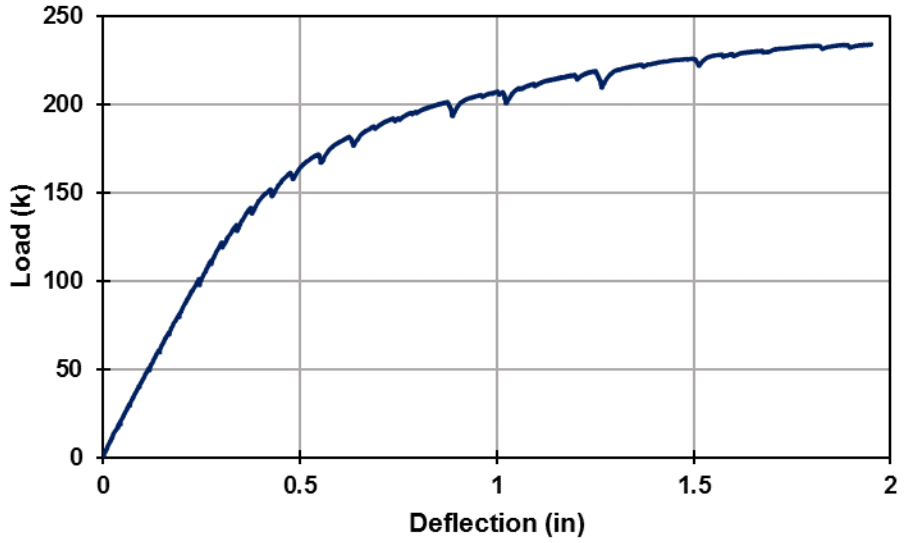

Figure 2.21 *Load deflection curve for Link Slab 2*

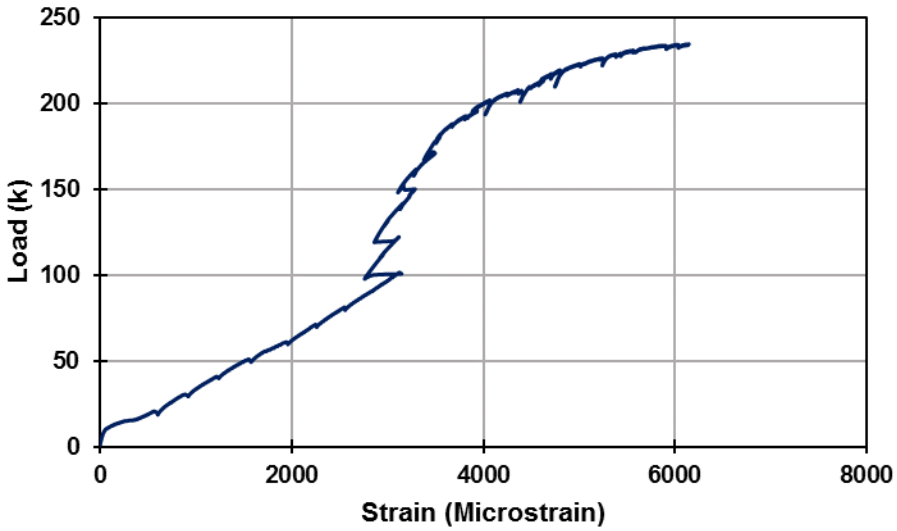

Figure 2.22 *Load strain curve for top rebar in the debonded region of the link slab-2*

2.5.2 Crack Width and Crack Propagation

The crack widths are measured by using three DCDTs mounted on the top of the link slab. The first crack extending through the center of the debonded region and picked up by DCDT-2 appeared soon after the loading start. The crack reached the AASHTO standard limit

of 0.33 mm (0.013 in) at 258 kN (58 kips). The crack width is shown against load in Figure 2.23.

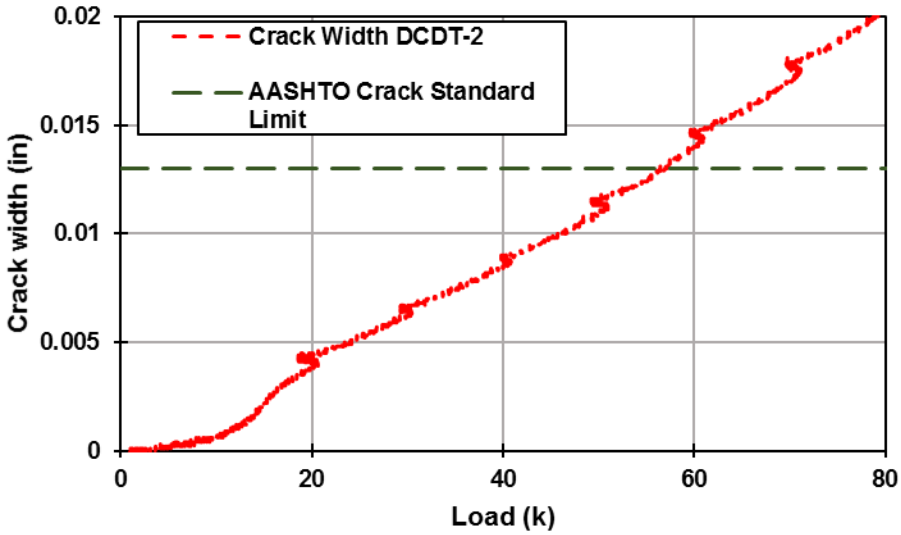

Figure 2.23 *Crack width versus load plot for DCDT-2*

The DCDT 1 and DCDT 3 measures the crack width for cracks that followed the first cracking. The readings from DCDT-1 and DCDT-3 are plotted against load in Figure 2.24. It can be seen that the second and third crack reached the AASHTO limit at 556 kN (125 kips) and 979 kN (220 kips) respectively. The cracking patterns are shown in the Figure 2.25 and Figure 2.26. It can be observed that the almost all cracks are consolidated in the debonded region. Three cracks ran all the way across the link slab, while there are other fine interconnecting cracks, which is a typical FRC behavior. Almost all cracks are flexural cracks except for a diagonal crack, similar to a shear crack, is seen on opposite end of debonded region on both side. This cracks may be because of the improved pin connection (In LS-1 some movement of the support under the link slab was observed indicating the support did not behaved as true pin) under the link slab which is restricting the motion of support under debonded region, although no such crack is observed in LS-1.

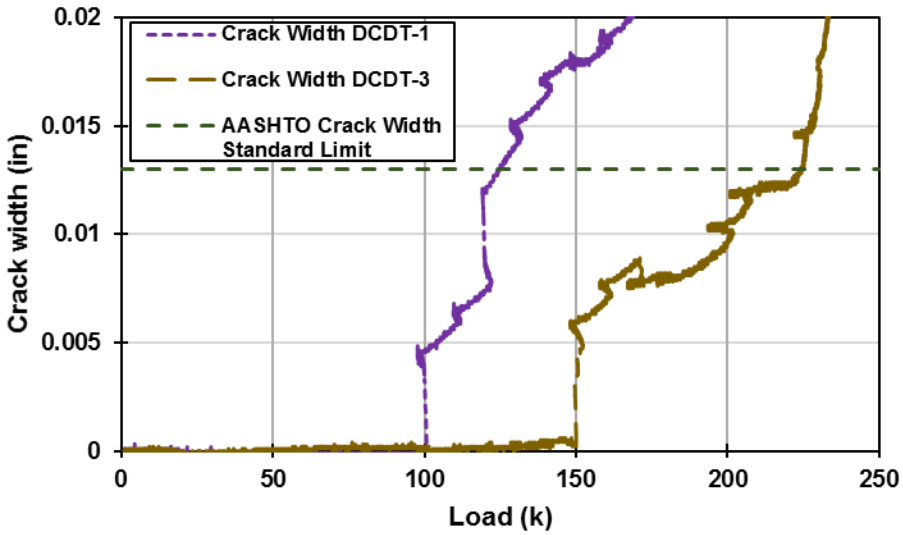

Figure 2.24 *Crack width versus load plot for DCDT-1 and DCDT-3*

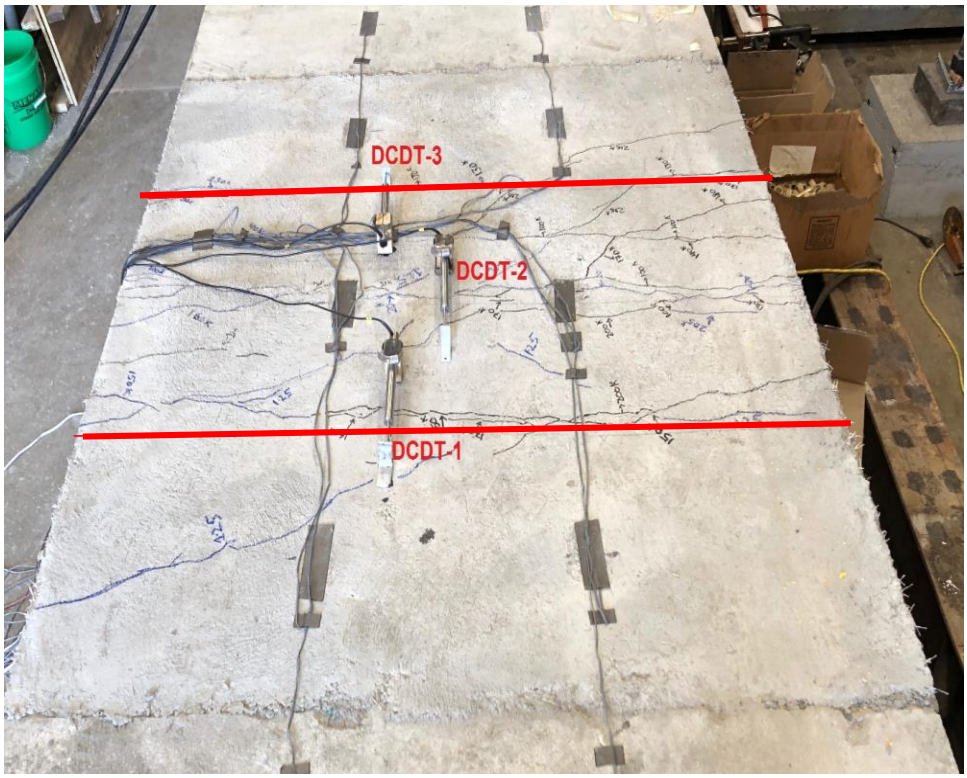

Figure 2.25 *Cracking pattern in LS-2*

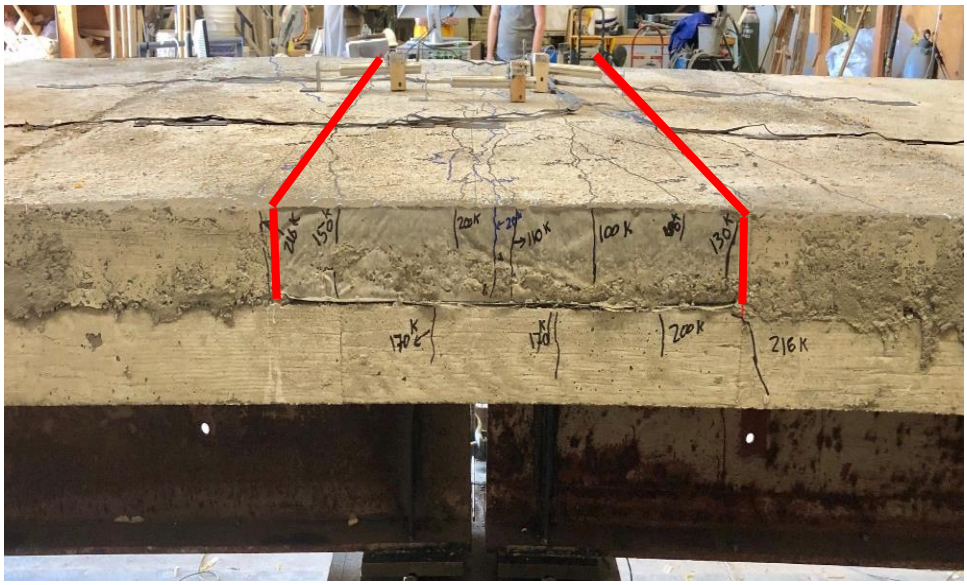

Figure 2.26 *Cracking pattern in LS-2 side view*

2.6 Comparison of the Test Results

The results of the two link slab test setups are compared below. The results for link slab 1 are represented by LS-1 and for link slab 2 are presented by LS-2.

2.6.1 Load-Deflection and Load- Strain Curves

The load deflection curves follow the same trend initially but eventually it can be seen in Figure 2.27 that the load-deflection curve for LS-2 is stiffer than that for LS-1. This indicates that the overall structure for the second specimen is stiffer than the first specimen, this does not necessarily mean that the second link slab is stiffer than LS-1. The entire structure is stiffer because the pin connection under the link slab behaved as true pin in the second specimen, while for first test supports under link slab moved, resulting in a structure with lower rigidity as a whole. A comparison of load and strain in the bottom rebar of the concrete slab under the loading point shown in Figure 2.28, highlights that for both link slabs the curves follow the

same path, highlighting the fact that even though the deflections at center is different for both link slabs the demand on the link slab is similar.

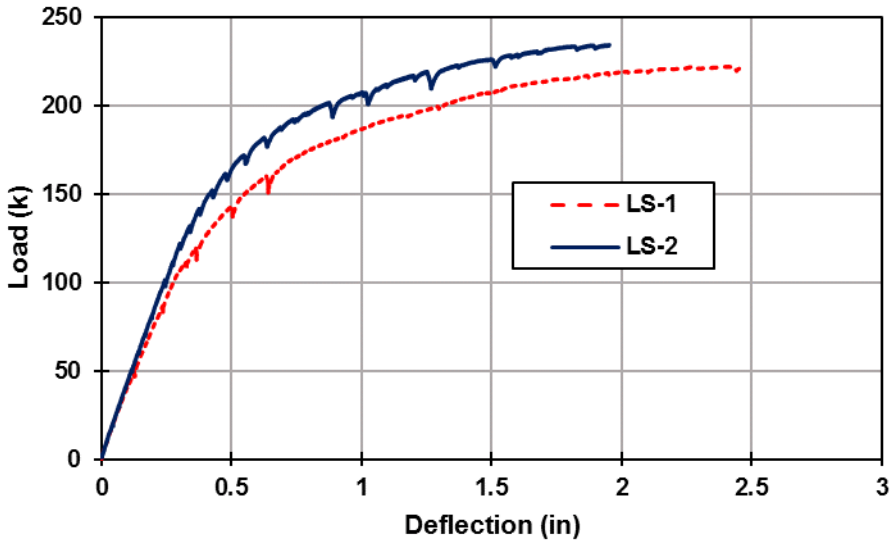

Figure 2.27 *Comparison of load-deflection curves.*

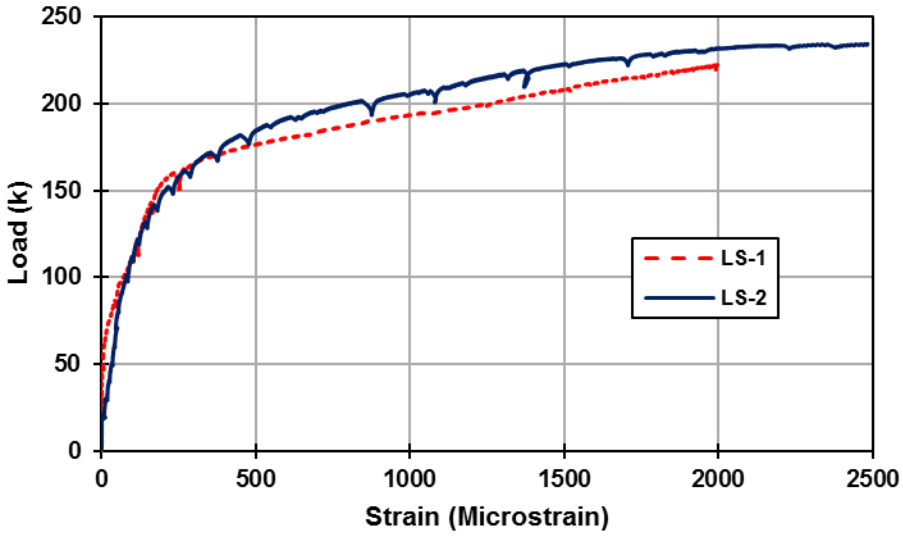

Figure 2.28 *Load against strain in the bottom rebar at mid span of concrete deck*

The comparison of load-strain curves for strain in top rebar in debonded region is shown in Figure 2.29. It shows that the LS-2 is more flexible then LS-1. It can be seen that for

a load of 444 kN (100 kips) the LS-1 experiences a percent strain of less than 0.01 while the strain percentage for GFRP rebar at the same loading is 0.3%. The steel rebar in LS-1 starts to go into plastic range after 200 kN (45 kip). The top GFRP rebar in LS-2 had a strain hardening effect at 444 kN (100 kips) (0.3% strain), which can be because of the tensile capacity of FRC and a combined action of GFRP and FRC, and it continued to take more strain as the ultimate tensile capacity of a GFRP rebar is 2.5%.

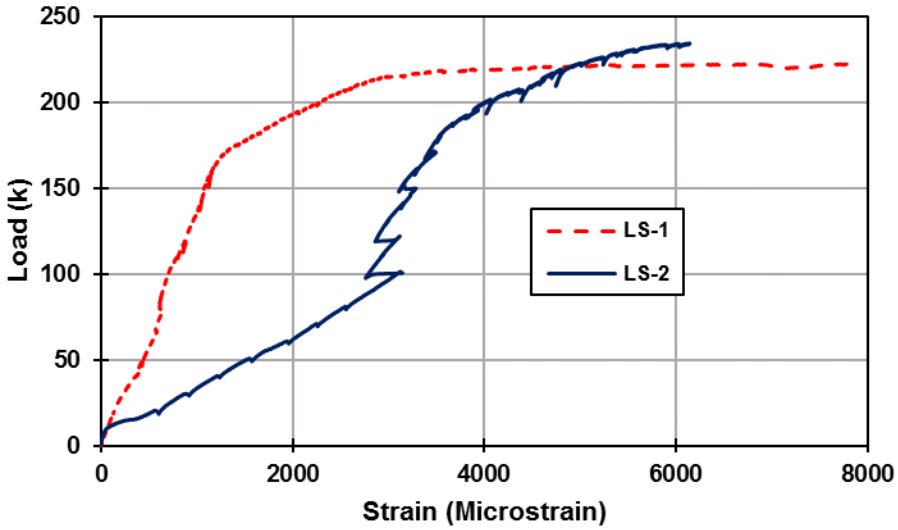

Figure 2.29 *The load strain curve for the top rebar in debonded region*

The load-strain curve for the strain recorded by surface strain gauge placed on top of the debonded region shows a similar trend (Figure 2.30). A strain hardening effect occurs at 3000 microstrains for LS-2, and the load strain curve shows that the behavior of the LS-2 is more flexible than that of LS-1, which agrees with the theoretical understanding as GFRP rebar has lower modulus of elasticity than steel rebar.

A comparison of load-strain curve for rebar in bonded region is shown in Figure 2.31. It can be seen that the GFRP rebar in LS-2 observes very small strain (40 Microstrains) as compared to the steel rebars in LS-1.The strain for steel rebar in LS-1 is significantly higher

for same amount of load at each stage. This highlights the fact the rebars in the bonded region of LS-1 is under greater stress than the rebars in LS-2, this can be because of the fact that the LS-1 experienced more deflection than the LS-2, thus the bonded region will be under more stress for LS-1 than LS-2.

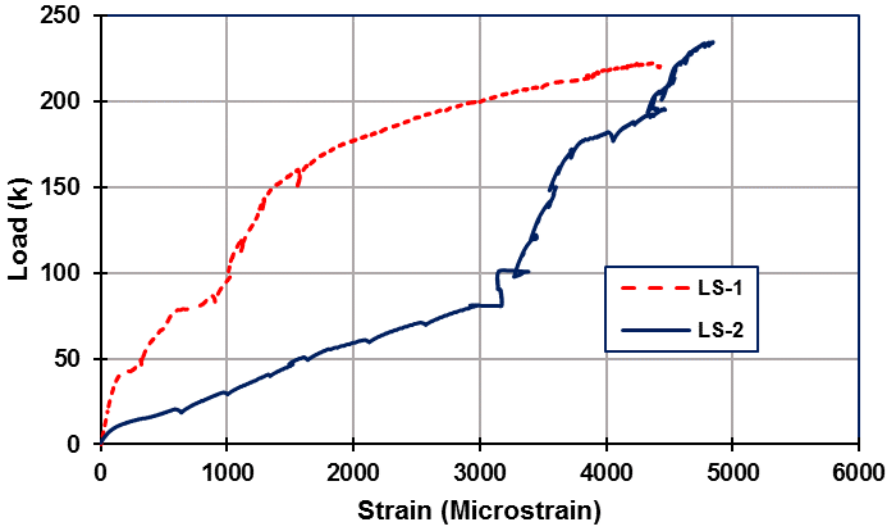

Figure 2.30 *The load strain curve for the surface strain gauge on top of debonded region*

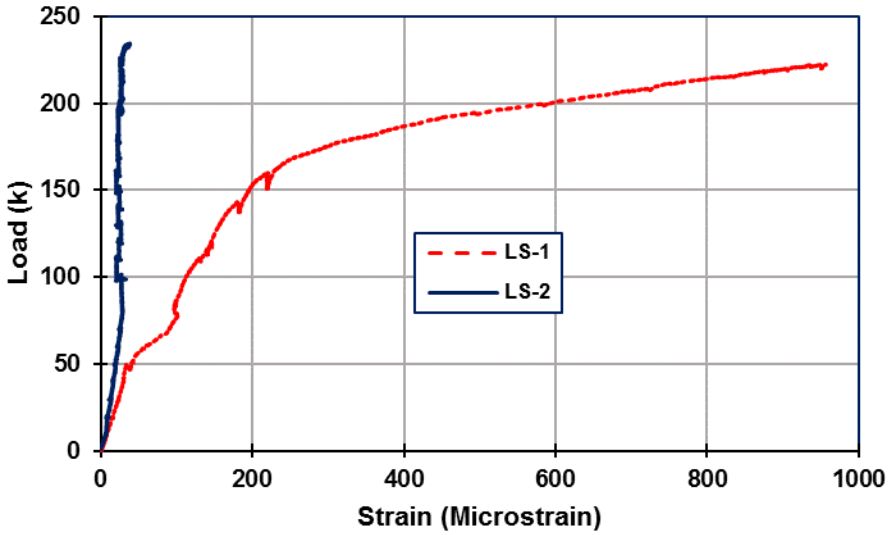

Figure 2.31 *Load-Strain Curve for the rebar in bonded region*

2.6.2 Crack Width and Crack Propagation

The first crack width is recorded by DCDT-2 for both link slabs. The crack initiates at middle of the debonded length of the link slab. The crack width for the first crack reaches AASHTO limit of 0.33 mm (0.013 in) at 534 kN (120 kips) and 258 kN (58 kips) for LS-1 and LS-2, respectively, as can be seen in Figure 2.32.

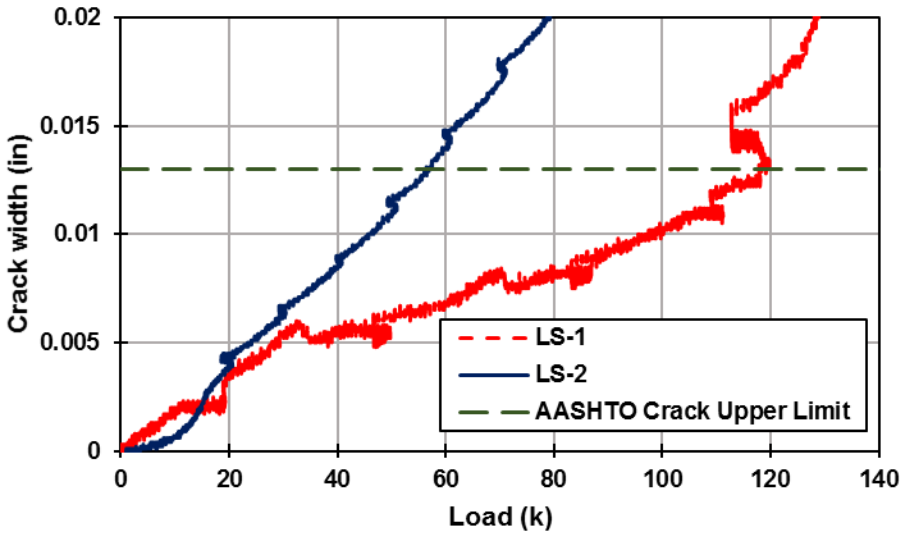

Figure 2.32 *The crack width comparison for DCDT-2 in LS-1 and LS-2*

DCDT-1 and DCDT-3 record the crack width for the cracks that follow the first crack. The comparison of results for DCDT-1 (Figure 2.33) shows that the crack widths for the LS-1 reaches the AASHTO Limit before the LS-2. For LS-2 the crack width remains negligible till 444.8 kN (100 kip). A similar trend can be seen in the crack width measured by DCDT-3 for both LS-1 and LS-2 shown in the Figure 2.34. These cracks are followed by finer cracks almost all of them consolidated in debonded region. A diagonal crack, similar to a shear crack on opposite end of debonded region on each side is observed, no such crack is formed in LS-1.

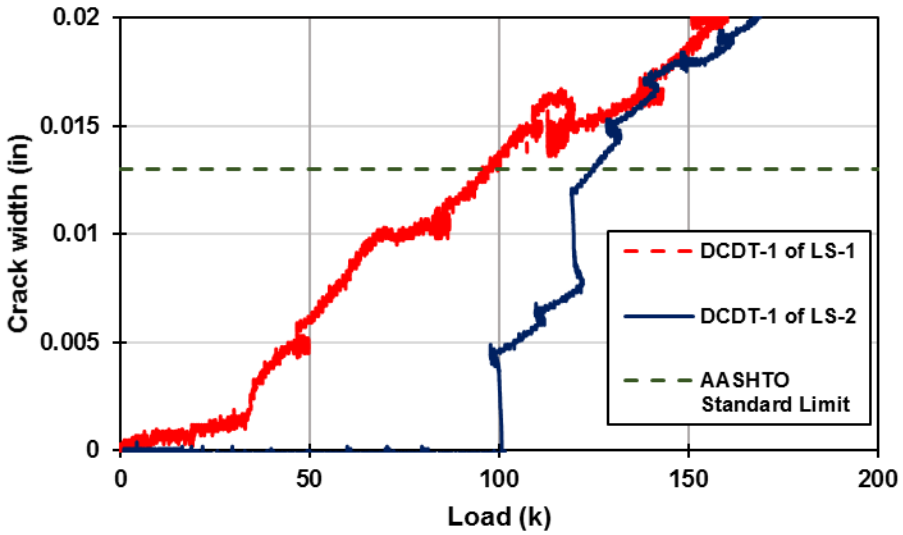

Figure 2.33 *The comparison of crack width for DCDT-1*

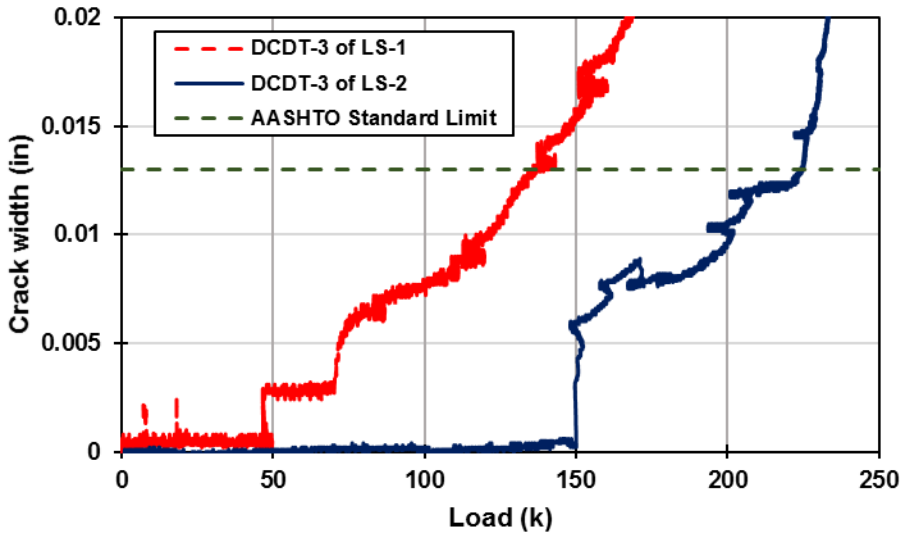

Figure 2.34 *The comparison of crack width for DCDT-3*

2.7 Numerical Investigation of Test Setups

The Abaqus CAE is used to make the finite element model for both the link slabs tested in the laboratory. The steel beams, concrete deck and FRC link slab were modeled using solid element (C3D8R) with hour glass control. C3D8R is a general purpose linear brick element with reduced integration. The reduced integration eliminates the problem of locking

phenomena which happens in C3D8 elements. The rebars were modeled as 2D truss elements. 2D truss element uses a linear interpolation for position and displacement and has a constant stress. The bonding between concrete deck and steel beam was simulated by using Tie constraint. A tie constraint ties two surfaces together such that there is no relative motion between the two surfaces. Tie constraint can be applied even if the meshes are different on the two surfaces. A surface to surface hard contact model in combination with tangential frictionless properties was used for simulating debonding between link slab and concrete deck. This allows for the surfaces in contact to transfer stresses when they are in contact and to separate when the contact stresses drops to zero. The model made in Abaqus CAE is shown in Figure 2.35.

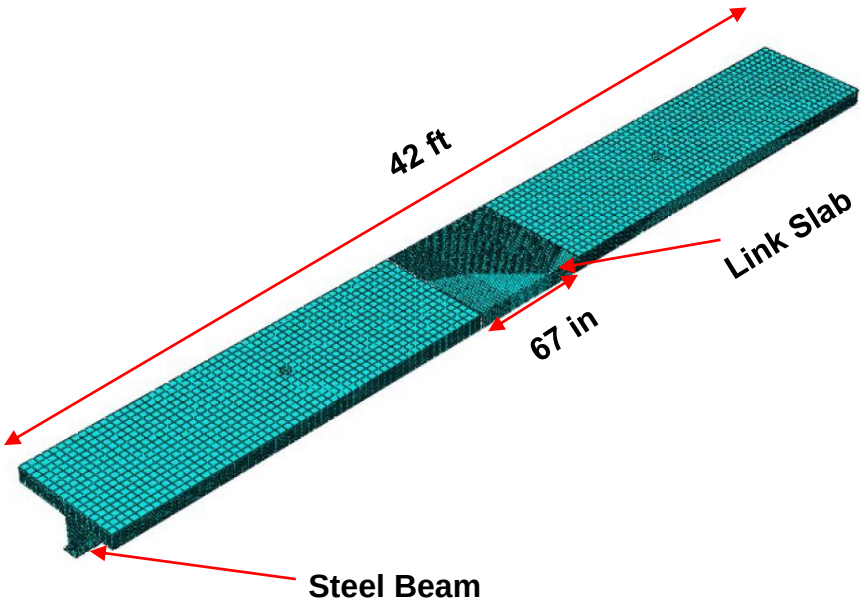

Figure 2.35 *Finite Element Model developed in Abaqus CAE*

The material properties of concrete and FRC were modeled using concrete damage plasticity (CDP) model. The properties were validated by comparing the load-deflection and load-strain curve for the strain in the reinforcement at the midspan with the experimental

results for both link slabs. The model for LS-1 is then used to perform a parametric study by changing the geometry and boundary conditions in the validated model.

2.7.1 Validation Model

The link slab tested in laboratory are modeled in Abaqus CAE. The load deflection curve from finite element modelling and experimental results are shown in Figure 2.36. The results from finite element closely follow the results from experimental testing for both LS-1 and LS-2. This verifies that the results from the model are reliable and the model is replicating the experimental conditions in the laboratory. The load deflection curves showed more rigidity than the actual experimental results.

The rebar in debonded region of the link slab 2 (LS-2) showed the higher strain and softer response overall then the link slab with steel rebars. The similar trend can be seen in the results from finite element analysis (Figure 2.37).

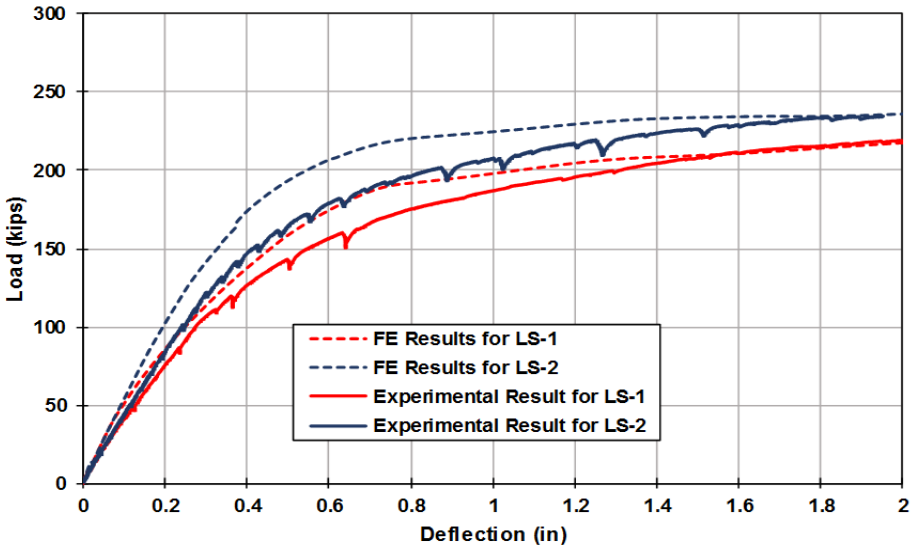

Figure 2.36 *Comparison of results from finite element model and experimental testing*

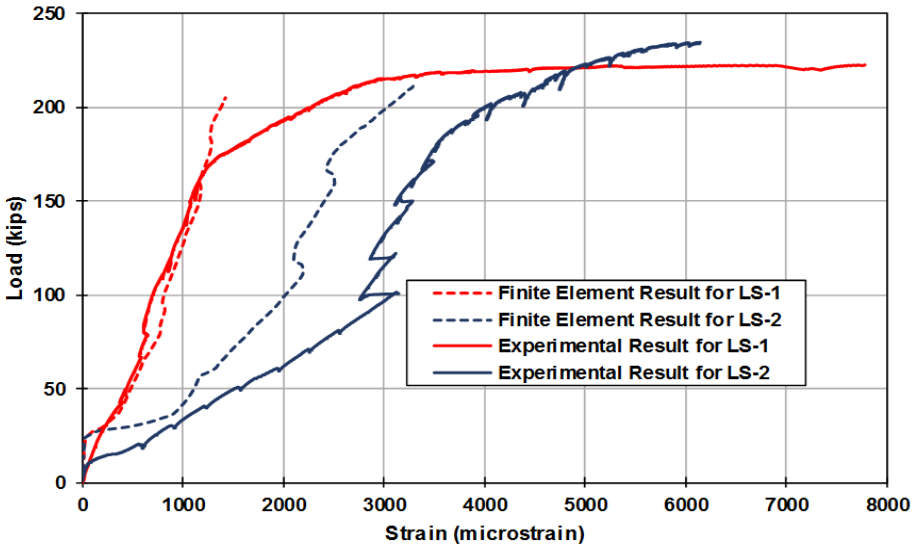

Figure 2.37 *Comparison of strain in rebar in debonded region from experimental and finite*

2.8 Parametric Study

The validated model for link slab 1 was used to carry out the parametric study. Three parameters are studied. The rebar spacing in debonded zone, the rebar spacing in the transition zone and the depth of link slab.

2.8.1 Effect of Rebar Spacing in Debonded Zone of Link Slab

The rebar spacing in the link debonded zone determines the capacity of link slab and its crack controlling ability. The reinforcement provided needs to be enough to control cracking at the same time making the link slab not too rigid.

Three different rebar spacing namely 17.8 cm (7 in), 25.4 cm (10 in) and 33.01 (13 in) are evaluated. The strain increases with increase in the spacing (Figure 2.38). The strain distribution contours can be seen in Figure 2.39.

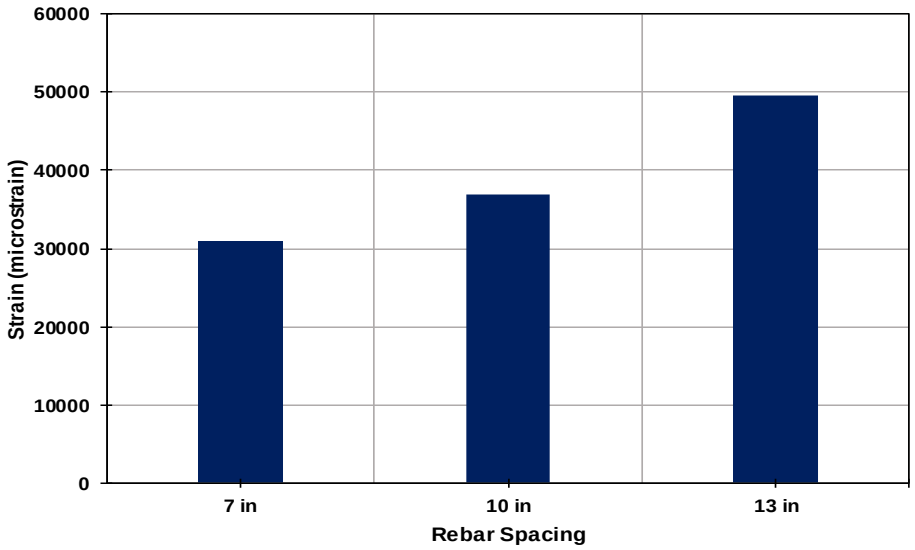

Figure 2.38 *The load strain curves in the rebar located in debonded zone of link slab*

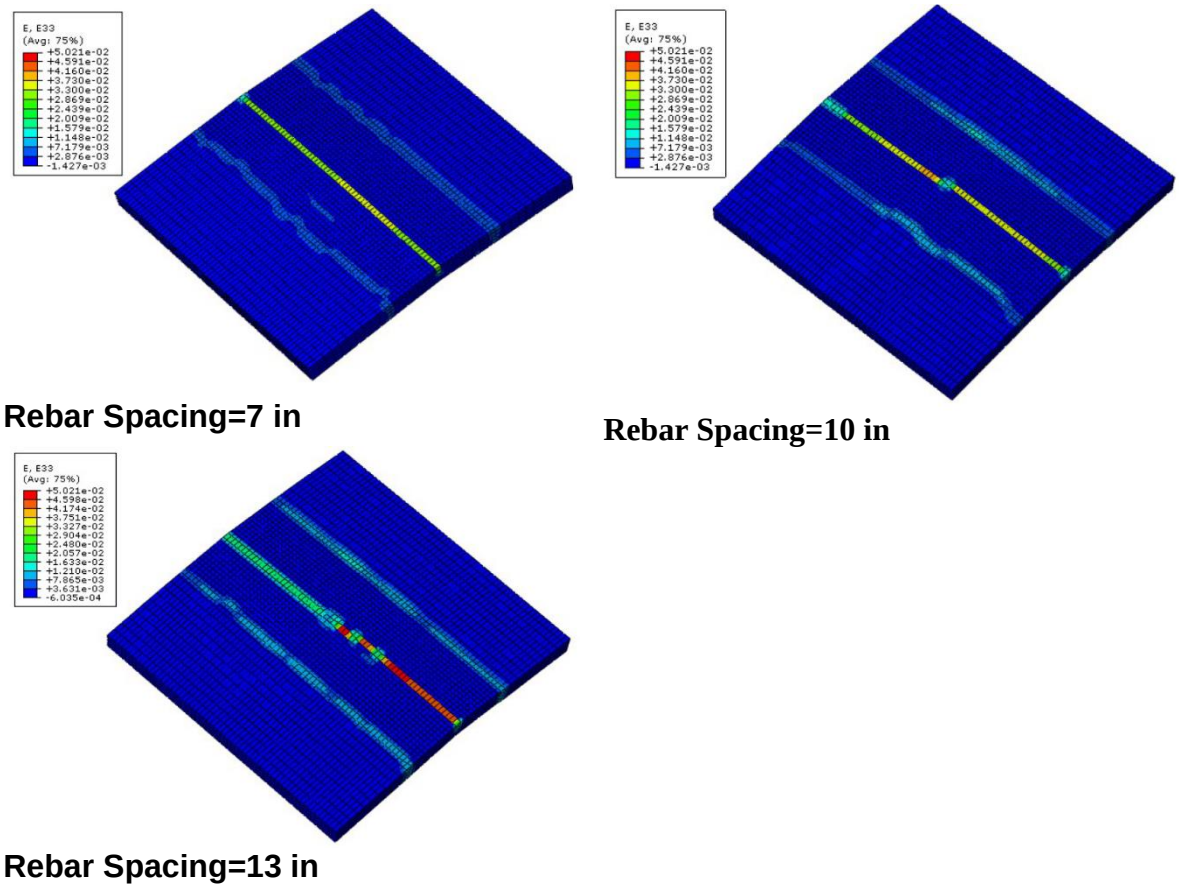

Figure 2.39 *Strain distribution in the link slab*

The strain distribution also shows that as the spacing increases the strains increase and become more pronounced not only on the top of expansion but along the line where debonded region is meeting bonded region. This is understandable as reduced rebar will result in more strains on the surface and thus more cracking as well.

2.8.2 Effect of Rebar Spacing in Transition Zone

The rebar spacing in transition zone becomes an important parameter especially for partial depth link slabs, since this ensures that there is no cracking in the connection between link slab and the concrete and the transfer of stresses to the debonded region in the link slab. The finite element analysis was performed for no additional reinforcement in the transition region, an additional reinforcement of #6 @ 8.9 cm (3.5 in) c/c (as provided in the experiment), and #6 @ 17.8 cm (7in) c/c. The plot of load strain curve (Figure 2.40) shows that the denser reinforcement in transition zone results in higher strain in the rebar. The same trend was observed on the strain observed on the surface of debonded zone, verifying the fact that the denser reinforcement provision in this region will ensure transfer of all stresses to the debonded region.

The strain distribution contours for the varying spacing of the reinforcement in bonded region is shown in the Figure 2.41. It can be observed that the strains are more distributed and extend into bonded zone for no additional reinforcement in the transition zone, while as the density of reinforcement is increased in transition zone the strain becomes more concentrated to the center of link slab and increase in the ultimate values as well, indicating that additional rebars help in transferring the stresses to the central region.

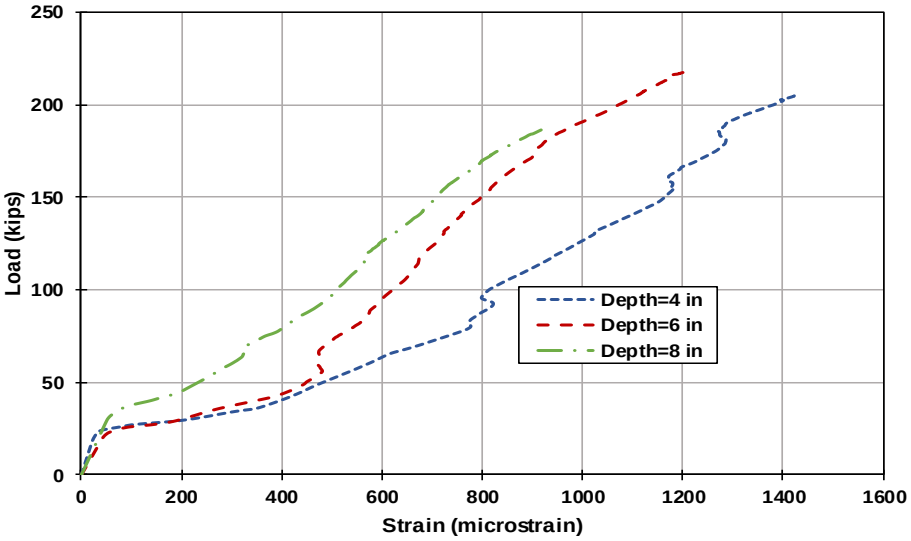

Figure 2.40 *The load strain curves for the strain in rebar of the debonded region*

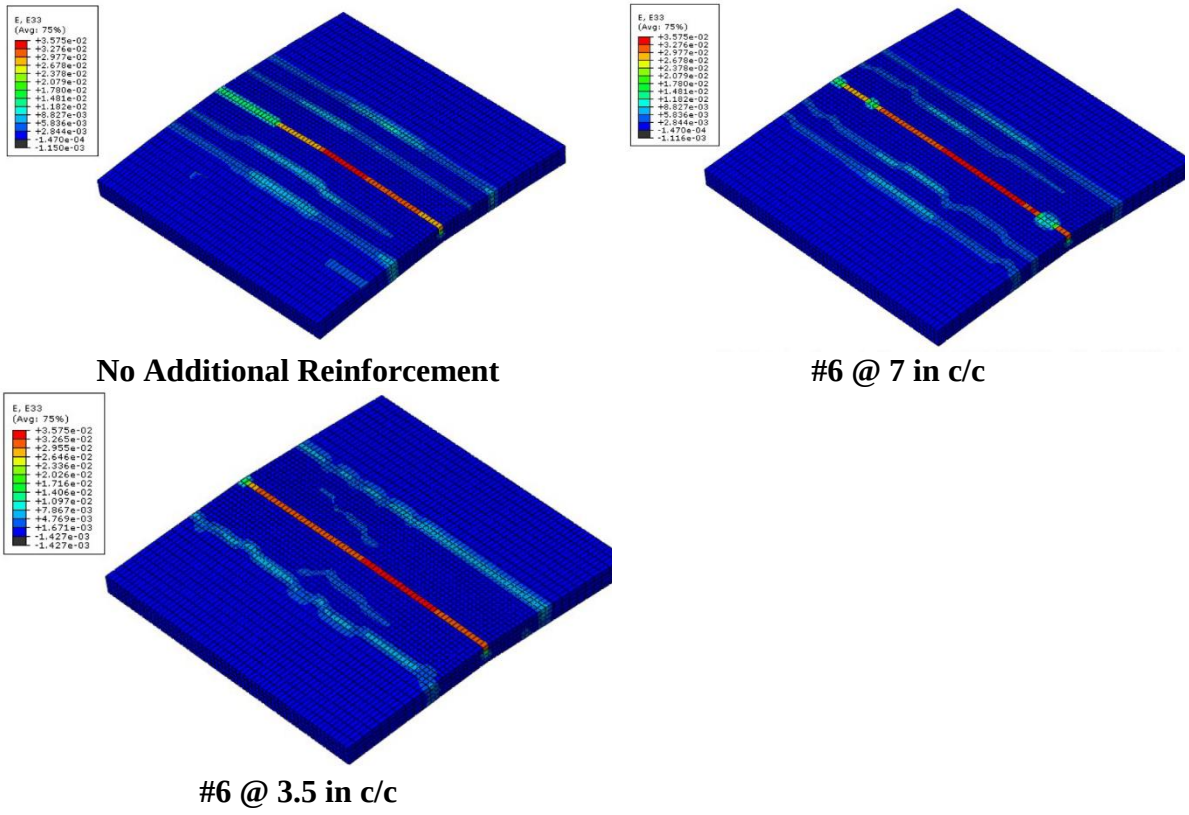

Figure 2.41 *The strain distribution contours for different additional reinforcement in transition zone*

2.8.3 Effect of Depth of Link Slab

The depth of link slab has captured interest of researchers in recent year, mostly because the half and partial depth link slabs can be convenient in rehabilitation projects. The question however has always been how much depth is sufficient since the more depth the more work it involves in taking out the existing portion of the link slab and the more material it needs to be replaced. Bearing in mind the importance of this parameter depth of 10.2 cm (4 in), 15.2 cm (6 in) and 20.3 cm (8 in) is explored through finite element simulations. The load strain curves for the varying depth shows the importance of the variation depth. The strain reduces for the increasing depth of the link slab. The link slab has minimum strain in the rebar for 8 in (Full depth link slab), while it is maximum for 10.2 cm (4 in) or half depth link slab (Figure 2.42).This is understandable since more depth of link slab will provide an increased moment of inertia to resist the negative moment induced in the link slab.

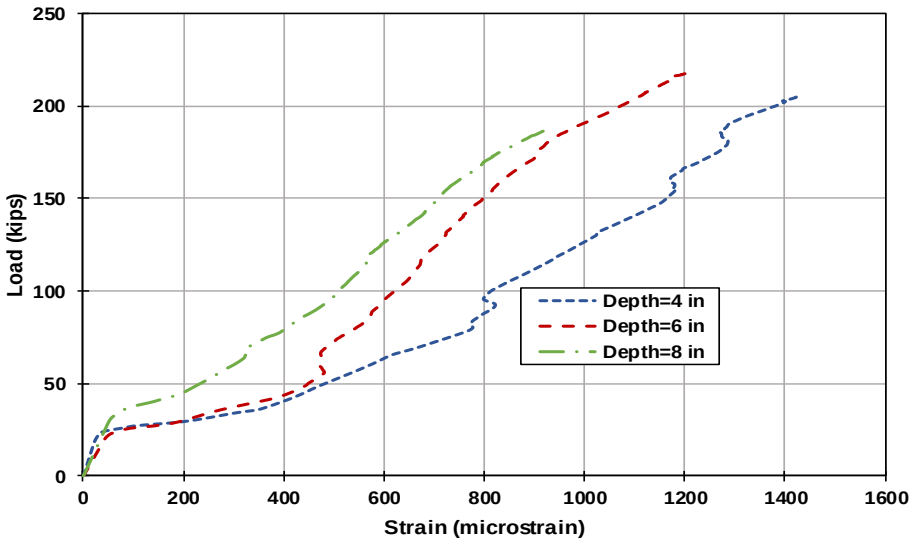

Figure 2.42 The load strain curves for the strain in rebar in debonded region

The strain distribution for the different depth can be seen in Figure 2.43. It can be seen that as depth increases the strain values although decrease but the distribution of strain is more wide spread, whereas for the depth of 4 in strain is concentrated at the center of the link slab.

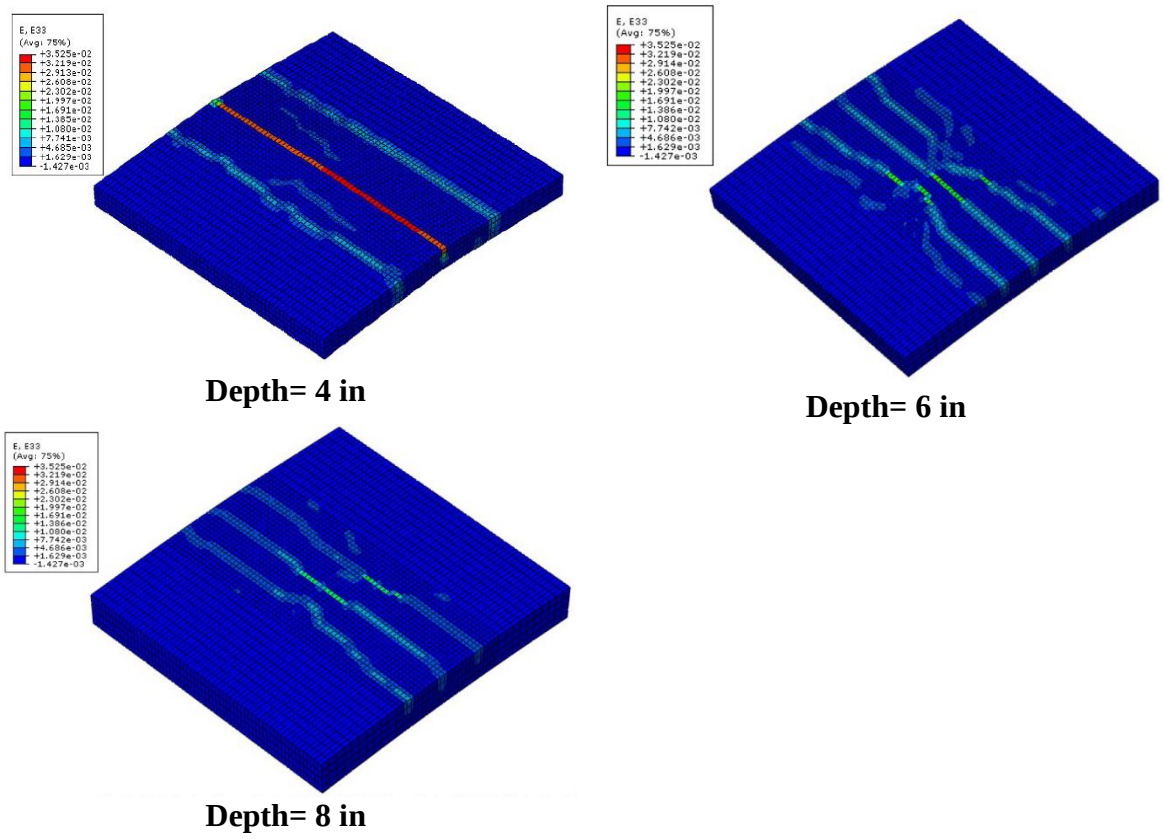

Figure 2.43 *The strain distribution for different depth of link slab*

CHAPTER 3. STRUCTURAL CONFIGURATION OF LINK SLAB FOR ABC APPLICATIONS

3.1 Introduction

Link slabs are a potential solution to the problems associated with the presence of expansion joints in bridge decks. With the addition of link slabs, expansion joints over the piers are eliminated to create a continuous bridge deck system, while maintaining simply supported girder conditions under the deck. In an intact condition, link slabs are able to close the pathway for the ingress of water and deleterious agents into the bridge superstructure. Link slabs are, however, subjected to axial forces and bending moments induced by thermal and service loads, which can potentially cause cracks and other performance issues in bridge structures. Due to direct loading demand on link slabs, they must be made with durable concrete materials designed to withstand high tensile stresses, while maintaining crack resistant properties to protect the bridge girders and piers from exposure to water and deleterious agents. Despite the importance of development of concrete mixture appropriate for link slabs (as explored, for example, by Dopko et al. (2018)), it is critical to obtain a proper understanding of the axial forces and bending moments in a link slab, especially if it is added to an existing bridge that has not been designed with a link slab.

The concept of using continuous bridge decks over simply supported girders gained attention beginning from the 1980s and 1990s (e.g., Zuk, 1981, Hulsey, 1992, Gastal and Zia, 1989, and Caner and Zia, 1998). The initial efforts were then followed by the field application of link slabs (e.g., Li et al., 2005, Kim et al., 2005, Li and Lepech, 2009). The material development targeted specifically for link slabs has been a focus of other studies, primarily to control the crack width (e.g., Li, 2008, Ryes and Robertson, 2011, Larusson, 2013, Hossain

and Anwar, 2014, and Dopko et al., 2018). Among the studies devoted to the structural design and configuration of link slabs, Caner and Zia (1998) designed two link slabs with superstructures of the same length with a deck size of 2 ft wide and 4 in thick. Two different girder types, namely concrete and steel girders were considered. The link slab was of 4 in thickness and 2 ft wide. The link slab was designed based on the mechanics of reinforced concrete materials and the loads induced to the link slabs because of girder end rotations. For this purpose, point load laboratory tests were performed on the two-span, single-girder link slab setups. Based on the outcome of the experimental tests paired with additional numerical simulations, a set of equations were developed for link slab design. The design methodology and steps were based on only the service load and the assumption that the flexural stiffness of the link slab remained minimal compared to that of the adjacent girders. This led to the perception that the flexural contribution of the link slab to the deck and girder system can be neglected and the link slab can be designed using end rotations extracted from the girders that are simply supported.

In a later study, Okeil and El-Safty (2005) showed that a link slab provides partial continuity between the bridge spans and that the girder support conditions have a significant effect on the forces and moments developed in the link slab. The cited study used a set of finite-element (FE) models to explore the forces and moments developed in the link slab based on whether the underlying girder supports were roller or pinned connections. The FE models were of the same dimensions as the test setups developed by Caner and Zia (1998) to make direct comparisons possible. For the two-span system with a total of four supports, two support configurations were investigated. The first configuration consisted of two roller supports at the far ends and two pinned supports at the middle, while this was reversed in the second

configuration to two pinned supports at the far ends and two roller supports at the middle. It was found that the first support configuration led to an upper bound for the loading demand on link slabs due to higher continuity moments. On the other hand, the second support configuration caused an upper bound for the loading demand on girders because of positive moments at the midspan of the girder. Such differences were attributed to the eccentricity of the link slab from the axis of rotation, around which the girder end rotates.

Ulku et al. (2009) explored the demand on link slabs considering the effects of different support conditions, debonded lengths, girder heights, and adjacent span ratios using a single-girder, two-span FE model. Positive and negative temperature gradients, as well as live loads, were applied to the model. The study found that the bending moment can be reduced to more than half after the conversion of support conditions from the pinned to roller condition. It was also reported that there were no difference in axial forces and bending moments for different support conditions under positive and negative temperature gradients. In a separate effort, Hong et al. (2014) performed a detailed FE analysis on a two span full-scale bridge superstructure. The effects of debonding length and support condition were examined on the internal forces and moments generated in the link slab. It was found that the support conditions can significantly influence the loading demand on link slabs.

Despite the fact that the significance of support conditions for the structural design and configuration of link slabs has been highlighted in the available literature, there was no experimental test to obtain an accurate assessment of the strains and stresses developed in the link slab as a function of support conditions. On the other hand, the existing studies were limited to the bridge superstructure, leaving a number of questions unanswered regarding how the addition of link slabs can change the loading demand on the bridge substructure. To address

the identified research gaps from both fundamental and practical perspectives, the current study provides a holistic investigation of link slabs through full-scale experimental tests and supporting numerical simulations. The experimental tests consist of a two-span deck system with three different support configuration under point loads. With a dense instrumentation layout, the strains and deflections are recorded at various locations within the debonded and bonded regions of the link slab, further to the deck and girders. The obtained data are then employed to validate the FE model of the same test setup with the goal of investigating additional link slab configurations beyond those tested in the laboratory. The validated FE model is then extended to evaluate the incorporation of two link slabs into a nine-span bridge with two expansion joints in Iowa. This bridge was selected as a representative of several multi-span bridges that are ideal candidates for the addition of link slabs. Through simulations under temperature gradient and service load effects. The effect of three different support conditions PRRP, RPPR and PPPP, and three debonded length 2.5%, 5% and 7.5% of length on the forces and moments developed in the super and sub structure of the bridge.

Noting that the support under girders are provided by bearing pads, which can change over time from a roller to pinned connection because of wear and tear, the outcome of this study provides the insight necessary to properly use link slabs for repairing existing bridges. This insight goes beyond the assessment of loading demand on bridge superstructures, as it is critical to have a realistic understanding of how loading distribution within the entire bridge super and substructures is influenced after the addition of link slabs to the bridges that were originally designed with expansion joints.

3.2 Experimental Tests with Different Support Configurations

A full-scale two-span experimental test setup, consisting of a bridge deck supported on W21×55 steel girders was built in the laboratory. The concrete deck, which was 160.0 cm (63.0 in) wide and had a thickness of 20.4 cm (8.0 in) and gained a compressive strength of 41.4 MPa (6.0 ksi) after 21 days. To represent the expansion joint, a 5.0 cm (2.0 in) gap was included between the steel girders. A half-depth link slab was constructed using fiber reinforced concrete (FRC). Through a separate investigation at the material level (Dopko et al., 2018), the FRC mixture was designed to offer high ductility in tension with reduced crack widths to ensure that the durability criteria are met. The FRC mixture used for the link slab had a compressive strength of 55.2 MPa (8.0 ksi) after 21 days. The link slab had a depth of 10.2 cm (4.0 in) and a total length of 170 cm (67 in). This length included a debonded length of 68.58 cm (27 in) (2×5% of span length plus 5 cm (2 in)) and a bonded length of 50.8 cm (20 in) as per Larusson (2013) to allow for the transition of concrete deck to link slab. Figure 3.1 shows the overall geometry of the test setup.

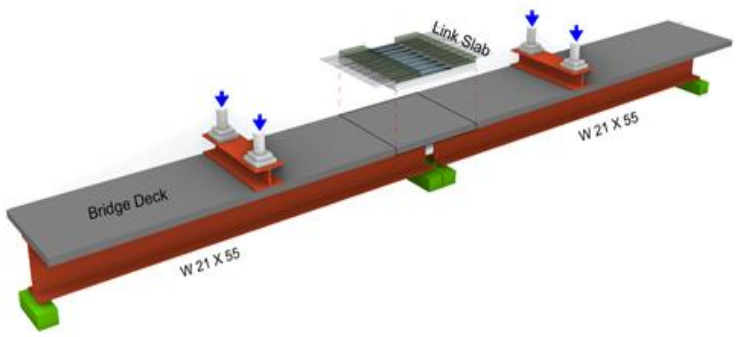

Figure 3.1 *The schematic of test setup in the laboratory.*

The link slab was designed following the procedure provided by Caner and Zia (1998) and modified by Ulku et. al (2009). This included the debonded and bonded regions. The debonded region is intended to release the moment and make the link slab act as pin, while the bonded region is designed to transfer the stresses from the bonded to debonded length, and to avoid any cracking on the face of connection between link slab and concrete deck. The debonded length was considered to be 5% of the span length, as recommended in the literature (e.g., Au and Tharmabala, 2013, Caner and Zia, 1998, Okeil and El-Safty, 2005, Ulku et al., 2009). A dense reinforcement detail is often used in the bonded region (as compared to the debonded region) to allow for transferring stresses from the deck to the debonded region of the link slab. The reinforcement detail included in the link slab consists of #6 longitudinal rebars with 17.8 cm (7.0 in) center-to-center spacing in the unbonded region. This spacing is reduced to half, i.e., 8.9 cm (3.5 in) in the bonded region.

The bridge superstructure was instrumented with a dense array of strain gauges mounted on rebars in different locations to monitor the development of strains as the applied load increases. Among the locations of interest were the reinforcement in the debonded and bonded regions. From preliminary FE simulations, it was observed that strains can become maximum at the center of the debonded length of the link slab. Thus a set of concrete surface strain gauge are mounted on top surface of link slab along the center line of debonded length. Surface strain gauges are provided on top of bonded region to observe the variation of strains between bonded and debonded region. In addition, six linear differential variable transformers (LVDTs) were installed on the steel girders (three on each) to fully monitor the deflection of the girder under different support configurations.

The link slab test setup was subjected to three cycles of loading and unloading for each support configuration. From preliminary FE simulations, the maximum load was decided in such a way that the entire setup remained in the elastic range. Two point loads of up to 88.96 kN (20 kips) were applied to the mid-span of each individual span using two actuators (Figure 3.2). Considering the effect of support configuration on the loading demand that bridge superstructure components, including link slabs, experience, and the current study investigated three support configurations. The configurations of interest consisted of different combinations of roller and pinned supports, which have been labeled as RPPR, PRRP, and PRPR, where R stands for a roller support and P stands for a pinned one. For each support configuration, main structural response measures, such as the deflection at midspan of girder, the strain in the rebar in the top rebar of debonded length, and strain on the top surface of the debonded length of link slab, were recorded for comparison purposes.

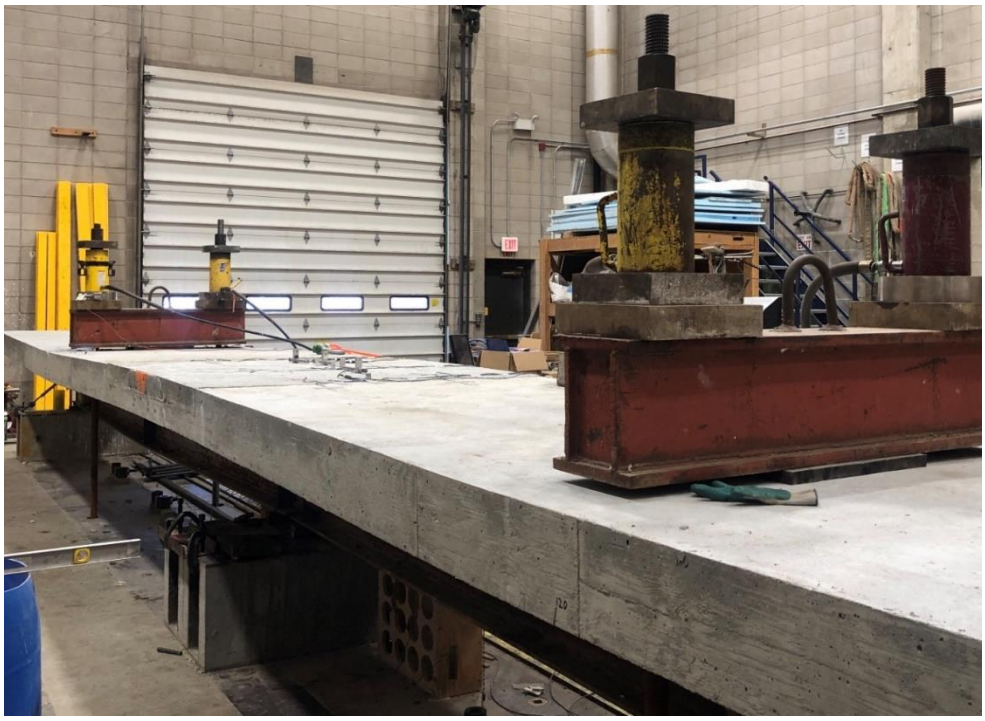

Figure 3.2 *The Laboratory test setup, showing actuators at loading points.*

3.3 Test Results and Observations

The experimental tests began with the PRRP support configuration and continued with PRPR and RPPR support configurations. The strains in the rebar and surface strain gauge was recorded. The strain developed in the top rebar of debonded length and the strain on the surface of the link slab were maximum and varied linearly with the loading. No cracks were observed for the initial two support conditions, however a fine crack on the surface of the link slab extending through the center of the link slab was observed for the RPPR support condition.

For each support configuration, the relation between the load applied to each girder and deflection recorded at the midpoint of the girder was first investigated. As shown in Figure 3.3, the deflection increases linearly by increasing the applied load within the range considered for the current experiments. The load-deflection curves shown in Figure 3.3 indicates that the RPPR support condition behaves as the most rigid one among the support conditions investigated. For PRRP support condition, there is no deflection initial loading of 13.3 kN (3 kips), this can be because the supports were settling. In contrast, the PRPR support configuration provides the least rigidity. This can be further supported with a review of the deflection profile obtained for the entire test setup (Figure 3.4). This profile is generated using the deflection data obtained using LVDTs at three points along the length of the girder in each span. It is noted that with changing the support configuration from RPPR to PRPR, the maximum recorded deflection can increase by up to 25%.

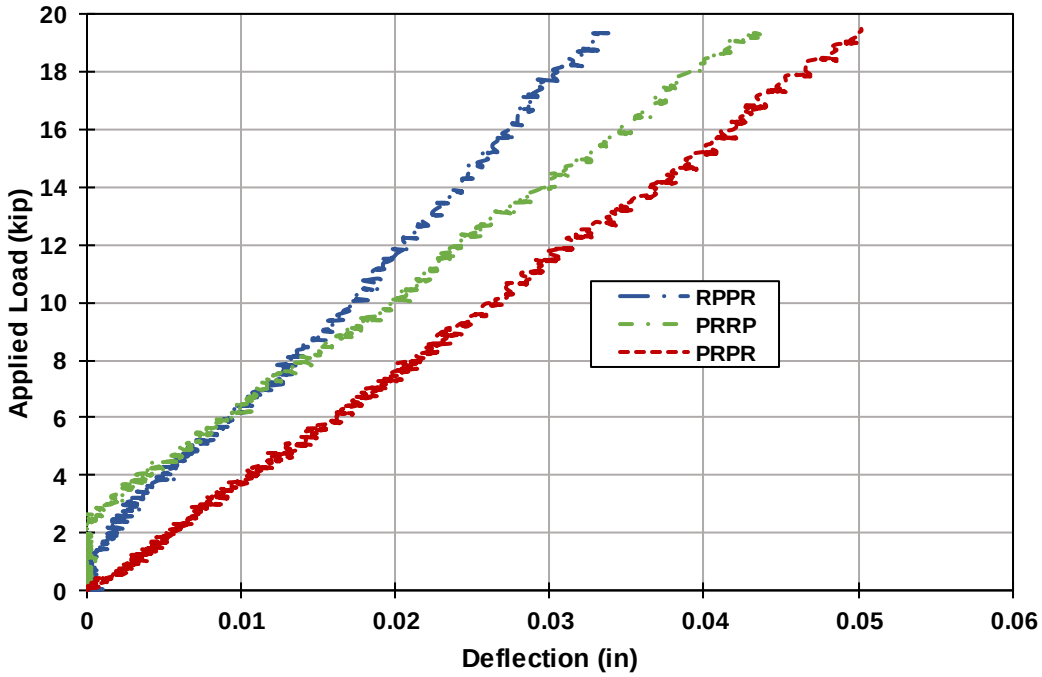

Figure 3.3 *Load-deflection curves for different support configurations.*

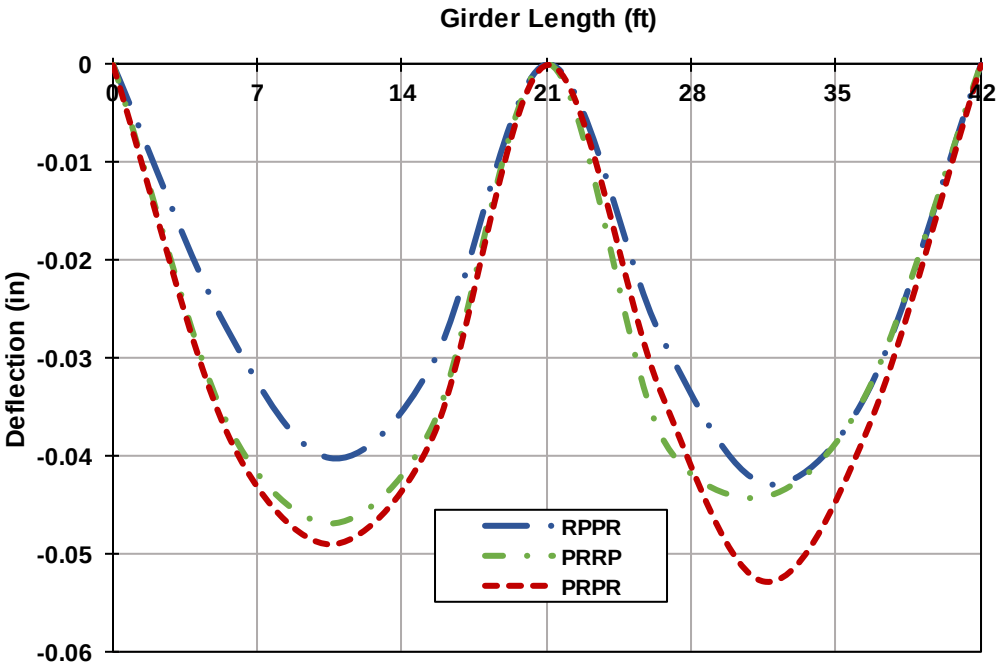

Figure 3.4 *Girder deflection profile under different support configurations.*

Figure 3.5 shows how the strain is developed at the top surface of the debonded region under different support configurations. All the load-strain curves follow a consistent trend and lead to a similar ultimate strain in the range of 747 to 791 microstrains. This indicates that although the support condition does not affect the general trend, but they certainly result in variation in the ultimate strains. The RPPR support condition resulted in maximum strain while the PRRP support condition resulted in minimum strain. The lower strain in PRRP case can be attributed to the ability of roller support condition to move thus releasing any flexural loading induced.

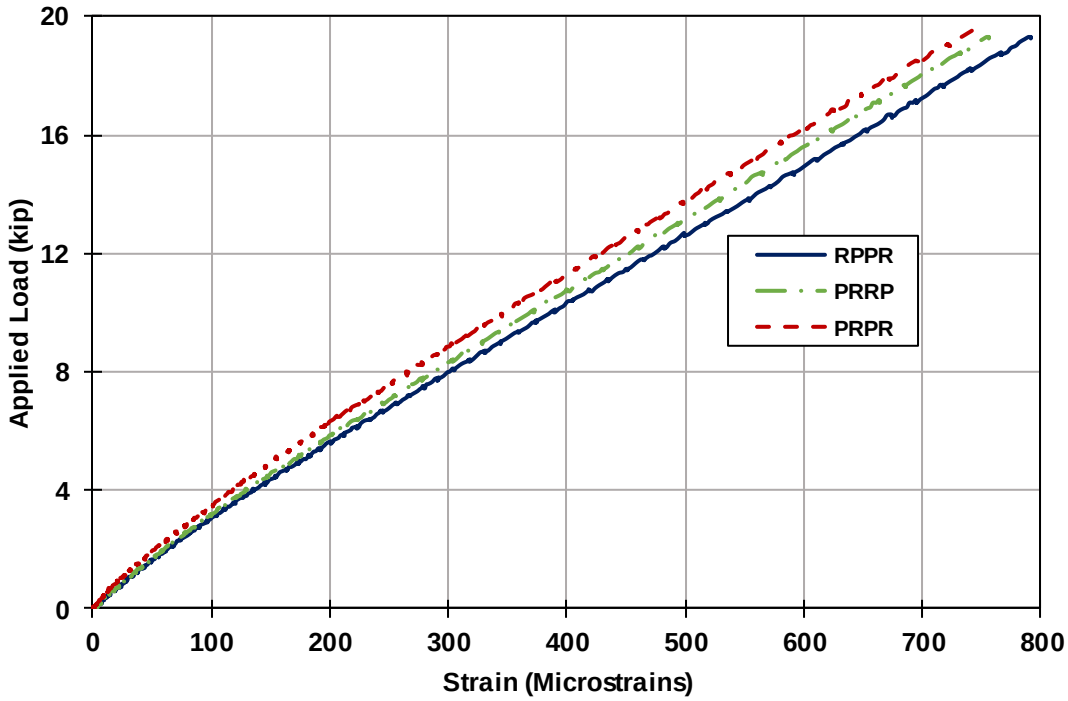

Figure 3.5 *Load Strain curves for surface strain gauges different support conditions*

Figure 3.6 shows the average strain measured at the center of the the top rebars embedded in the debonded region of the link slab. The center of the rebar is located at 5.0 cm (2.0 in) from the top surface of the link slab. The strain measured is the lowest for the PRRP support configuration and the highest for the RPPR support configuration. Noting that the

ultimate strain recorded in the rebars changes from 140 to 228 microstrains, it is critical to design a link slab in such a way that the maximum strain can be accommodated without the formation of cracks, especially under the service loads. The experimental results prove that the variation in support conditions under the link slab not only result in changes in the slope of load-deflection curves, but also effects the demand exerted on the link slab.

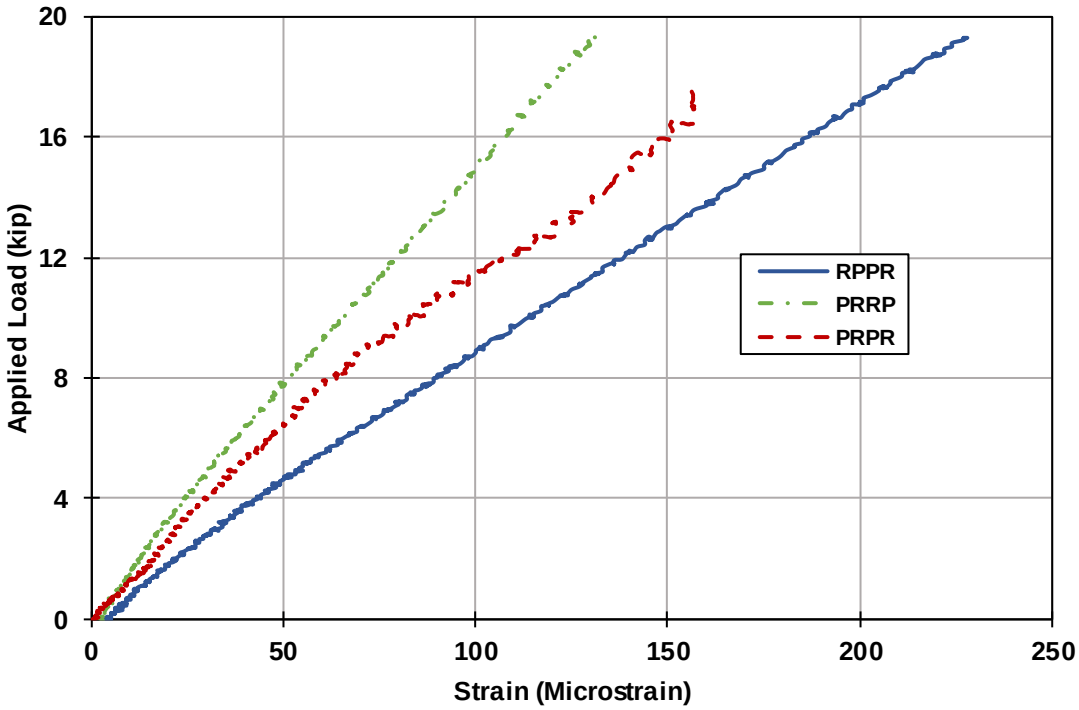

Figure 3.6 *Load Strain Curve for rebar in the debonded region*

3.4 Numerical Investigation of Link Slab Setup

To further investigate the factors that contribute to the structural response of the bridge superstructures with a link slab, the Abaqus software package was used to replicate the link slabs tested in the laboratory (Figure 3.7). The steel girders, concrete deck, and link slab were modeled using an eight-node solid element with hour glass control. The rebars were modeled as two-dimensional truss elements. The bonding between the concrete deck

and steel girder was captured by a tie constraint. This constraint connects the two surfaces together such that there is no relative movement between them. A surface to surface hard contact model in combination with tangential frictionless properties was used for simulating the debonding of the link slab from the concrete deck. This allows the two adjacent surfaces to transfer stresses when they are in contact and to separate when the contact stress drops to zero. The concrete and FRC materials included in the setup were modeled with the concrete damage plasticity model using the properties obtained from the material tests performed along with the full-scale structural tests.

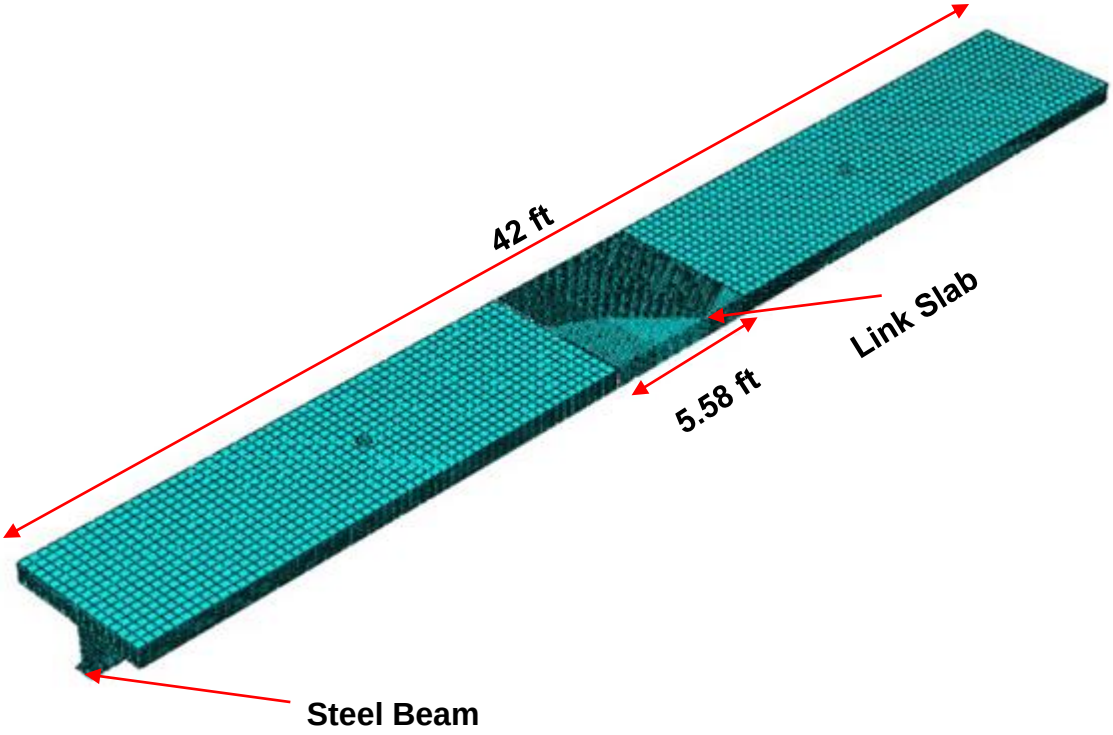

Figure 3.7 *The finite element model for the link slab.*

The developed FE model was first validated using the experimental test results. This was achieved through comparing various structural response measures, such as load-deflection and load-strain relationships. The load deflection curves obtained from the FE simulations and experimental test results are shown in Figure 3.8. It can be seen that the

simulation results closely follow the experimental test data for all the three support configurations. After reviewing the corresponding strain values, it was confirmed that the developed FE model is reliable and can be employed for further investigations.

After validation of FE models, a set of simulations were performed to evaluate the effect of support condition and link slab detail. The models were evaluated for thermal loading in different support conditions. The models were also evaluated for the different debonded length of link slab.

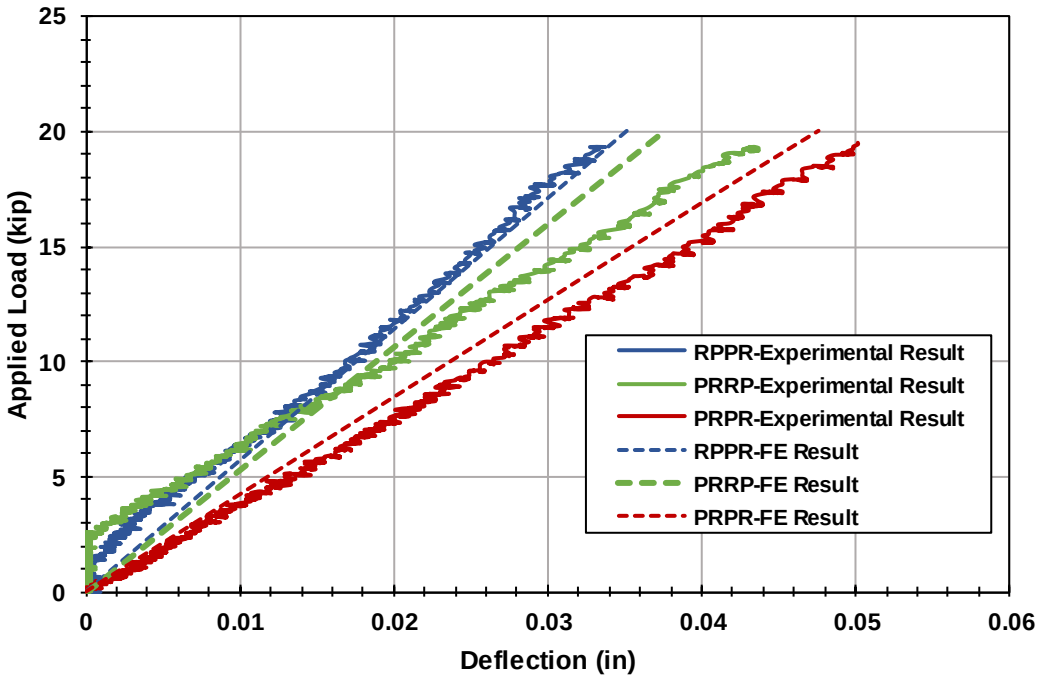

Figure 3.8 *The load deflection curve for different support conditions.*

3.4.1 Effect of Temperature Variation

The experimental results and FE simulation showed that the support condition effect the stresses developed in the link slab. The generated model were used to see the effect of support condition on the thermal induced stresses in the link slab. The thermal stresses were

simulated by subjecting the model to a temperature variation of 50 ºF, which is the temperature variation used by Iowa Department of Transportation for cold climate. The thermal loading along with dead load was simulated considered for different support conditions. The PRRP support condition resulted in the least strain in the rebar with (349 microstrain), while the PRPR condition resulted in the maximum strain (504 microstrain) in the rebar in debonded region of the link slab. The strain distribution followed the same trend for the surface strains with PRRP being the lower bound and RPPR the upper bound. The contours for strain variations can be seen in the Figure 3.9.

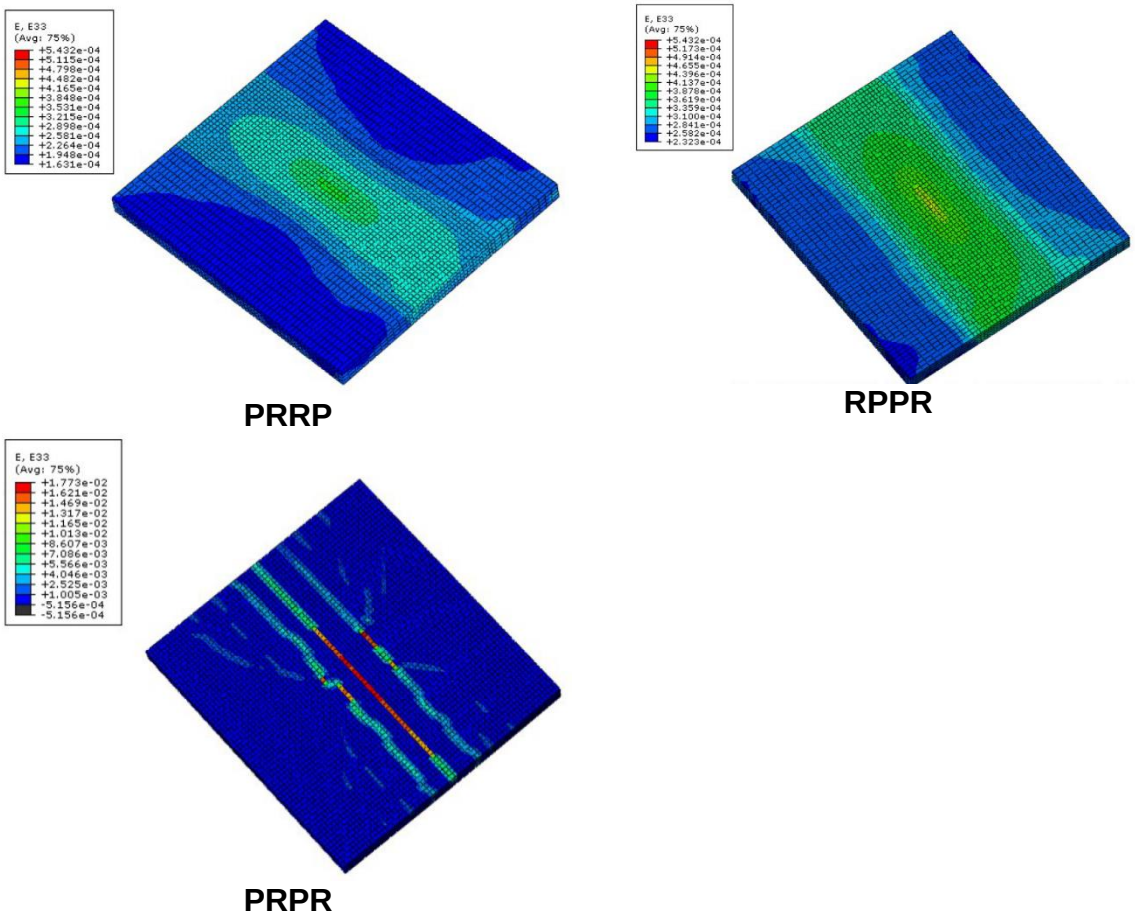

Figure 3.9 *Effect of support condition under gravity and thermal loading*

The increased strains in PRPR condition can be explained by the fact that the movement of girder is restrained on one side and the expansion is again restrained by the second pin under

the link slab, the expansion in between these two pin will be experienced by the link slab and the pin under link slab will act as a point around which the link slab will rotate, resulting in an increased strain on top of link slab. This does not happen in the other two support configuration, for instance in the PRRP case the rollers will move under the link slab thus releasing the point around which the link slab could rotate, and in turn releasing the flexural load, while in RPPR case the forces will be released by the outward movement of the rollers at the outer ends of girders.

3.4.2 Effect of Debonded Length

The debonded length of the link slab has been of interest because an increased debonded length results in an increased cost, as it involves more work of concrete removal and replacement. The debonded length of 2.5%, 5% and 7.5% are evaluated. The midspan deflection recorded for the 2.5% debonded length is minimum (1.54 cm (0.61 in)) while that for 7.5% debonded length is maximum (2.39 cm (0.92 in)), this highlights the fact that the increase in debonded length reduces the rigidity in the link slab. The strains however were maximum for the debonded length of 5%, and minimum for 2.5% debonded length, the strain contours are presented in the Figure 3.10. One common observation from the strain distribution contours is that irrespective of the debonded length the strain is maximum along the center of debonded length right on top of the expansion joint and this maximum strain is then followed by the strain along the line where the debonded region meets the bonded region.

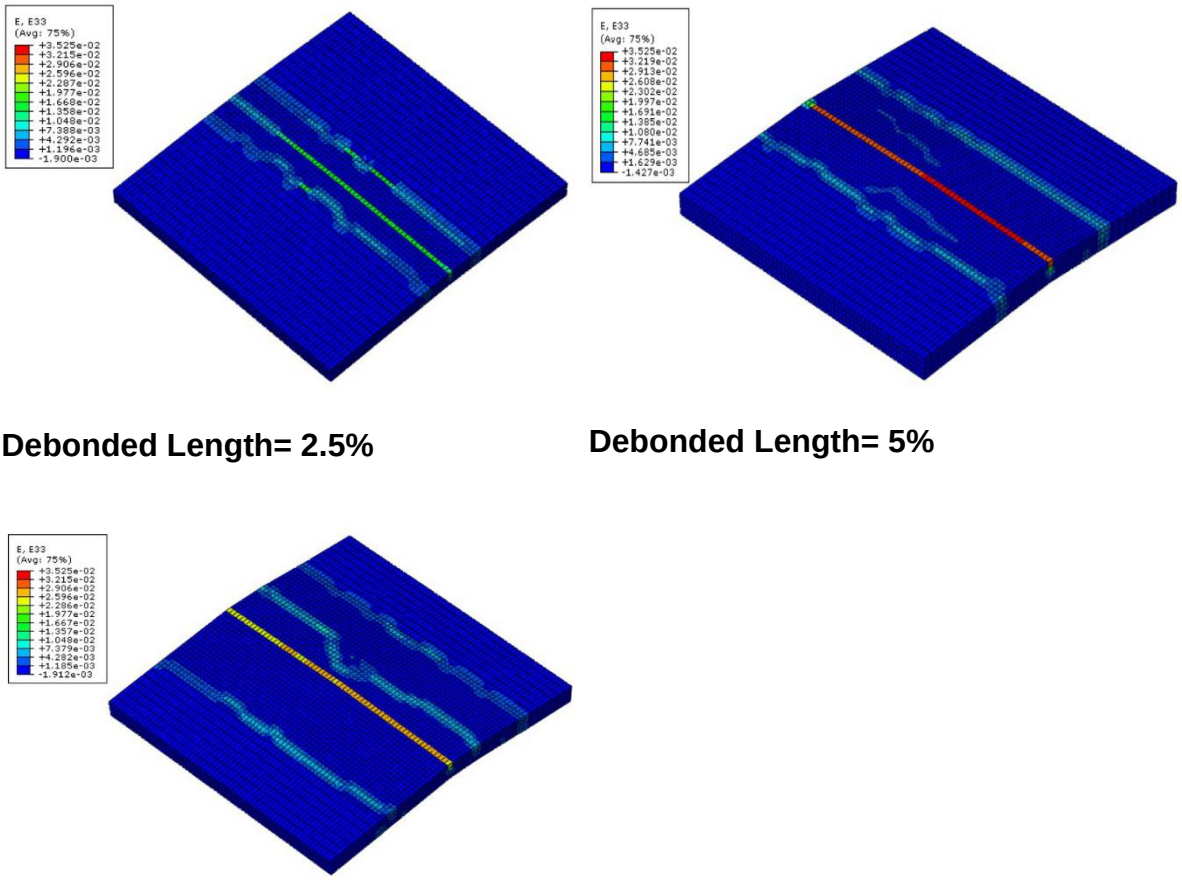

Figure 3.10 *Strain distribution for varying debonded length of link slab*

3.5 Load Distribution in Bridge Structure

To extend the scope of investigations to the entire bridge structure, and especially investigate how the loading demand on the bridge substructure changes after the addition of link slabs, a nine-span bridge located on Iowa Highway 101 over the Cedar River in Vinton, Iowa is considered as a candidate to replace its expansion joints with link slabs. The total length of the bridge is 247.5 m (811.9 ft). The bridge was originally designed with two expansion joints, which were located over the third and sixth piers. Continuous supports were provided over the remaining six piers, which can be assumed to behave similar to a pinned connection.

Of the nine spans, the seven interior spans are 29.4 m (96.5 ft) long and the two exterior spans are both 20 m (65'-9") long (Figure 3.11). The bridge ends are not tied to the abutment, and thus, assumed free to move. The letting date for the bridge was 1979, making the bridge 40 years of age in 2019.

The bridge has been constructed with pre-tensioned, pre-stressed concrete girders and supported by deep piles at the piers and abutments. The design stresses for the bridge material, which are in accordance with the AASHTO Standard Specifications for Highway Bridges, Series of 1977, can be summarized as follows: reinforcing steel of f_s = 138 MPa (20,000 psi), (Section 1.5.26B), concrete (girders) of f_c = 34.5 MPa (5,000 psi), concrete (other bridge components) of f_c = 24 MPa (3,500 psi), (Section 1.6.6B), and prestressing steel of f_s = 1860 MPa (270,000 psi), (Section 1.6.6A). When the bridge was originally designed, the bearing pads that support girders at the expansion joints were modeled and expected to behave similar to a roller support. As the bearing pads age, however, it is expected that their behavior changes. The older the pads get, the more they start to behave like a pinned support rather than a roller support. Taking this and the age of the bridge into consideration, it is found critical to investigate the effect of support configuration on the load distribution in the bridge super and substructure. The ABAQUS software package was used for the modeling and simulation of the entire bridge structure. A number of assumptions and idealizations were made to construct the FE model that can represent the bridge as accurately as possible. The most effective three-dimensional FE model of the superstructure utilized shell elements for the slab deck with eccentrically stiffened beam elements for the girders (Figure 3.12). To capture the accurate stiffness of the girders, their exact cross-sectional geometry has been assigned to them.

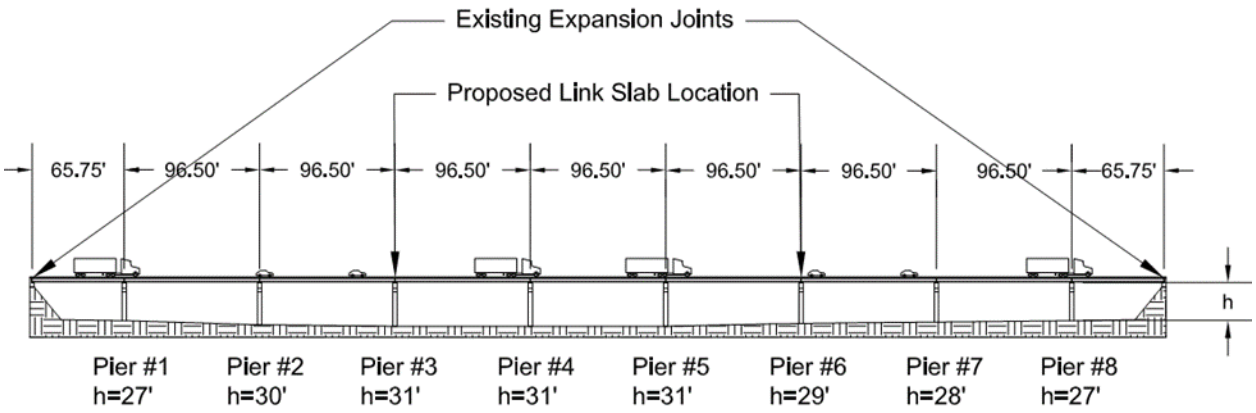

Figure 3.11 *Schematic layout of the bridge structure under consideration.*

The ABAQUS software package has the capability to apply an offset distance to the shell and beam elements from their node locations. Thus, the shell and beam elements have been assigned to the mid-surface of the thickness of the slab deck and the neutral axis of the cross-sectional area of the girders, respectively. This makes it possible to accurately capture the T-beam moment of inertia. The full composite action between the concrete slab deck and prestressed concrete girders is modeled by the node-to-surface link elements with tie constraints. Care is taken to tie the portion of the deck slab as wide as the top flange width of each girder. This helps the slab decks and the girders tied to them to act monotonically under external loads as is the case for the actual bridge.

The link slabs were modeled using the FRC material properties obtained from the experimental tests. The connectivity between the link slab and slab deck, on both sides, was defined using the surface-to-surface tie constraints. Considering the geometry of the bridge piers, they are modeled using shell elements. The connectivity between the piers and the girders were modeled by rigid link elements through multi-point constraints. Such rigid links enforce the kinematic relationships between the degrees of freedom at each node shared with two different types of finite elements, i.e., shell elements of the piers and beam elements of the

girders. This will effectively eliminate the perturbation of stresses and strains at the interface boundary of the piers and girders. The boundary conditions at the base of the piers were modeled using ideal fixed connections. To investigate the effect of support configurations on the structural response of the bridge super and substructure, three combinations of PPPP, PRRP, and RPPR were simulated. The effect of the link slab's debonded length was also explored by considering a range of debonded length, i.e., 2.5%, 5.0%, and 7.5% of the span length. These configurations have been evaluated for the dead load and a temperature gradient of 50 ºF, which is used by Iowa Department of Transportation for cold weather conditions.

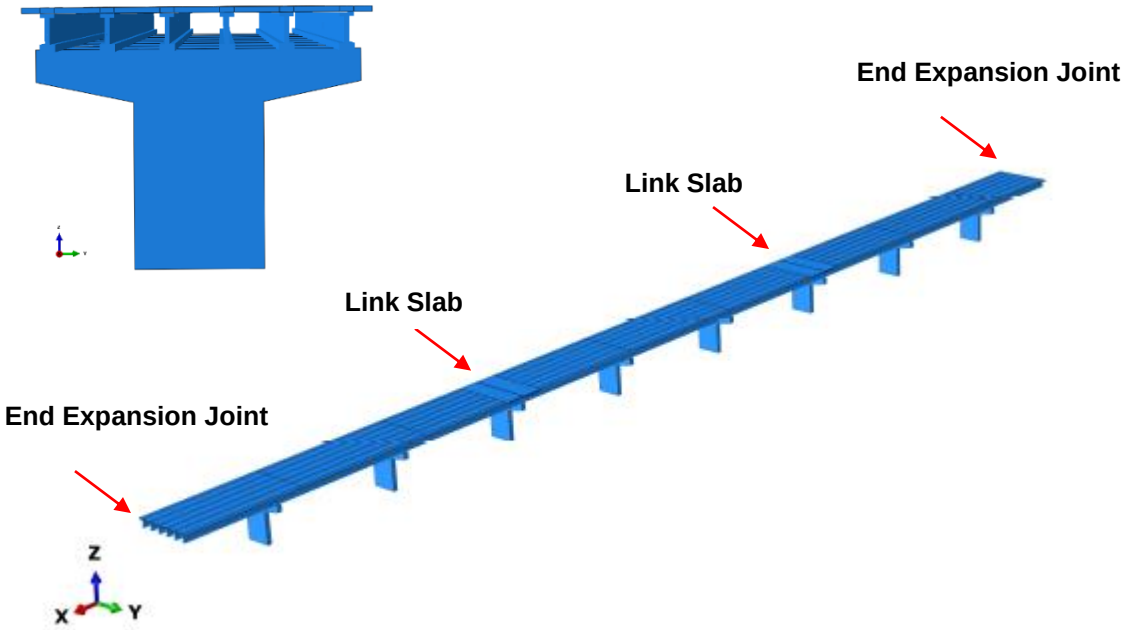

Figure 3.12 *Link slab locations and end expansion joints locations.*

3.6 Simulation Results and Findings

Upon completing the FE simulations, a range of structural response measures, such as axial forces and bending moments in the piers, link slabs, and bridge decks, were obtained. A detailed comparison was then made to understand the effect of support configurations with the

debonded length fixed at 5% of the span length. In the next stage, noting that the RPPR support configuration causes the highest demand, the effect of debonded length, i.e., 2.5%, 5%, and 7.5%, was explored when the support configuration was fixed at RPPR.

The bending moments and axial forces generated in the link slab and slab deck of the bridge were obtained for different support configurations and debonded lengths. The effect of different support configurations on the bending moment developed along the length of the link slab is shown in Figure 3.13. It can be seen that the RPPR support configuration results in the highest bending moment at the debonded length, while the PRRP support configuration causes the highest bending moment at the two ends. This is expected since the RPPR support configuration provides a pinned connection under the link slab at pier 3 and pier 6, about which the link slab can rotate, while in the PRRP configuration, the support can move under the bending moment, thus releasing the moments at the support, which eliminates the rotation of the link slab.

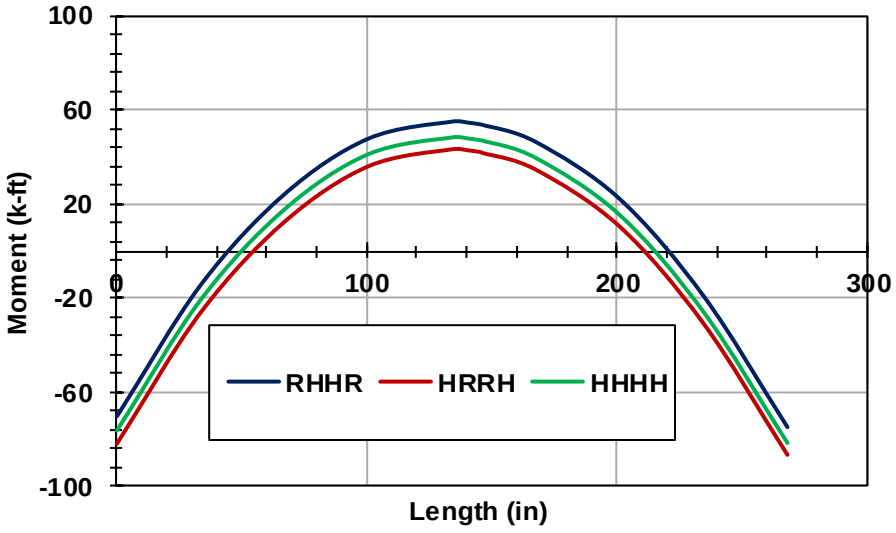

Figure 3.13 *Bending moment in the link slab for different support conditions.*

The axial forces developed in the link slabs are also affected by variation in the support configuration. The PRRP support configuration results in the highest axial force of 14323 kN (3220 kip), while the RPPR support configuration causes the lowest axial force of 4942 kN (1111 kip).This is due to the fact that in the PRRP support configuration the expansion of the bridge is experienced by the link slab, as the pinned connection at the ends restrict the outward deflection of the bridge deck, while in the RPPR support configuration, the supports allow for outward deflection, thus freeing the link slab from additional axial stresses.

The findings from the performed simulations show that the two support configurations of RPPR and PRRP have opposite trends regarding the bending moment and axial force developed in the link slabs. This highlights the fact that depending on the support configuration under the link slab, either axial force or bending moment can be controlling. The important point to be noted is that it will be best to provide support configurations that can minimize the flexural loading in the link slab, as the bridges are subjected to live load (which is not considered in this study) along with dead load and thermal load, the live load can result in additional moments, while it will have negligible contribution to the axial forces.

The effect of support configuration on the bending moment and axial force in the mid-span section of the bridge deck has been summarized in Table 3.1. The bridge without link slab experienced maximum moment at midspan for PRRP support condition, while minimum for PPPP support condition. The axial force for support condition without link slab was highest for PPPP support conditions and lowest for RPPR support configuration. For the bridge with link slab it can be seen that the PPPP support configuration resulted in the maximum axial force and bending moment in the mid-span section, while the RPPR support configuration resulted in minimum bending moment and axial force in the same section. The high values of

what obtained for the PRRP and PPPP support configurations can be attributed to the end restraints. The RPPR support configuration has rollers at the ends, which can freely move, thus reduce the moment and axial force in the rest of the deck.

Table 3.1 *Response of super structure under different support conditions*

	Midspan Response						
	Without Link Slab			With Link Slab			
	Moment (k-ft)	**Axial Force (kip)**	**Deflection (in)**	**Moment (k-ft)**	**Axial Force (kip)**	**Deflection (in)**	**Link Slab Deflection (in)**
RPPR	1392.5	326.8	0.075	1214	134	0.0090	-0.641
PRRP	1750.8	41.5	0.086	3176	3341	0.0630	-0.632
PPPP	1298.3	401.5	0.075	3225	3380	0.0570	-0.636

The deflection of the top of the link slab and the deck mid-span can also be found in Table 3.1. The mid span deflection for PPPP and RPPR support condition is same for the bridge without link slab and the deflection is higher for PRRP case. Since in the bridge without link slab, the middle section will be acting independent of the end supports the deflection comes out to be same for the RPPR and PPPP support conditions. The deflection values for the bridge without link slab are higher than the bridge with link slab because the link slab will add additional rigidity to the structure thus reducing the deflections. The mid-span deck deflection for the RPPR support configuration is minimum, while the movement of the link slab is maximum for the same support configuration. This is because the two pinned connections will provide an increased constraint as compared to the PRRP support configuration. The deflection profile for all the support conditions evaluated with and without link slabs are shown in Figure 3.14. The effect of debonded length on the axial forces developed in the super structure is also investigated. The axial force decreases with increasing the debonded length as reflected in Table 3.2. On the other hand, the bending moments obtained for the varying debonded lengths

show that the bending moment in the link slab increases with the increase in the debonded length. This is an important observation as increase in the debonded length should release the demand on the link slab. The increase in the bending moment for increasing the debonded length from 2.5% to 7.5% resulted in bending moments that were up to 1.5 times of the moments generated with a 2.5% debonded length.

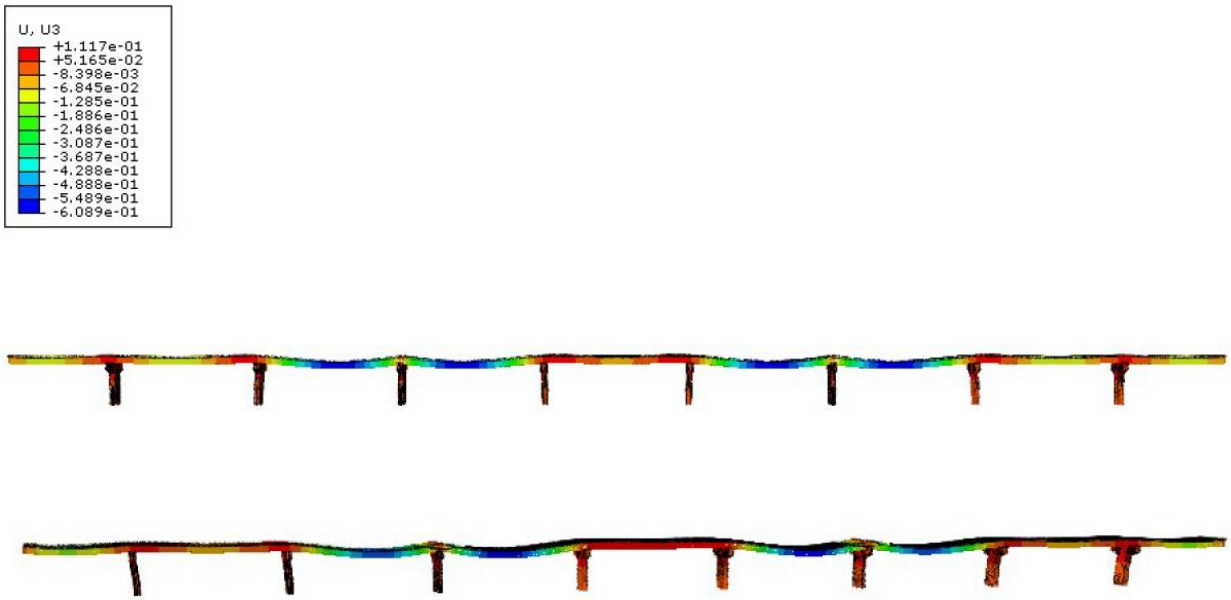

(a)

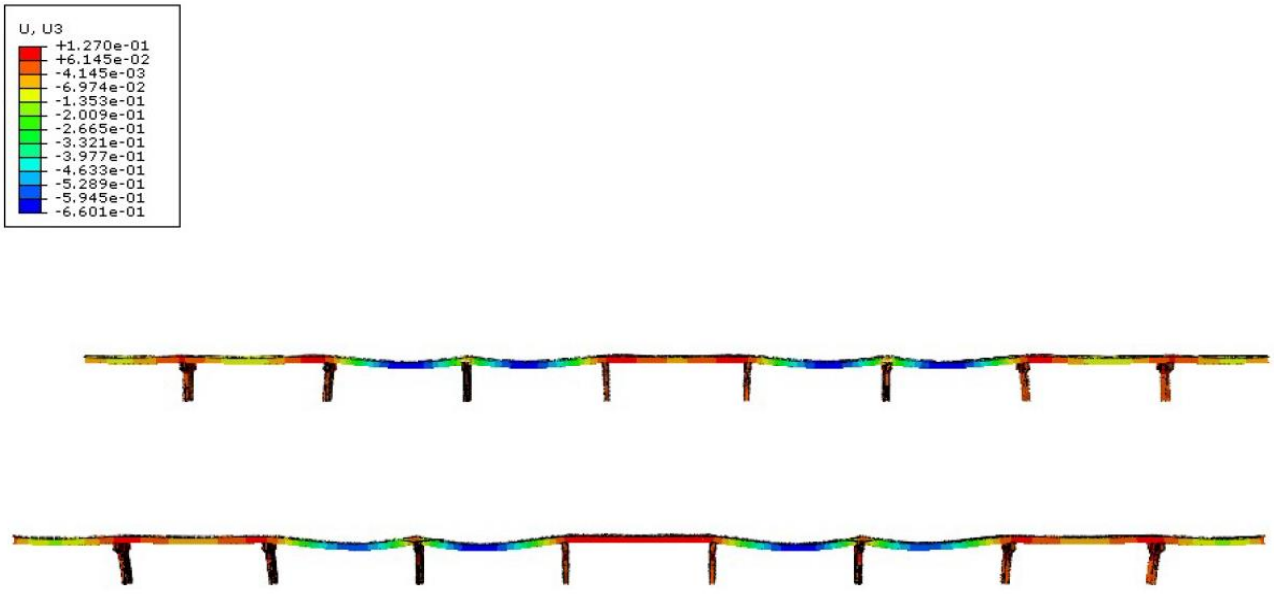

(b)

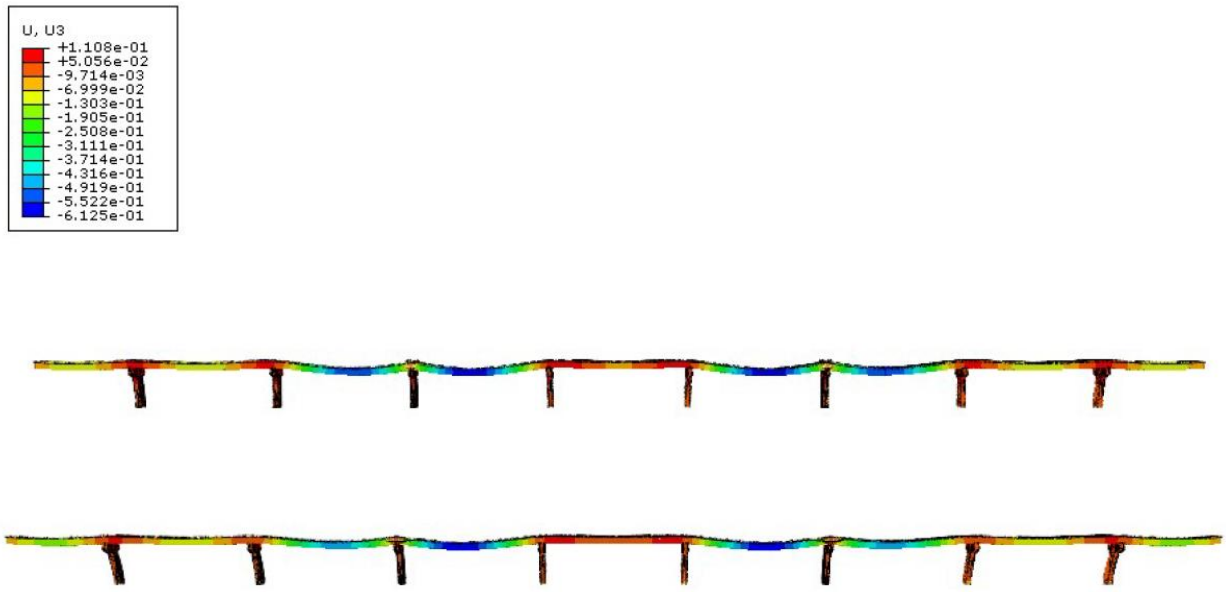

(c)

Figure 3.14 *(a) PPPP without LS and PPPP with LS (b) PRRP without LS (top) and PRRP with LS (bottom) (c) RPPR without LS (top) and RPPR with LS (bottom)*

Table 3.2 *The axial force and moment at mid-span of the deck.*

	Link Slab		**Mid-span of the Deck**	
Debonded Length	**Axial Force (kips)**	**Bending Moment (k-ft)**	**Axial Force (kips)**	**Bending Moment (k-ft)**
2.5%	1112	11	2968	131.0
5.0%	1111	54.5	1214	134.3
7.5%	1111	54.8	1138	185.0

The reaction forces and moments for different support condition with and without link slab were obtained. A comparison of the results for reaction forces show that the addition of link slab resulted in an increase of 4.5 % in reaction force on the piers adjacent to the pier with link slab on it. The variation in all other piers because of the addition of link slab was negligible. This increase in reaction force can be attributed to the additional self-weight of link slab. The reaction moments in the piers was obtained for the structure with and without link

slab. This is important considering the addition of link slab in an existing structure will change the demand on different components of the structure. The addition of link slab resulted in significant increase in the reaction moment. Figure 3.15 shows the reaction moments developed in the piers with and without link slab, where the PPPPwLS refers to PPPP support configuration with link slab, and PPPPwoLS refers to PPPP support configuration without link slab. For the support configuration with highest moments in pier (RPPR) the reaction on end pier increased almost three times of the original demand, while for PRRP case the demand increased by almost 6 times of original demand on the pier for same support configuration without link slab. The reaction moments were minimum for PRRP case and maximum for RPPR support configuration for bridge with and without link slab for all the piers towards the end from the link slab (P1, P2, P3, P6, P7 and P8). For the piers in located in between the two link slab (P4 and P5), the reaction moments remained unchanged for different support configuration without link slab, however when link slab was added the reaction moment was highest for RPPR and lowest for PRRP support condition. This is expected as the slab is expanding under temperature loading and the pinned connection in RPPR support configuration, between the girder and pier transfers all the generated moments to the piers. The other two support conditions, i.e., PRRP and PPPP, cause almost the same reaction moments on all the piers, except Piers 3 and 6. Piers 3 and 6 are the piers, above which link slabs are located. The reaction moments on these two piers are the lowest for the PRRP support configuration and the highest for the RPPR support configuration. This is due to the fact that the roller connection in the PRRP configuration allows for the lateral movement of the bridge superstructure without moving the pier, and thus, releasing the on top of the pier, while in the RPPR configuration, the pinned connection provides additional lateral force on top of the

column, thus, increasing the reaction moments. The reaction forces in the piers remained unchanged for different support conditions.

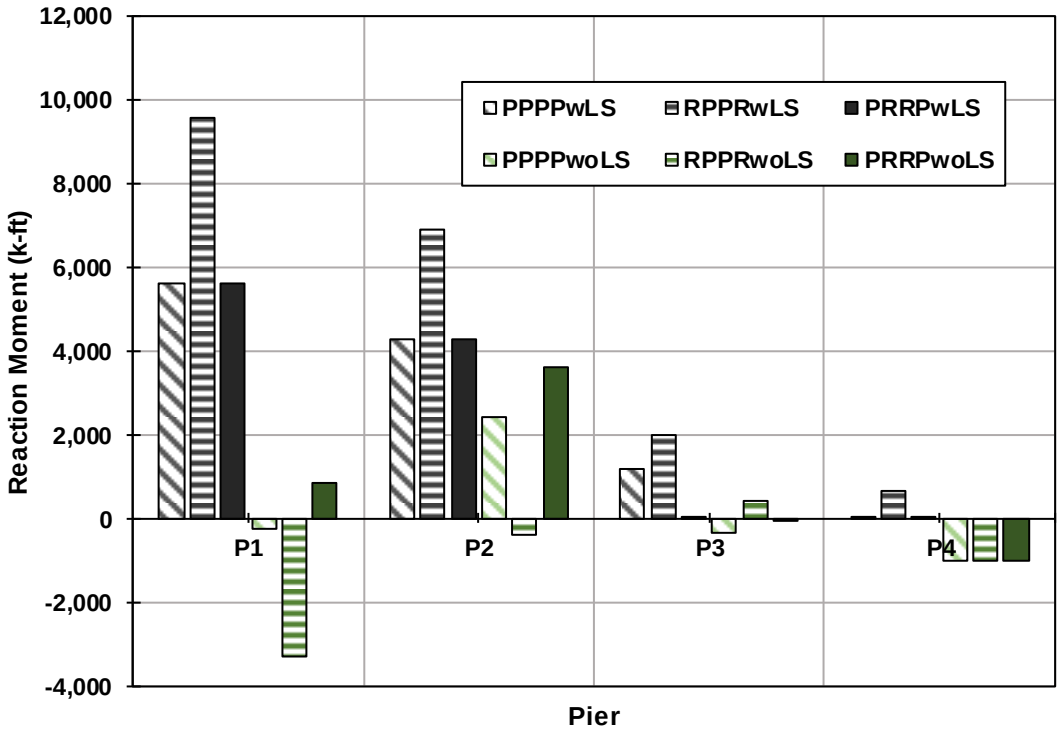

Figure 3.15 *Reaction moments on piers for different support conditions.*

The reaction moments for varying debonded lengths for the RPPR support configuration are shown in Figure 3.16. It can be seen that the change in debonded length does not change the reaction moment at the pier base. This is due to the fact that the change in debonded length is not changing the overall length of the structure or the boundary condition of the piers. The debonded length had no effect on the reaction forces in the pier.

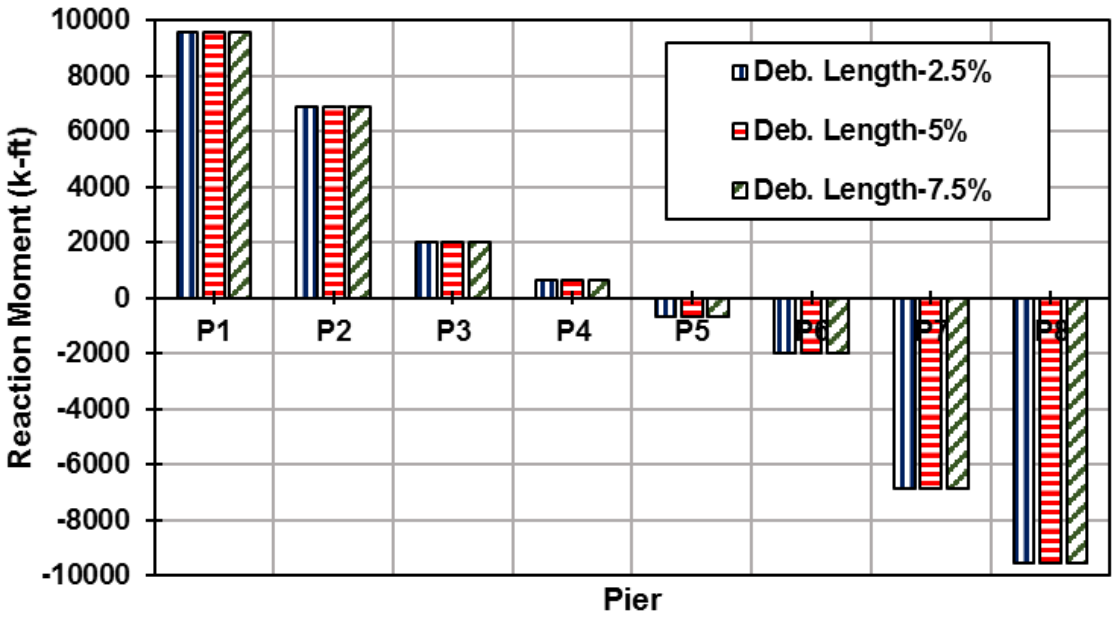

Figure 3.16 *Reaction moments on the pier for varying debonded length of link slab.*

CHAPTER 4. ASSESSMENT OF TRANSPORT PROPERTIES, VOLUME STABILITY, AND FROST RESISTANCE OF NON-PROPRIETARY ULTRA-HIGH PERFORMANCE CONCRETE

4.1 Introduction

Disruption in the functionality of concrete structures as a result of deterioration has become a growing concern for those involved in the construction, maintenance, and management of civil infrastructures. Thus, a mounting demand has been placed to enhance the performance of concrete against the penetration of destructive agents with the ultimate goal of increasing the expected service life. This has led to the development of ultra-high performance concrete (UHPC), which offers superior mechanical, permeability, and durability properties compared to conventional concrete. The exceptional properties of UHPC are obtained through a set of special requirements, including: (1) low water-to-binder ratio, (2) gradation of solid particles optimized for high particle packing density, (3) high quality cement and aggregates, (4) abundant use of cement and supplementary cementitious materials, (5) high particle dispersion during the mixing process, and (6) incorporation of fibers. The aggregates used for UHPC are considerably finer than the aggregates commonly used in conventional concrete. This, in turn, improves the packing density of UHPC, while demanding careful aggregate selection and gradation.

The main ingredients of UHPC are often produced, packaged, and distributed as proprietary mixtures with a unit price significantly higher than conventional concrete. Given the fact that this proprietary aspect has made UHPC cost prohibitive in many civil infrastructure projects, there have been research efforts to develop low-cost, non-proprietary UHPC mixtures by optimizing the cement content, replacing a portion of cement with other less expensive cementitious materials, and exploiting less expensive granular materials.

Among the past studies, Ghafari et al. (2015) provided an analytical model for developing a UHPC mixture that delivers the desired strength with minimum cement content using a statistical mixture design approach. Yu et al. (2014), Shi et al. (2015), Soliman and Tagnit-Hamou (2017 a,b) considered different filler materials, such as limestone and quartz powder, supplementary cementitious materials, such as fly ash and slag, and less expensive granular materials, such as fine glass powder, to reduce the total cost, while maintaining the strength of UHPC. Wille et al. (2011 and 2015) developed a non-proprietary UHPC mixture using the materials commercially available in the United States with the primary objective of optimizing the mixture proportion to achieve a high strength.

The studies on the durability aspects of non-proprietary UHPC mixtures are, however, limited. Among the existing studies, El-Tawil et al. (2016) investigated non-proprietary UHPC mixtures made with different types of cement, different silica fume contents, and various volume percentages of steel fiber. The UHPC mixtures showed no significant variation in relative dynamic modulus, the mass loss was less than 3% for all the tested specimens, and the passing charge was negligible in the rapid chloride penetration test. Berry et al. (2017) developed a non-proprietary UHPC mixture, for which the drying shrinkage strain was recorded to be 130 microstrains after 120 days; the passing charge was very low; a negligible mass loss was observed after 300 cycles of freeze and thaw; and no scaling was reported when the specimens were subjected to deicing chemicals for 50 cycles. In a separate effort, Khayat and Valipour (2018) developed a non-proprietary UHPC mixture and tested it for resistivity, shrinkage, and frost resistance. The autogenous and drying shrinkage for the non-proprietary mixture that contained only cement as binder were high. This issue was addressed by replacing 50% of cement with ground granulated blast furnace slag. The electrical resistivity measured

for the mixtures was in the range of 30 to 45 kΩ-cm. The durability factor reduced only 0.03% after 300 cycles of freeze and thaw, highlighting the superior frost resistance of the developed mixture.

Despite the contribution of former studies to shed light on some of the durability aspects of non-proprietary UHPC mixtures, the transport properties and volume stability of such mixtures had not been investigated with proper methods and details. In particular, the existing studies were only focused on rapid chloride penetration or resistivity tests, which cannot be sufficient considering the drawbacks identified for these tests. On the other hand, shrinkage, especially autogenous shrinkage, which is known to be a critical issue for UHPC mixtures (Mechtcherine et al., 2009, Koh et al., 2011, Yoo et al., 2014, Bao et al., 2015 and 2017, Yoo and Banthia, 2016, Meng and Khayat, 2017), had not been explored in depth or rarely considered for non-proprietary UHPC. To address the current research gaps, the objective of this study is to develop non-proprietary UHPC mixtures with locally available materials and then assess their performance under the penetration of destructive agents, moisture variation, and freeze and thaw cycles. For this purpose, a set of six non-proprietary UHPC mixtures are designed by using ordinary Portland cement, regular sand, widely available masonry sand, silica fume, and steel fiber. Upon ensuring that the expected strength has been achieved, holistic experimental tests are performed to (i) evaluate transport properties using rapid chloride penetration test (RCPT), surface resistivity, and rapid chloride migration test (RCMT), (ii) assess volume stability by measuring shrinkage properties (both autogenous and drying shrinkage), and (iii) examine frost resistance through freeze and thaw cycles. For comparison purposes, two additional proprietary UHPC mixtures are made and subjected to similar tests. A review of the obtained results shows the promise of the developed non-

proprietary UHPC mixtures in meeting the expected performance measures with only a fraction of cost of proprietary UHPC mixtures.

4.2 Experimental Program

4.2.1 Materials

The materials used for the non-proprietary UHPC mixtures developed for the current study consist of cement, silica fume, fine aggregate, masonry sand, steel fiber, high range water reducing (HRWR) admixture, and water. The selected cement was ASTM Type I cement with a specific density of 3.10. The silica fume was supplied by Elkem Materials. The chemical composition of both cement and silica fume are reported in Table 4.1. The fine aggregate was the same aggregate type used in the laboratory for conventional concrete mixtures (i.e., 0 - 4.75 mm (0.1870 in)). The fine aggregate was sieved in such a way that the maximum size is limited to 2.38 mm (0.0937 in). The specific density of fine aggregate was 2.72. The masonry sand was obtained from Hallett Materials, which is a local supplier in Ames, IA. To obtain the desired particle packing, the masonry sand was included to form 15% of the total sand, following the Andreasen-Andersen particle packing curve. The particle size distribution of the laboratory sand, masonry sand, cement, and silica fume are shown in Figure 4.1. The steel fibers had a diameter of 0.2 mm (0.0079 in) and length of 13 mm (0.5120 in).

Table 4.1 *Chemical oxides of cement and silica fume.*

Type of Binder	**CaO**	**SiO_2**	**SO_3**	**Fe_2O_3**	**Al_2O_3**	**MgO**	**K_2O**	**Na_2O**	**TiO_2**
Portland Cement	62.94	20.10	3.18	3.09	4.44	2.88	0.61	0.10	0.24
Silica Fume	0.30	94.30	-	0.10	0.09	0.43	0.83	0.27	-

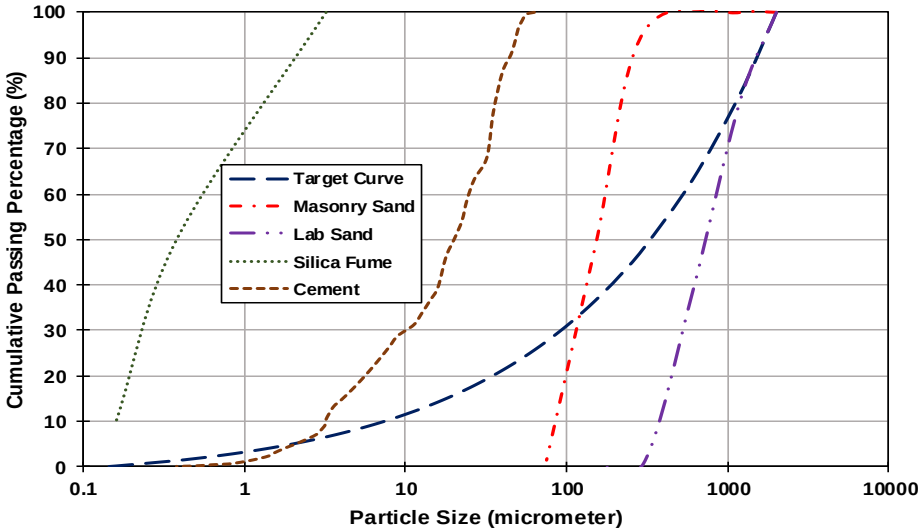

Figure 4.1 *Particle size distribution of used materials.*

For extending the investigations beyond non-proprietary mixtures, two proprietary UHPC mixtures were also prepared for this study. The first mixture, P1, contained a premix binder that included all the cement, fine sand, silica fume, and silica powder, as well as other proprietary materials that had not been reported. The other materials used in P1 were HRWR admixture, water, and steel fiber. The second mixture, P2, had a premix binder that included the silica fume and silica flour, as well as other proprietary materials that had not been reported. Contrary to the P1 premix binder, P2 did not include cement and sand, giving the flexibility of adding local sand and cement at the time of mixing. P2 also contained HRWR admixture, defoamer, shrinkage-reducing admixture, water, and steel fiber.

4.2.2 Mixture Design of UHPC

Among the factors that influence the properties of UHPC, particle packing is known to play a pivotal role to obtain a densely-packed mixture with proper workability (Shi et al., 2015). There are different packing models that can be employed for the particle packing of UHPC. Initially, the linear particle density model was introduced in the literature to predict the

optimal ratio between cement and mortar. This was based on the concept of virtual density, which was defined as the maximum density that can be achieved if the particles are placed by hand one by one. Due to the limitations of this model, the compaction density model was introduced. This model took into consideration the difference between the virtual and actual particle packing densities through a compaction index. With further advances, the most recent particle packing model, which has been used in this study, relies on the concept of continuous gradation. This model is based on the idea of Fuller and Thompson (1907), which proposed that the packing of aggregates affect the overall properties of concrete. This idea formed the foundation of the particle packing model proposed by Andreasen and Andersen (1930). The latest model indicates that an optimal particle size density results in minimum porosity, and thus, maximum strength. The percentage of particles smaller than size D, i.e., $P(D)$, for a particle-packed concrete can be calculated as:

$$P(D) = \left(\frac{D}{D_{max}}\right)^{q} \tag{4.1}$$

where D_{max} is the maximum particle size, and q is the distribution modulus, which determines the proportion of fine and coarse particles in the mixture. As the original model was unable to consider the effect of smallest sized particles, it was further modified by Funk and Dinger (1993). The modified Andreasen and Andersen particle packing model is based on the following equation, as reported by Yu et al. (2014):

$$P(D) = \frac{D^{q} - D_{min}^{q}}{D^{q} - D_{max}^{q}} \tag{4.2}$$

where D_{min} and D_{max} represent the smallest and largest particle size, respectively. The distribution modulus,q, varies based on the type of concrete. A q value greater than 0.50 results in a coarse mixture, while a q value less than 0.25 provides a mixture of fine content. According to Brouwers (2005 and 2006), a q value under 0.28 results in an optimal packing density. For self-compacting concrete, Hunger (2010) suggested a q value in the range of 0.22 to 0.25. Borges et.al (2014) suggested that a q value of 0.37 provides high particle density for self-compacting concrete. This was confirmed by El-Tawil et al. (2016) for UHPC mixtures. The preliminary results on different q values of 0.23, 0.30, and 0.37 supported the use of 0.37, which produced the highest packing density and strength value. Therefore, in the current study, the modified Andreasen and Andersen packing model with a q value of 0.37 was used as the target curve and the proportion of individual concrete ingredients was selected such that the obtained curve closely fit the target curve. A curve fit was considered an optimum fit when the sum of squares of residuals (RSS) was minimized. The RSS was calculated by the least square method as follows:

$$RSS = \sum_{i=1}^{n}(P_{mix}(D_i) - P_{tar}(D_i))^2 \quad (4.3)$$

where $P_{tar}(D_i)$ is the target passing percentage at particle size D_i, and $P_{mix}(D_i)$ is the passing percentage of the combined solid materials for particle size D_i in the designed mixture.

4.2.3 Mixture Proportion

The proportioning of non-proprietary UHPC mixtures was developed by using the modified Andreasen and Andersen curve to ensure that the maximum particle packing is achieved. The initial approach was to optimize the cumulative passing percentage curve by

bringing it as close to target curve as possible. The preliminary mixture proportions obtained from the fully optimized curve (shown in Figure 4.2(a)) resulted in an average compressive strength of 65.5 MPa (9.5 ksi) at 28 days. The insufficiency of compressive strength when the gradation curve was optimized with high sand-to-cement ratio (i.e., 2.3) proved that optimizing the particle packing alone is not sufficient to develop the expected strength. Noting that the sand-to-cement ratio plays a significant role in the strength development, this ratio was later modified to be in the range of 1.2 to 1.4 (by weight). Using this range and a water-to-cement ratio of 0.20 and 0.25, six non-proprietary mixtures were developed (Table 4.2).

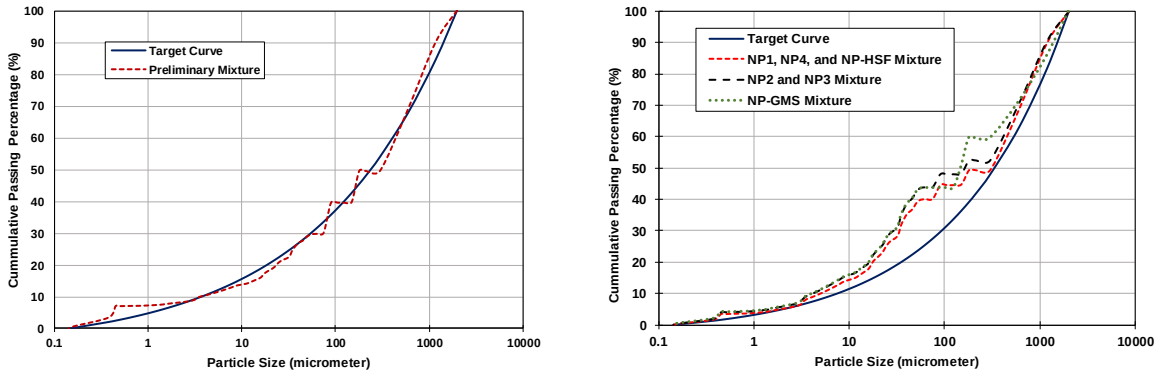

Figure 4.2 *Andreason-Andersen curves for (a) Preliminary designed curve, (b) solid particles' gradation curve of the developed non-proprietary UHPC mixes.*

The mixture designs were obtained by fixing the sand-to-cement ratio at 1.4 for the NP1 and 1.2 for the NP2 mixture, both with a water-to-cement ratio of 0.2. The NP3 and NP4 mixtures were made with similar sand-to-cement ratio of 1.4 and 1.2, respectively, but with a water-to-cement ratio of 0.25 to investigate the effect of water-to-cement ratio on the main properties of non-proprietary UHPC. The NP-HSF mixture was designed similar to the NP1 mixture, but with a silica fume content increased to 25% of the cement weight. For the listed mixtures, the sand that passed the 2.38 mm (0.0937 in) sieve was used. The sixth mixture, i.e.,

NP-GMS mixture, however, was designed with gradation modified sand. For this mixture, after sand was sieved and separated, the exact amount of sand fitting the target curve was used. This was to evaluate the effect of particle size of granular materials. Further to the six non-proprietary UHPC mixtures, two proprietary UHPC mixtures were prepared for comparison purposes.

Table 4.2 *Mix proportions*

Mixture	**NP1**	**NP2**	**NP3**	**NP4**	**NP-HSF**	**NP-GMS**	**P1**	**P2**
Flow (in)	8.5	8.5	8.0	9.0	8.5	8.0	8.5	8.5
7-Day Compressive Strength (ksi)	14.1	14.2	12.6	11.2	10.4	14.7	17.0	14.6
Split Tensile Strength (ksi)	1.47	1.54	1.53	1.50	1.59	1.71	2.10	1.74
Resistivity (kΩ-cm)	8.0	8.5	9.7	6.1	25.7	20.2	60.0	23.5
Ultimate Autogenous Shrinkage ($\times 10^{-6}$ m/m)	280	240	400	260	980	370	477	322
Ultimate Drying Shrinkage (%)	0.110	0.135	0.124	0.110	0.148	0.125	0.110	0.124

4.2.4 Mixing and Curing

Upon completing a set of preliminary tests, a step-by-step mixing procedure was developed similar to the previous studies on the development of non-proprietary UHPC (e.g., Berry et al., 2017). The sand and silica fume were first mixed for 5 minutes, followed by the addition of cement. After mixing the dry materials for 5 additional minutes, water and HRWR admixture were added. The mixing process was continued until each mixture became fluid (usually within 5-10 minutes). The steel fibers were then added by 2% of the concrete's volume and mixed until they fully dispersed (usually within 5 minutes). Upon finishing the mixing

process, the flow was measured and samples were cast. The samples were left in the mixing room for a day. They were then demolded and stored in the curing room until the time of the planned tests.

4.2.5 Test Plan

The samples of the developed non-proprietary and proprietary UHPC mixtures were tested for flow, compressive strength, tensile strength, rapid chloride penetration, rapid chloride migration, surface resistivity, autogenous shrinkage, drying shrinkage, and frost resistance. The flow was measured using the flow table modified following ASTM C143 for testing mortars. The flow test was in accordance with the standard, except that 25 drops of flow table were skipped as the developed UHPC mixtures were self-consolidating. The compressive test was performed on three 100×200 mm (4×8 in) cylinders of each mixture, according to ASTM C39. The split tensile strength test was conducted using three 100×200 mm (4×8 in) cylinders, following ASTM C469. The rapid chloride penetration test (RCPT) was carried out on three 50×100 mm (2×4 in) disks in accordance to ASTM C1202. Similar size disks (3 for each test) were used for the rapid chloride migration test (RCMT) based on NT BUILD 492. The surface resistivity was measured using 100×200 mm (4×8 in) cylinders in accordance with ASTM WK37880. The autogenous shrinkage was measured from the sealed corrugated plastic tubes of 420 mm (16.53 in) long with a diameter of 29 mm (1.14 in), according to ASTM C1698. The samples were stored in a room temperature of 73 ± 5 ºF. The drying shrinkage was measured on 25×25×258 mm (1×1×10 in) prisms, following ASTM C596. The resistance to freeze and thaw cycles was evaluated for each mixture on three beam samples of 75×100×279 mm (3×4×11 in), in accordance with ASTM C666.

4.3 Assessment of Flow and Strength Properties

4.3.1 Flow

The flow of UHPC mixtures was evaluated similar to mortars by using a flow table. Each mixture was allowed to spread and the flow was measured after the mixture stopped spreading. The results of flow test are reported in Table 4.3. It can be seen that all the mixtures had a consistent flow of 203 mm (8 in) to 228mm (9 in). This confirmed that all the developed mixtures were self-consolidating and can be cast properly without external vibration.

4.3.2 Compressive and Split Tensile Strength

The compressive strength test was conducted on three cylinders of each mixture at the age of 7 days. Their average values have been provided in Table 4.3. Among the developed non-proprietary mixtures, the compressive strength of the NP-GMS mixture was the highest, followed by the NP2, NP1, NP3, NP4, and NP-HSF mixtures. The compressive strengths of the non-proprietary mixtures were in the same range of the compressive strength of the P2 proprietary mixture, while the P1 proprietary mixture provided the highest 7-day compressive strength.

The change in the water-to-cement ratio from 0.20 to 0.25 (i.e., NP1 and NP2 compared to NP3 and NP4, respectively) was found to decrease the compressive strength of mixtures by up to 20%. The increase of the silica fume content also resulted in a reduction of compressive strength, proving that excessive amount of silica fume can have an adverse effect on strength properties. The increase in the sand-to-cement ratio (in the studied range of 1.2 to 1.4) resulted in a negligible reduction of compressive strength. This can be explained with the fact that UHPC contains a high amount of cement, a great portion of which remains unhydrated.

Therefore, change of cement content in the studied range did not influence the hydration and strength development in any significant way. Table 4.3 also reports the results of split tensile test performed on the developed mixtures. The tensile strength for the NP-GMS mixture was the highest among the developed non-proprietary UHPC mixtures because of the modified gradation and improved packing. The obtained tensile strengths showed similar trends with changes in the water-to-cement ratio, sand-to-cement ratio, and silica fume content. Although the tensile strengths of the developed mixtures were lower than their proprietary counterparts, they can be considered sufficiently high for non-proprietary UHPC.

Table 4.3 *Results of fresh, strength and transport properties.*

Mixture	**NP1**	**NP2**	**NP3**	**NP4**	**NP-HSF**	**NP-GMS**	**P1**	**P2**
Flow (in)	8.5	8.5	8.0	9.0	8.5	8.0	8.5	8.5
7-Day Compressive Strength (ksi)	14.1	14.2	12.6	11.2	10.4	14.7	17.0	14.6
Split Tensile Strength (ksi)	1.47	1.54	1.53	1.50	1.59	1.71	2.10	1.74
Resistivity (kΩ-cm)	8.0	8.5	9.7	6.1	25.7	20.2	60.0	23.5
Ultimate Autogenous Shrinkage ($\times 10^{-6}$ m/m)	280	240	400	260	980	370	477	322
Ultimate Drying Shrinkage (%)	0.110	0.135	0.124	0.110	0.148	0.125	0.110	0.124

4.4 Assessment of Transport Properties

4.4.1 Electrical Resistivity

Considering the advantages of electrical resistivity tests, including low cost and ease of use in practice, there has been growing attention to this test for evaluating the concrete's transport and permeability properties. In this study, the surface resistivity was measured on

three cylinders of each mixture and their average values are reported in Table 4.3. The surface resistivity of the non-proprietary UHPC mixtures varied in the low range of 6.1 to 9.7 kΩ-cm for the mixtures with low silica fume content and increased to 25.7 kΩ-cm for the mixture with high silica fume content (i.e., NP-HSF). The superior resistivity of the NP-HSF mixture highlights that the increase of silica fume can result in a considerable increase in resistivity. The surface resistivity of the proprietary mixtures, particularly P1, was high. This indicates that although the mixture proportions of proprietary UHPC mixtures were not available, they should have contained a significant amount of silica fume. This observation raises two important questions: (1) if the developed non-proprietary mixtures can provide similar resistance against chloride penetration, and (2) if the electrical resistivity test (and RCPT) are viable tests for the assessment of transport and permeability properties of UHPC. The answer to these two questions was sought in the following tests.

4.4.2 Chloride Penetration Tests

The developed UHPC mixtures were tested for chloride penetration with both RCPT and RCMT. The results from RCPT followed the trend observed by the surface resistivity test, showing a significantly high passing charge in the range of 3000 to 10000 Coulombs in different non-proprietary mixtures. To understand if the mixtures are truly vulnerable to chloride attack and if the surface resistivity test and RCPT are proper tests for such evaluation, a RCMT was devised. While the RCPT measured the charge passed through the concrete sample and related it to chloride ion penetration, the measurement in RCMT was based on observing the penetrated depth of chloride ions through the formation of white silver chloride where the sprayed silver nitrate reaches to and reacts with penetrated chloride (Najimi et al. 2017). The results of RCMT are presented in Figure 4.3 for all the non-proprietary and

proprietary mixtures. It can be seen in this figure that the depth of chloride penetration into the non-proprietary mixtures (and the associated chloride migration coefficients) was very low to negligible, similar to the proprietary mixtures. Figure 4.4 highlights the low penetration depth of chloride in a sample of the NP1 mixture after the RCMT.

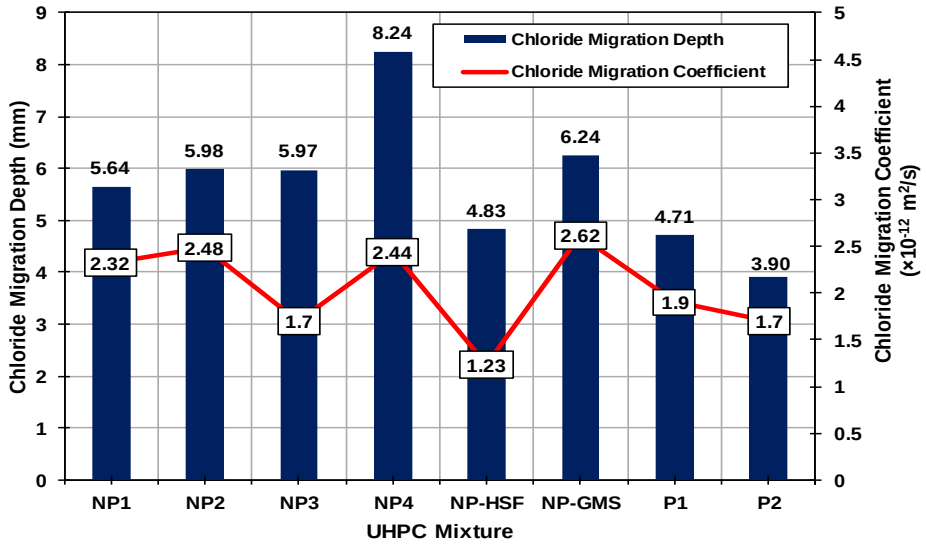

Figure 4.3 *Chloride migration depth and chloride migration coefficient of UHPC mixes*

Figure 4.4 *Chloride migration in a sample of NP1 in rapid chloride migration test*

(a)

(b)

Figure 4.5 *(a) Corrosion of fibers only on the surface of non-proprietary mix (b) Corrosion of fibers in the depth of a sample of proprietary mix P1*

To evaluate the common perception that steel fibers do not corrode in UHPC (or only corrode on the surfaces), the samples were carefully examined to understand if there are any signs of steel fiber corrosion. Figure 4.5(a) shows that there was corrosion of steel fibers in non-proprietary mixtures, but this corrosion was only on the exposed surface of the samples. On the other hand, there were signs of steel fiber corrosion further deep into the samples for the P1 proprietary mixtures, as shown in Figure 4.5(b). Based on the results collectively obtained from the resistivity test, RCPT, and RCMT, as well as the corrosion observed in the steel fibers of proprietary mixtures (with considerably high resistivity), the capability of existing accelerated test methods for determining the vulnerability of UHPC mixtures to chloride penetration is found to be in need of further investigation.

4.5 Assessment of Shrinkage Behavior

4.5.1 Autogenous Shrinkage

Figure 4.6 shows the results of autogenous shrinkage tests performed during a 140-day period. It can be seen in this figure that, except for the NP-HSF mixture, which consistently showed the highest shrinkage, the autogenous shrinkage of the developed non-proprietry mixtures were in the same range of the proprietary mixtures. The high autogenous shrinkage of the NP-HSF mixture can be related to its high silica fume content. This is consistent with the literature, as the use of mineral additives that contain fine capillary pores (e.g., silica fume) is proven to increase the susceptibility of a mixture to self-desiccation and autogenous shrinkage (Mazloom et al., 2004, Zhang et al., 2003, Meng and Khayat, 2017). The reduction of the water-to-cement ratio in the mixtures with a similar sand-to-cement ratio resulted in increased initial autogenous shrinkage (at early ages) and reduced ultimate shrinkage (when comparing the NP4 with the NP1 mixture for the sand-to-cement ratio of

1.4 and the NP3 with the NP2 mixture for the sand-to-cement ratio of 1.2). With reducing the water-to-cement ratio, self-desiccation increases the capillary tension in the pore fluid, resulting in higher autogenous shrinkage (Meng and Khayat, 2017). This is commonly observed in the early age of UHPC (Mechtcherine et al., 2017, Yoo et al., 2014, Koh et al., 2011). The mixtures with a lower sand-to-cement ratio were found to experience higher autogenous shrinkage. This can be attributed to the lower content of fine aggregates in their mixtures, which in turn, can reduce their restraining effect to prevent the autogenous shrinkage.

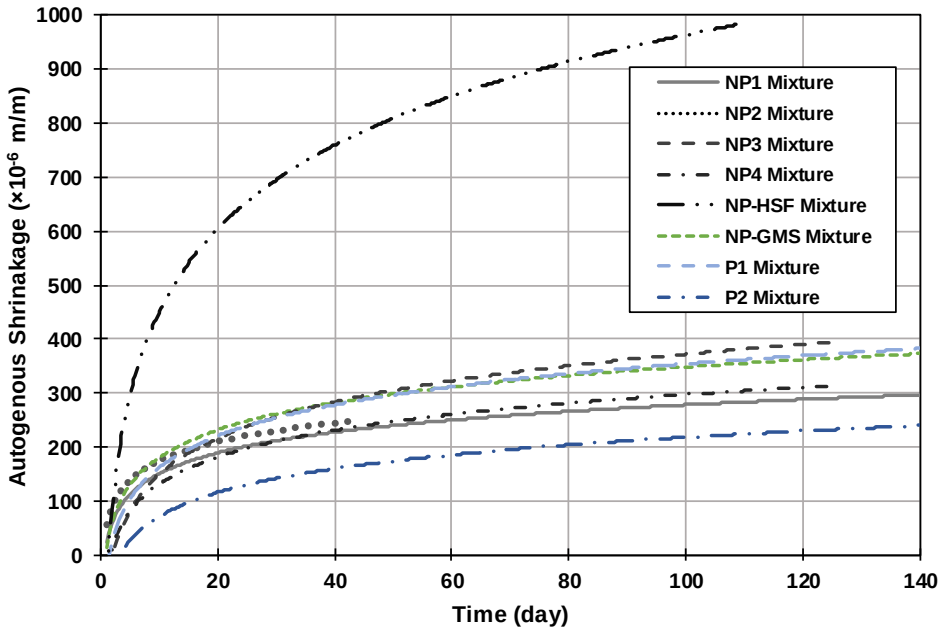

Figure 4.6 *Autogenous shrinkage plot for UHPC mixes*

4.5.2 Drying Shrinkage

The drying shrinkage readings were taken for four samples of each mixture and their average values were plotted in Figure 4.7. Except for the NP-HSF mixture, which contained a high amount of silica fume, the drying shrinkage of all the developed non-proprietary UHPC mixtures were close to each other. As discussed for autogenous shrinkage, the inclusion of

silica fume can be the cause of this increased shrinkage. Increases in the water-to-cement ratio for the mixtures with a similar sand-to-cement ratio resulted in increased drying shrinkage. This can be explained with the weakened microstructure of the paste and the availability of evaporable moisture, which is responsible for volume instability. An increase in the sand-to-cement ratio for the mixtures with a similar water-to-cement ratio led to the reduction of drying shrinkage. This can be attributed to the restraining effect of fine aggregates, which was improved by increasing the sand-to-cement ratio.

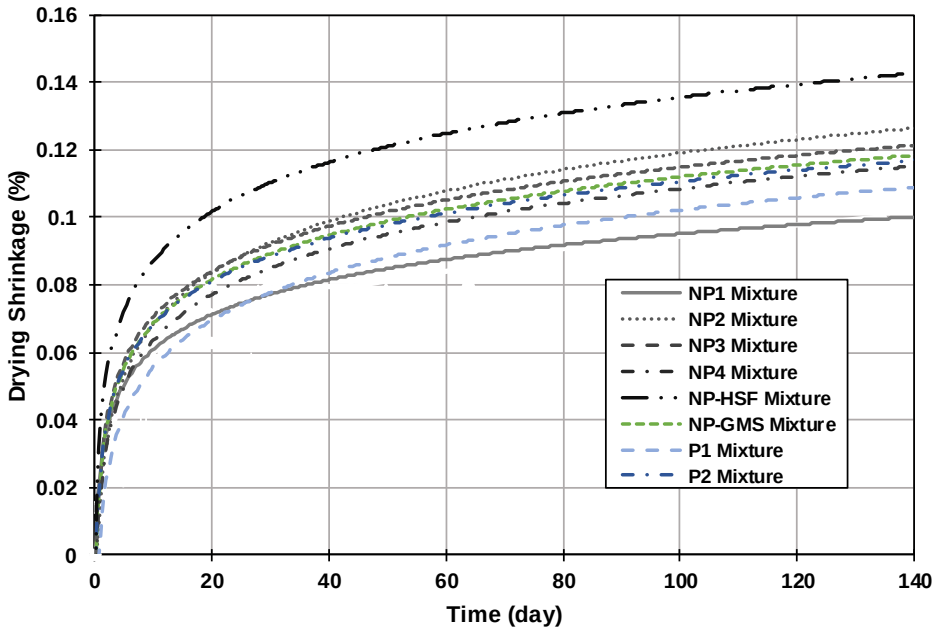

Figure 4.7 *Drying shrinkage of UHPC mixes*

While the drying shrinkage of non-proprietary and proprietary UHPC mixtures were close (except for the NP-HSF mixture), most of the non-proprietary mixtures showed a slightly higher drying shrinkage than the P1 proprietary mixture. Based on this observation and the fact that the P1 mixture most likely contains high silica fume, it was inferred that the P1 mixture also have some type of shrinkage-reducing admixture in the form of powder

included in the premix binder. The NP-HSF mixture, which had a 25% silica fume content, showed the highest values of drying shrinkage. This confirmed the direct relationship between the silica fume content and drying shrinkage in the UHPC mixtures.

4.6 Assessment of Frost Resistance

For the purpose of understanding the behavior of the developed non-proprietary UHPC mixtures under freeze and thaw cycles, three beam samples of each mixture were subjected to rapid cycles of freeze and thaw (300 cycles). In 30-cycle intervals, mass and dynamic modulus of the mixtures were measured to assess the frost resistance. A review of the obtained results indicates that the performance of non-proprietary and proprietary UHPC mixtures remain satisfactory and similar. This can be verified with the fact that there was only a negligible loss in mass for all the samples after 300 cycles (Figure 4.8(a)). The change in the relative dynamic modulus of elasticity, as shown in Figure 5.8(b), was also consistently negligible even after 300 cycles.

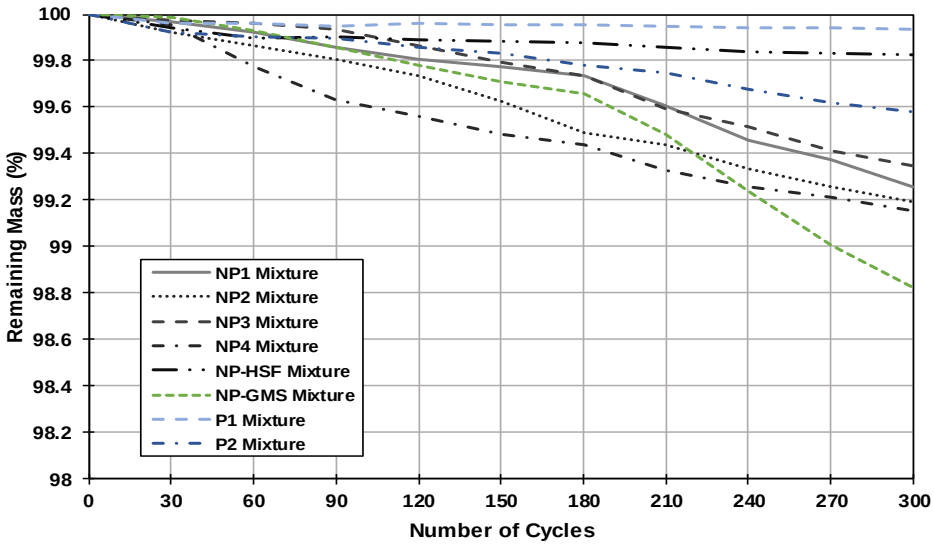

(a)

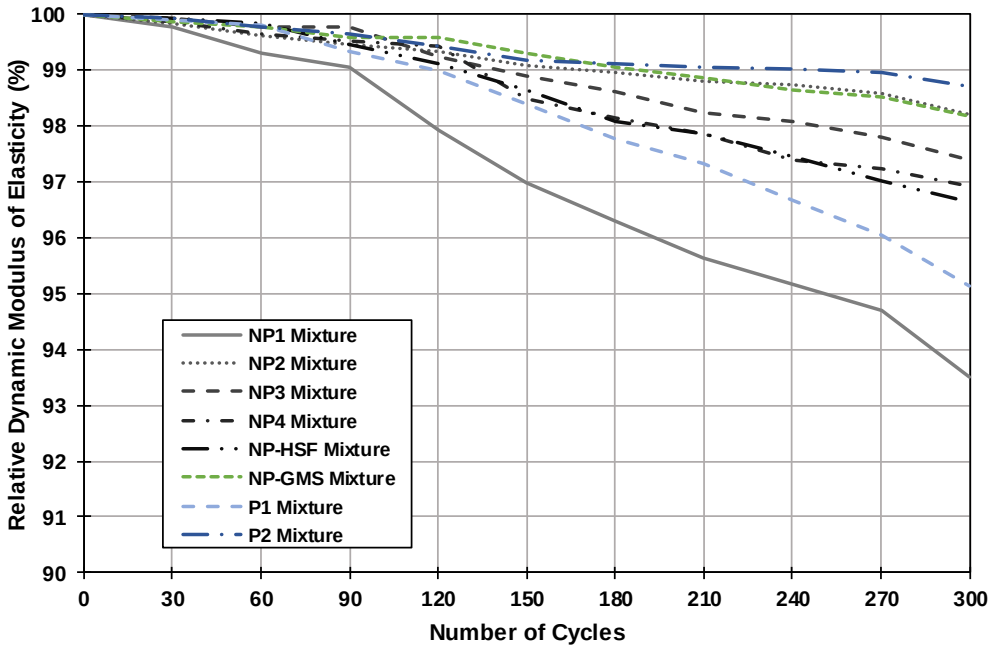

(b)

Figure 4.8 *(a) Remaining mass of samples in Freeze Thaw test, and (b) Relative dynamic elasticity of Freeze Thaw sample*

It should be noted that the freeze-thaw test was expected to be terminated when the relative dynamic modulus of elasticity reaches 60% of its original value (ASTM C666). This threshold was never reached, indicating the high frost resistance of the developed mixtures.

CHAPTER 5. CONCLUSIONS AND RECOMMENDATIONS

This chapter summarizes the conclusions and findings from experimental tests, finite element simulations, and material investigations performed for link slabs in this study.

5.1 Summary

The presented study consisted of a set of two experiments on full scale link slabs, including FRC in combination with steel and GFRP rebars. The performance of FRC link slab with steel and GFRP reinforcement was evaluated. The effect of two different type of detailing for transition zone was also investigated. The study also included the experimental study on the effect of support condition on stresses in the link slab. The study further explored the effect of the introduction of link slab on a full scale bridge. The stresses in the link slab and in the bridge pier along with the stresses in the girders were evaluated. The study was then extended to develop an economic non-proprietary UHPC mix, which could be used in the link slabs with properties comparable to the proprietary UHPC. The preliminary evaluation showed that the material developed has satisfactory strength and durability properties.

5.2 Conclusions

The following conclusions can be drawn from experimental study, finite element modeling and material development.

5.2.1 Conclusions from the Study on Performance Evaluation of Link Slabs by Experimentation

In this section of the presented study, the performance of two link slabs was evaluated through two full scale experiments. The link slabs were in combination of FRC with steel and

GFRP rebars. The data from experimental tests were used to validate finite element model of the tested samples and a set of parameters, including rebar spacing in the debonded region, rebar spacing in bonded region and the depth of the link slab. The following conclusions can be drawn from this study.

1. A half depth FRC link slab made with GFRP rebar results in more flexible link slab than that made with steel rebars.
2. Although the first crack appeared in the FRC with GFRP rebar link slab, the cracks following the first crack appeared in later stages of loading and had tighter widths than those in the FRC with steel rebar link slab.
3. The half depth link slabs made with FRC in combination with either steel or GFRP rebar can be implemented in both cast in place and rehabilitation projects.
4. The provision of supplementary rebars in the bonded zones helps with transferring the stresses to the link slab. This avoids the problem of macrocracking at the face of connection of link slab and bridge deck.
5. The cracks developed were all concentrated in the debonded region as intended. The FRC link slab had a fine web of cracks, instead of one macro crack, which suggests that the fibers in the FRC were able to limit the crack width.
6. From the finite element modelling of the experimental setup, it was found that the rebar spacing in the debonded zone affects the strain produced on top of link slab. The strain distribution however followed the same trend, irrespective of rebar spacing.

7. The parametric study on the rebar spacing in the bonded zone showed that the provision of additional rebars in the transition zone resulted in the increased strain in the debonded region, which shows that the additional reinforcement ensures the transfer of all stresses to the debonded region.
8. The finite element models showed that the increase in depth of link slab results in lower strains. This finding is consistent with the general understanding of this structural system since the increase in depth results in the increased moment of inertia of the link slab and thus higher resistance to the moment.
9. As the depth of link slab is increased, the strain values reduced but the strain distribution differed from 4 in depth to 8 in depth. As the depth increased, the strain distributed outwards from the center of the debonded region of the link slab, while in lower depth it was concentrated at the center on top of the expansion joint.

5.2.2 Conclusions from Investigation of Loading Distribution in Bridges

This section of the study investigated how the addition of link slabs to bridges can change the loading demand on their super and substructures. For this purpose, full-scale experimental tests of a link slab setup were performed in the laboratory with three different support configurations. The scope of investigations was further extended through a set of FE simulations of the same test setup to understand the effect of support condition under thermal induced forces and the effect of variation of debonded length of link slab. Upon obtaining a full understanding of the structural response of the link slab under combinations of roller and pinned supports, a representative nine-span bridge was considered to evaluate how the loading demand in a full bridge structure changes as a result of adding link slabs. This was

achieved through monitoring various structural response measures, such as the deflections, axial forces and moments in the super structure and the reaction force and reaction moments in the substructure of the bridge. The following conclusions were drawn from this study.

1. The experimental test in the laboratory showed that support condition has a significant effect on the strains developed in the link slab. The PRRP case provides the lower bound for strains in the rebars located in debonded region of link slab and on the surface of the link slab, while the RPPR case provides the upper bound for strains.
2. In contrast to the finding of the past experimental studies it was found that the slope of load deflection curve for different support condition varies and this finding was complemented by the finite element simulation results as well.
3. The thermal induced stresses also varied by variation in the support condition. The PRPR support condition results in the highest demand on the link slab while the PRRP condition results in the lowest demand on the link slab.
4. Among the three debonded lengths explored for the FE models of link slab tested, the debonded length of 2.5% resulted in the minimum deflection while the debonded length of 7.5 % resulted in maximum deflection at the midpoint, the strains however were observed to be maximum for the debonded length of 5% and minimum for the debonded length of 2.5%.
5. The bending moment in the link slab is maximum for the RPPR and minimum for the PRRP support conditions, while the axial force was maximum in the PRRP and minimum for the RPPR support condition. The moments and axial

forces in the midspan of the bridge are highest for PPPP support condition and lowest for the RPPR condition.

6. The support conditions have a significant effect on the reaction moments in the piers for both bridges with link slabs and without link slabs. The change in moment demand on the end pier after addition of link slab increased as high as 6 times for different support condition. The support conditions PRRP and PPPP resulted in similar reaction moments on the piers other than those directly under the link slab. For the piers below the link slab, the reaction moment was minimum for the PRRP support configuration and maximum for the RPPR support condition. The reaction moments are not affected by changing the debonded length of the link slab.
7. The variation in the debonding length has no effect on the axial force in the link slab, while the bending moment increased with the increase in the debonded length of the link slab. The axial stresses in the midspan of the middle deck of the bridge was not affected by the variation in the debonded length of the link slab. The bending moment at the middle of the deck decreases with increase in the debonded length of the link slab.

5.2.3 Conclusions from Material Development

With the ultimate goal of developing economic, non-proprietary UHPC mixtures with desired performance characteristics, this portion of the presented study was primarily focused on the transport properties, volume stability, and frost resistance of six non-proprietary UHPC mixtures in comparison with two proprietary mixtures. The following conclusions can be made based on the results and observations obtained from a rigorous set of tests, including

flow, compressive strength, tensile strength, rapid chloride penetration, rapid chloride migration, surface resistivity, autogenous shrinkage, drying shrinkage, and freeze and thaw.

1. Use of the modified particle packing density curve and the optimization of cumulative passing percentage may not result in the expected performance without a proper selection of water-to-cement and sand-to-cement ratios. This highlights the importance of taking into consideration all the main contributing factors when designing non-proprietary UHPC mixtures.
2. While the surface resistivity of non-proprietary mixtures were lower than that of proprietary mixtures, the depth of chloride penetration and chloride migration coefficient were almost the same for all the non-proprietary and proprietary mixtures. On the other hand, traces of steel fiber corrosion was observed in the proprietary mixtures with a high surface resistivity and low RCPT passing charge. Such findings suggested that the surface resistivity test and RCPT may not be the most proper experiments for assessing the performance of UHPC against chloride penetration. Thus, further investigations, involving the chloride diffusion and chloride-induced corrosion of UHPC mixtures, can be helpful.
3. The average autogenous shrinkage of non-proprietary mixtures were 22.5% lower than that of the proprietary mixtures. However, the autogenous shrinkages of the developed non-proprietary mixtures increased with increasing the silica fume content (up to twice of the average of all the tested non-proprietary mixtures). An increase of 26% and 36% were recorded by changing the water-to-cement ratio from 0.20 to 0.25 and the sand-to-cement

ratio from 1.2 to 1.4, respectively. The drying shrinkage of non-proprietary and proprietary mixtures were close with a variation under 3%.

4. The developed non-proprietary mixtures performed very well under the freeze thaw tests, which were continued up to 300 cycles. All the mixtures were found to have a mass loss of less than 2% and drop in the relative dynamic modulus of elasticity of less than 7%. This indicated the capability of the developed UHPC mixtures for the applications that involve extreme exposure conditions.

The experimental work done along with finite element modelling in this study helped understand the structural behavior of link slabs. The study found that the support conditions have significant effect on the stresses developed in the link slab. The study also determined that a flexible link slab can be designed by using GFRP rebar in conjunction with FRC. The promise of a non-proprietary UHPC was also explored using local materials. This was to ensure that the developed non-proprietary UHPC had good transport and freeze thaw properties, which are critical for structural elements, such as link slabs.

5.3 Future work

The current experimental work can be extended by exploring the effect of support conditions by testing full scale beams to the ultimate capacity under different support conditions. This will provide a complete understanding of the link slab behavior under different support conditions in linear and nonlinear stress/strain range, which will be helpful in the structural analysis and design.

The design of the transition and bonded zone for half depth link slab needs to be further explored as these regions have a significant role in transferring the stresses to the debonded

zone. This aspect becomes more important in precast link slabs where a good bonding between the newly installed link slab and the old concrete deck can be a problem. The effect of debonding is another aspect that needs to be explored, especially for partial depth link slabs, as a plastic sheet needs to be provided in the middle of the deck, which is not desirable because of the possible accumulation of water. This water can undergo cycles of freezing and thawing, resulting in additional stresses and cracks. The exploration of the effect of debonding can be an important topic to explore in partial depth link slabs.

The non-proprietary UHPC developed can be further investigated to understand their flexural properties and bond strength with steel and GFRP rebars. This will evaluate its capability to be considered as a viable material for link slabs. Finally, long term monitoring of link slabs used in the field can provide invaluable information to ensure the performance and durability of bridges, especially at their joints.

REFERENCES

Andreasen, A.H.M. and Andersen, J. (1930). *Über die Beziehung zwischen Kornabstufung und Zwischenraum in Produkten aus losen Körnern (mit einigen Experimenten).* Colloid & Polymer Science, Vol. 50 (3), pp. 217-228.

ACI Committee 544. (2009). *Report on Fiber Reinforced Concrete,* ACI 544.1R-96 (Reapproved 2009). American Concrete Institute.

ASTM, C 1609/C 1609M-05. (2005). *Standard Test Method for Flexural Performance of Fiber-Reinforced Concrete (Using Beam with Third-Point Loading),* ASTM International.

ASTM Standard C39, (2005).*Standard Test Method for Compressive Strength of Cylindrical Concrete Specimens*. ASTM International.

Au, A., Lam,C.,Au, J., and Tharmabala, B. (2013). *Eliminating Deck Joints Using Debonded Link Slabs: Research and Field Tests in Ontario*. Journal of Bridge Engineering, Vol. 18, No. 8, , pp. 768-778.

Shin-ichi Igarashi, A.W., Kawamura, M. (2005). *Evaluation of capillary pore size characteristics in high-strength concrete at early ages*, Cement Concr. Res. 35, 513–519.

Borges P.H.R., Fonseca L.F., Nunes V.A., Panzera T.H., Martuscelli C.C. (2014). *Andreasen Particle Packing Method on the Development of Geopolymer Concrete for Civil Engineering*. J Mater Civ Eng;26(4):692–7.

Berry, M., Snidarich, R., Wood, C. (2017). *Development of non-proprietary ultra-high performance concrete*.The state of Montana Department of transportation.

Chen, S., Zhang, R., Jia, L.J., Wang, J.Y., Gu, P. (2018). *Structural behavior of UHPC filled steel tube columns under axial loading*. Thin-Walled Struct.;130(March):550–63.

Charuchaimontri, T., Senjuntichai, T., Ožbolt, J., Limsuwan, E. (2008). *Effect of lap reinforcement in link slabs of highway bridges. Engineering Structures*, Vol. 30, No. 2, pp. 546-560.

De Larrard, F., Sedran, T. (1994). *Optimization of ultra-high-performance concrete by the use of a packing model*. Cem Concr Res.;24(6):997–1009.

Dong, Y. (2018). *Performance assessment and design of ultra-high performance concrete (UHPC) structures incorporating life-cycle cost and environmental impacts*. Constr Build Mater. ;167:414–25.

El-Safty, A.K. (1994). *Analysis of Jointless Bridge Decks with Partially Debonded Simple*

Span Beams. PhD. Dissertation, North Carolina State University Raleigh, NC.

El-tawil, S., Alkaysi, M., Naaman, A.E., Hansen, W., Liu, Z. (2016). *Characterization and Application of a Non Proprietary Ultra High Performance Concrete for Highway Bridges* (MDOT RC-1637).

Fuller, W.B., Thomson, S.E. (1907). *The Laws of Proportioning Concrete*. Vol. 59, Transactions of the American Society of Civil Engineers. p. 67–143.

Graybeal, B.A. (2014). *Design and Construction of Field-Cast UHPC Connections*. FHWA. 1-36 p.

Gastal, F., and P. Zia. (1989). *Analysis of Bridge Beams with Jointless Decks*. Proceedings of IASBE Symposium, pp. 555-560.

Gu, C.P., Ye, G., Sun, W. (2015). *Ultrahigh performance concrete-properties, applications and perspectives*. Sci China Technol Sci.; 58(4):587–99.

Ghafari, E., Costa, H., Júlio, E. (2015). *Statistical mix design approach for eco-efficient UHPC*. Cem Concr Compos;55:17–25.

Hunger, M. (2010). *An integral design concept for ecological self-compacting concrete*, PhD thesis Eindhoven University of Technology, Eindhoven, the Netherlands.

Hossain, K. M. A., and M. S. Anwar. (2014). *Strength and Deformation Characteristics of ECC Link Slab in Joint-Free Bridge Decks*. Istanbul Bridge Conference.

Brouwers, H.J.H. and Radix, H.J. (2005). *Self-compacting concrete: theoretical and experimental study*, Cem. Concr. Res. 35.2116–2136.

Brouwers, H.J.H. (2006). *Particle-size distribution and packing fraction of geometric random packings*, Phys. Rev. E 031309-1–031309-14.

Funk, J.E., Dinger, D.R. (1994). *Predictive Process Control of Crowded Particulate Suspensions, Applied to Ceramic Manufacturing*, Kluwer Academic Publishers, Boston, the United States.

Kahanji, C., Ali, F., Nadjai, A., Alam, N. (2018). *Effect of curing temperature on the behaviour of UHPFRC at elevated temperatures*. Constr Build Mater;182:670–81.

Kim, Y.J. (2018). *Development of Cost-Effective Ultra-High Performance Concrete (UHPC) for Colorado's Sustainable Infrastructure*. University of Colorado, Denver; Colorado Department of Transportation, 66p.

Koh, K.T., Ryu, G.S., Kang, S.T., Park, J.J., and Kim, S.W. (2011). *Shrinkage properties of ultra-high performance concrete (UHPC)*, Advanced Science Letters, 4(3), 948-952.

Ho, E., and Lukashenko, J. (2011). *Link Slab Deck Joints*. Annual Conference of the Transportation Association of Canada.

Hulsey, J.L. (1992). Final report bridge lengths : *jointless prestressed girder BRIDGES* by School of Engineering University of Alaska Fairbanks 263 Duckering Building Fairbanks , AK 99775, Prepared for Alaska Cooperative Transportation And Public Facilities Quic.

Johnston, C. D. (2001). *Fiber-Reinforced Cements and Concretes*, CRC Press, Vol. 3.

Kim, Y. Y., G. Fischer, and Li, V.C. (2004). *Performance of Bridge Deck Link Slabs Designed with Ductile Engineered Cementitious Composite*. ACI Structural Journal, Vol. 101 No. 6, pp. 792-801.

Lárusson, L.H. (2013). *Development of Flexible Link Slabs using Ductile Fiber Reinforced Concrete*. PhD Thesis, Technical University of Denmark, Lyngby, Denmark.

Li, V. C., E. H., Yang, and Li, M. (2008). *Field Demonstration of Durable Link Slabs for Jointless Bridge Decks Based on Strain-Hardening Cementitious Composites–Phase 3*: Shrinkage Control. Research Report RC-1506. Michigan Department of Transportation.

Li, V.C., and Lepech, M. D. (2009). *Application of ECC for Bridge Deck Link Slabs*. Materials and Structures, Vol. 42, Issue 9, pp. 1185-1195.

Li, V. C., Lepech, M. D., and Li, M. (2005). *Field Demonstration of Durable Link Slabs for Jointless Bridge Decks Based on Strain-Hardening Cementitious Composites*. Research Report RC-1471. Michigan Department of Transportation.

Li, V. C. (2008). *Engineered Cementitious Composites (ECC) Material*, Structural, and Durability Performance, University of Michigan, Ann Arbor, MI.

Mazloom, M., Ramezanianpour, A.A., and Brooks, J.J. (2004). *Effect of silica fume on mechanical properties of high-strength concrete*, Cement and Concrete Research, 26, 347-357.

Meng, W., and Khayat, K. (2017). *Effects of saturated lightweight sand content on key characteristics of ultrahigh-performance concrete*, Cement Concr. Res., 101, 46-54.

Mechtcherine, V., Dudziak, L., and Hempel, S. (2009). *Internal curing to reduce cracking potential of ultra high performance concrete by means of super absorbent polymers*, Proceedings of 2nd International RILEM Workshop on Concrete Durability and Service Life Planning, 31-38.

Najimi, M., Ghafoori, N., Sharbaf, M. (2017). *Alkali-activated natural pozzolan/slag mortars: A parametric study*. Constr Build Mater. 2018;164:625–43,12.222

Richard, P., Cheyrezy, M. (1995). *Composition of reactive powder concretes*. Cem Concr Res. 1995;25(7):1501–11.

Rajasekar, A., Arunachalam, K., Kottaisamy, M., Saraswathy, V. (2018). *Durability characteristics of Ultra High Strength Concrete with treated sugarcane bagasse ash*. Constr Build Mater.;171:350–6.

Russel, G.H., Graybeal, B. (2013). *Ultra-High Performance Concrete : A State-of-the-Art Report for the Bridge Community*.FHWA-HRT-13-060.

Ryes, J., and Robertson, I. N. (2011). *Precast Link Slabs for Jointless Bridge Decks. Research Report* UHM-CEE-11-09. FHWA, U.S. Department of Transportation.

Samani, G. S. (2013). *Structural Performance of Link Slabs Subjected to Monotonic and Fatigue Loading Incorporating Engineered Cementitious Composites*. MSCE Thesis, Ryerson University, Toronto, Canada.

Shi, C., Wu, Z., Xiao, J, Wang, D., Huang, Z., Fang, Z. (2015). *A review on ultra high performance concrete: Part I. Raw materials and mix design*. Constr Build Mater.;101:741–51.

Soliman, N.A., Tagnit-Hamou, A. (2017). *Using glass sand as an alternative for quartz sand in UHPC*. Constr Build Mater.;145:243–52.

Soliman, N.A., Tagnit-Hamou, A. (2017). *Partial substitution of silica fume with fine glass powder in UHPC: Filling the micro gap*. Constr Build Mater.;139:374–83.

Ulku, E., Attanayake, U., and Aktan, H. (2009). *Jointless Bridge Deck with Link Slabs: Design for Durability*. In Transportation Research Record: Journal of the Transportation Research Board, No. 2131, Transportation Research Board of the National Academies, Washington D.C., pp. 68-78.

Wing, K. M., and Kowalsky, M. J. (2005). *Behavior, Analysis, and Design of an Instrumented Link Slab Bridge*. Journal of Bridge Engineering, Vol. 10, No. 3, pp. 331-344.

Wille, K. (2013). *Development of Non-Proprietary Ultra-High Performance Concrete for Use in the Highway Bridge Sector* (FHWA-HRT-13-100).;59

Wille, K., Naaman, A.E., El-Tawil, S., Parra-Montesinos, G.J. (2012). *Ultra-high performance concrete and fiber reinforced concrete: Achieving strength and ductility without heat curing*. Mater Struct Constr.;45(3):309–24.

Yoo, D.Y., Yoon, Y.S. (2015). *Structural performance of ultra-high-performance concrete beams with different steel fibers*. Eng Struct.;102:409–23.

Yu, R., Spiesz, P., Brouwers, H.J.H. (2014). *Mix design and properties assessment of Ultra-High Performance Fibre Reinforced Concrete (UHPFRC)*. Cem Concr Res;56:29–39.

Yang, S.L., Millard, S.G., Soutsos, M.N., Barnett, S.J., Le, T.T. (2009). *Influence of aggregate and curing regime on the mechanical properties of ultra-high performance fibre reinforced concrete (UHPFRC)*. Constr Build Mater.;23(6):2291–8.

Zou, X.X., Wang, J.Q. (2018). *Experimental study on joints and flexural behavior of FRP truss-UHPC hybrid bridge*. Compos Struct.;203(June):414–24.

Zuk, W. (1981). *Jointless Bridges*. Research Report No. FHWA/VA-81-48. Virginia Highway and Transportation Research Council.

Zhang, M.H., Tam, C.T., Leow, M.P. (2003). *Effect of water-to-cementitious materials ratio and silica fume on the autogenous shrinkage of concrete*, Cement Concr. Res. 33, 1687–169.